

DISSERTATION
SUBMITTED TO THE
COMBINED FACULTIES OF NATURAL SCIENCES AND MATHEMATICS
OF THE RUPERTO-CAROLA UNIVERSITY OF HEIDELBERG, GERMANY
FOR THE DEGREE OF
DOCTOR OF NATURAL SCIENCES

Put Forward by
Xiangcheng Chen
Born in Chaohu, China
Date of Defense: 18 November 2015

NON-INTERCEPTIVE POSITION DETECTION
FOR SHORT-LIVED RADIOACTIVE NUCLEI
IN HEAVY-ION STORAGE RINGS

Referees: Prof. Dr. Klaus Blaum
PD Dr. Adriana Pálffy

Abstract

A heavy-ion storage ring can be operated as an isochronous mass spectrometer with a particular ion-optical setting. However, the isochronism condition cannot be fulfilled for all the stored ions due to the large momentum acceptance of the ring, which restricts the measurement precision. Although this anisochronism effect can be corrected for by measuring the velocity of each ion with two time-of-flight detectors, the number of admissible ions is severely limited by this detection technique. As a complementary approach, it is proposed to measure the magnetic rigidities of the circulating ions non-interceptively with an intensity-sensitive and a position-resolving cavity jointly to overcome this limitation. Moreover, this approach also enables simultaneous lifetime measurements of the stored ions.

In this dissertation, the correction method for the anisochronism effect with a cavity doublet is outlined. An innovative design of the position cavity is then introduced, which offsets the cavity from the central orbit and exploits the resonant monopole mode. Based on this concept, a rectangular and an elliptic cavity are investigated by analytic and numerical means in compliance with the machine parameters of the Collector Ring. Afterwards, two scaled prototypes are tested on an automatic test bench with great efficiency and accuracy. The results are then compared with the simulations and found to be in good agreement.

Zusammenfassung

Ein Schwerionen-Speicherring kann durch eine spezielle Ionenoptik als isochrones Massenspektrometer betrieben werden. Jedoch kann aufgrund der großen Impulsakzeptanz des Rings die Isochroniebedingung nicht für alle gespeicherten Ionen erfüllt werden, wodurch die Messgenauigkeit beschränkt ist. Der Effekt der Anisochronie kann zwar durch Messen der Geschwindigkeit jedes einzelnen Ions mit zwei Flugzeitdetektoren korrigiert werden, jedoch ist die Anzahl der messbaren Ionen durch diese Detektionsmethode deutlich beschränkt. Als ein komplementärer Ansatz wird vorgeschlagen, die magnetische Steifigkeit der umlaufenden Ionen zerstörungsfrei gleichzeitig mit einer intensitätssensitiven und einer positionsempfindlichen Kavität zu messen, um diese Einschränkung zu überwinden. Darüber hinaus ermöglicht dieser Ansatz die simultane Messung der Lebenszeiten der gespeicherten Ionen.

In dieser Dissertation ist die Methode zur Korrektur des Anisochronieeffekts durch ein Kavitätsdublett dargestellt. Es wird ein innovatives Design der positionsempfindlichen Kavität vorgestellt, wobei die Kavität gegenüber dem zentralen Orbit versetzt ist und die resonante Monopol-Mode verwendet wird. Aufbauend auf diesem Konzept wird eine rechteckige und eine elliptische Kavität analytisch und numerisch unter Berücksichtigung der Maschinenparameter des Collector Rings untersucht. Daraufhin werden zwei skalierte Prototypen an einem automatisierten Messaufbau mit hoher Effizienz und Genauigkeit getestet. Die Ergebnisse werden mit den Simulationen verglichen und eine gute Übereinstimmung festgestellt.

CONTENTS



I	Introduction	1
1.1	Nuclear Physics at Storage Rings	2
1.1.1	Nuclear Mass	2
1.1.2	Nuclear Lifetime	3
1.1.3	Beta-Delayed Neutron Emission	4
1.2	Mass Measurement with Storage Rings	5
1.2.1	Schottky Mass Spectrometry	5
1.2.2	Isochronous Mass Spectrometry	7
1.2.3	Schottky Spectroscopy in Isochronous Mode	8
1.3	Motivation	8
2	Cavity Basics	10
2.1	Standing Wave Cavity	10
2.2	Detuning by Perturbations	13
2.3	Figures of Merit	14
2.4	Power Coupling	17
2.4.1	Coupling Schemes	17
2.4.2	Frequency Spectrum of Coupled Signal	18
2.5	Correction for Anisochronism Effect	21
3	Conceptual Design	24
3.1	Historical Perspective	24
3.2	Design Criteria	27
3.2.1	Isochronous Modes of Collector Ring	27
3.2.2	Requirement Specifications	28
3.3	Analytic Sketch	30
3.3.1	Rectangular Cavity	30
3.3.2	Elliptic Cavity	32
3.4	Computational Refinement	36
3.4.1	Apertures with Beam Pipes	37
3.4.2	Higher-Order Modes	38
3.4.3	Installation of Plungers	41
4	Empirical Justification	44
4.1	Prototype Cavities	44
4.2	Scattering Parameters	46
4.3	Static Test	48

4.3.1	Test Bench Setup	48
4.3.2	Debut of Prototypes	50
4.3.3	Drift of Resonant Frequency	52
4.3.4	Determination of Relative Permittivity	53
4.3.5	Detuning by Plungers	55
4.3.6	Damping of Higher-Order Modes	56
4.4	Dynamic Test	57
4.4.1	Test Bench Setup	57
4.4.2	Profiling Detuned Frequency	59
4.4.3	Profiling Electric Field	60
4.4.4	Profiling Shunt Impedance	61
5	Conclusion	67
A	Maxwell's Equations	70
A.1	Cartesian Coordinate System	71
A.2	Cylindrical Coordinate System	73
A.3	Elliptic Cylindrical Coordinate System	74
A.3.1	Elliptic Coordinate System	74
A.3.2	Mathieu Functions	76
B	Engineering Drawings	79
	Bibliography	86

1 INTRODUCTION



Heavy-ion storage rings have continually been advancing research in nuclear, atomic, and molecular physics. When coupled to radioactive beam facilities, they offer unprecedented opportunities for a close study of moderately and highly charged ions of exotic nuclei, especially in the relativistic regime. For a comprehensive review, see e.g. [1–4].

As of 2015, there exist two heavy-ion storage rings in operation around the world—the Experimental Storage Ring (ESR) at GSI in Darmstadt [5], and the experimental Cooler Storage Ring (CSR_e) at IMP in Lanzhou [6]. The schematic layouts of the former and the latter are illustrated in figs. 1.1 and 1.2, respectively. Both facilities are able to produce, accelerate, and store a broad spectrum of nuclides from the lightest hydrogen to the heaviest uranium. Meanwhile a handful of new rings that particularly aim at exotic nuclei and molecular clusters of experimental interest in various regions of the nuclear chart are coming online in the near future. See chapter 5 for more details.

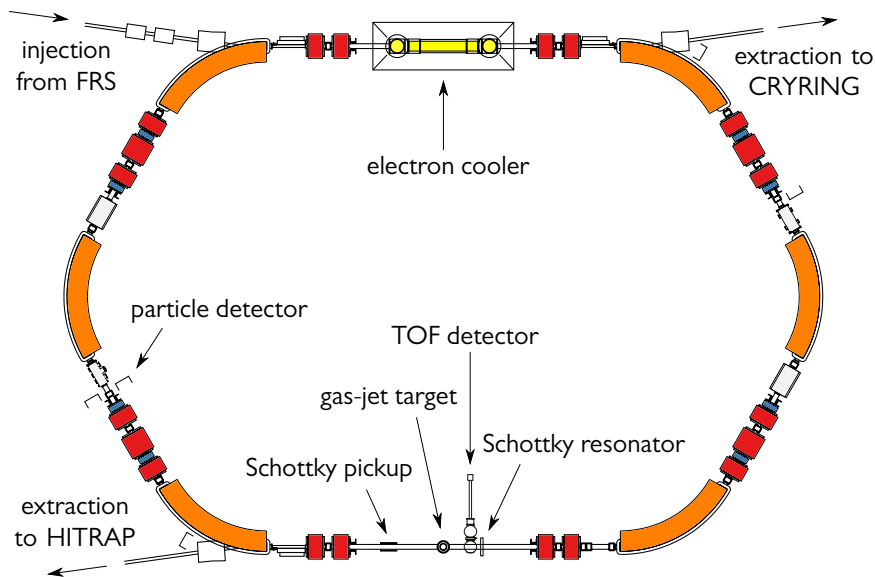


Figure 1.1 Schematic layout of the ESR. The ring has a circumference of 108.36 m and a maximum magnetic rigidity of 10 T·m. Apart from the essential lattice magnets for steering the beam, it is also equipped with an electron cooler for the electron cooling, as well as a pickup and a kicker station for the stochastic cooling. Moreover, several experimental apparatus are installed into the ring as well. Shown in the layout are gas-jet target, in-ring Time-Of-Flight (TOF) detector, capacitive Schottky pickup, cavity-based Schottky resonator, and five particle detectors housed in pockets integrated into the vacuum chamber.

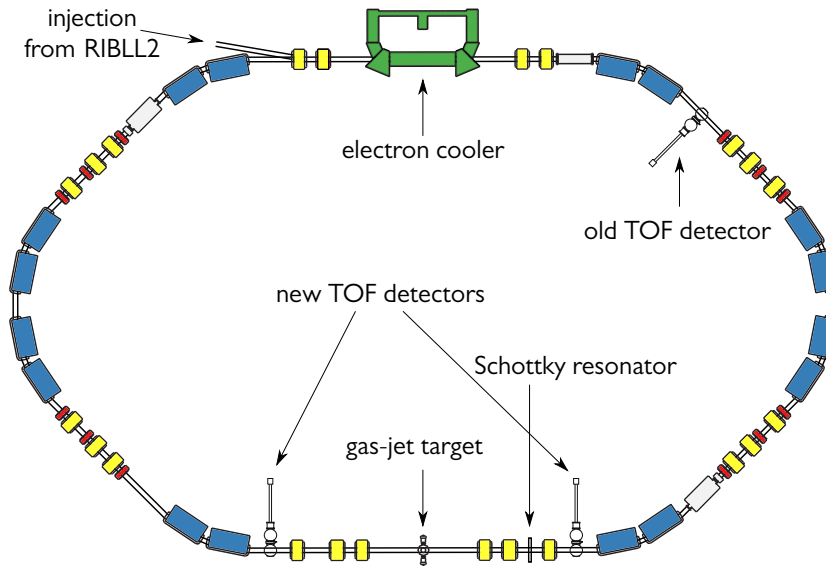


Figure 1.2 Schematic layout of the CSRc. The ring has a circumference of 128.8 m and a maximum magnetic rigidity of 8.4 T·m. An electron cooler has been installed already, yet a stochastic cooling system is in development. For the experimental purpose, a gas-jet target, a cavity-based Schottky resonator, and a Time-Of-Flight (TOF) detector are also installed into the ring. Together shown in the layout are a pair of newly deployed TOF detectors in a straight section.

1.1 Nuclear Physics at Storage Rings

A storage ring can turn into a mass spectrometer with a special ion-optical setting and/or incorporating beam-cooling techniques [7]. Due to the large momentum acceptance of the ring [8], cocktail beams, which consist of ions of various species, can be stored simultaneously in the ring. This allows for direct ion identifications and in situ mass calibrations, thus leads to a great mass resolving power (10^5 – 10^6) and a fine mass measurement precision (10^{-6} – 10^{-7}) [9, 10].

On the other hand, a storage ring can be employed for the study of decay spectroscopy when it is equipped with time-resolving detectors [11–13]. Due to its ultra-high vacuum (10^{-10} – 10^{-12} mbar) [8], stored ions can survive sufficiently long in the ring against atomic charge exchange reactions with the residual gas unless they decay first. Various kinds of radioactive (e.g. α - and β -) decays have extensively been investigated mainly at the ESR for the last two decades [2]. A measurable range of nuclear lifetimes from a few tens of microseconds to several decades has been achieved there [14–16].

Investigations on the β -delayed nucleon emissions are also feasible with a storage ring, of which a special case— β -delayed neutron emission—was already proposed for the ESR and the envisaged Collector Ring (CR) at FAIR [17].

1.1.1 Nuclear Mass

The nuclear mass is a direct observable of the complex interplay among strong, weak, and electromagnetic interactions inside a nucleus. As an experimental criterion, it is used to examine the validity and reliability of a nuclear structure theory [18]. Through such an inspection, the discrepancy between measured and predicted mass values often led to a new discovery. For instance, the nuclear shell closure at nucleon numbers of 20, 50, 82, and 126 was discovered [19] by comparing measured masses at that time with the liquid drop model [20]. Nuclear masses are also essential in astrophysics for modeling the processes of nucleosynthesis, stellar evolution, and stellar explosion [21]. After F. W. Aston precisely measured the masses of hydrogen and helium [22], A. S. Eddington soon realized that the mass defect

of helium could explain the origin of the solar energy [23].

Nowadays, the measured nuclear mass surface is mapped towards the nucleon drip-lines, owing to the advancement of precision mass spectrometry by means of ion trapping. Not only will this impose stringent tests on theoretical predictability, but also peculiar phenomena may emerge [24–28]. Two complementary approaches via Penning traps and storage rings are intensively exploited in order to investigate ions in great detail. While the mass measurements of radioactive nuclei with a Penning trap usually deliver high-precision results (10^{-7} – 10^{-8}), the masses of short-lived nuclei with lifetimes of the order of submillisecond can be measured with a storage ring. In this chapter, emphases are focused on the investigations on nuclear properties with storage rings. For a comprehensive review on the physical experiments with Penning traps, see e.g. [29, 30].

One of the remarkable achievements by virtue of storage rings may be attributed to the mass measurement of ^{208}Hg , of which only one hydrogen-like ion was recorded throughout an entire two-week experiment at the ESR [25]. The measured mass is the last missing piece of information for computing the average proton-neutron interaction strength, δV_{pn} , of ^{210}Pb . It is found that δV_{pn} of ^{210}Pb is about 2.5 times smaller than that of the doubly magic ^{208}Pb , which is consistent with the theoretical prediction. The result suggests that possible shell quenching and new shell closure in the nuclear region far from β -stability could be investigated by examining δV_{pn} .

In nuclear astrophysics, experimental masses of exotic nuclei measured with storage rings are crucial for constraining the pathways of the rapid neutron-capture process (r-process) for the neutron-rich nuclei [31], and of the rapid proton-capture process (rp-process) for the proton-rich nuclei [32]. The mass of the proton-unbound ^{65}As measured at the CSRe decisively concludes that ^{64}Ge is most likely not a waiting point—a nucleus can capture no more protons, thus must wait for β -decay—in the evolution of X-ray bursts [33]. Another marvelous result delivered at the CSRe is the mass of ^{45}Cr , which rejects the hypothesis on the Ca-Sc cycle formed along the rp-process path [34].

In contrast to the β -stability, which exists in the ground states of nuclei, there is also a metastability found in the excited states, usually termed as isomers [35]. The conventional technique for detecting such an isomer is the gamma spectroscopy by correlating the production of the isomer with emitted photons from its de-excitation. Due to the accidental background correlation, this method is limited in the short half-lives of isomers with an upper bound of one millisecond [36, 37]. As a complementary technique, the mass spectrometry at a storage ring is able to identify an isomer by detecting the mass difference from its ground state with almost no upper limits in time [38–40]. In addition, the de-excitation to the ground state can be observed within the storage, hence the lifetime can simultaneously be determined [41–44].

1.1.2 Nuclear Lifetime

The pursuit of nuclear β -decay of highly charged nuclei was actually one of the driving forces that motivated the construction of the ESR [45]. This is of particular importance for a better understanding of the nucleosynthesis taking place in the stellar interiors. It is generally believed that the stellar nucleosynthesis proceeds in a hot environment (30–100 keV), where few or even zero electrons are bound to a nucleus [46]. Under such an extreme condition, the β -decay of a nucleus could behave differently than in the neutral atom. For instance, the decay channel of the orbital electron capture (EC) is completely shut off for a bare ion, while the bound state β -decay (β_{b}^{-}) could become energetically possible [47].

A series of pilot experiments addressing nuclear lifetimes were conducted at the ESR, and had demonstrated the great success of its commissioning. It was revealed in 1992 that although a neutral ^{163}Dy is stable against any radioactive decay, a fully ionized $^{163}\text{Dy}^{66+}$ can β_{b}^{-} -decay into either the K or the L shell of its daughter nucleus $^{163}\text{Ho}^{66+}$. This discovery marked the first observation of the β_{b}^{-} -decay [48]. The reported half-life of 48(3) d set an upper limit (275 eV) on the mass of the electron neutrino [49]. Another experiment in the same campaign was the decay study on the bare ^{187}Re , which

had a profound impact on the galactic chronology [16]. Once all the orbital electrons are stripped off from ^{187}Re , the β_{b}^- -decay can drastically reduce the half-life by more than 9 orders of magnitude. The measured half-life of 32.9(20) a led to a more accurate estimate of the age of our Galaxy.

Due to the large momentum acceptance of a storage ring, various decay channels—such as EC, β^+ , β_{b}^- , and the continuum state β -decay (β_{c}^-)—may distinctly be observed, and the corresponding lifetimes can selectively be measured. As a merit, the branching ratio of a certain decay channel can be determined without ambiguity [50]. Some initiatives have been made at the ESR, and the results are extraordinary [51–56]. A selected list includes:

- The pure β^+ branches were measured for the bare $^{52\text{g}}\text{Fe}$ and $^{53\text{g}}\text{Fe}$, and the sum of β^+ and branches were measured for the bare $^{52\text{m}}\text{Mn}$ and $^{53\text{m}}\text{Fe}$ [51];
- The ratio of β_{b}^- - to β_{c}^- -decay rates was determined for the bare ^{207}Tl [53];
- One-half enhancement of the EC decay rate was revealed for the hydrogen-like ^{140}Pr and ^{142}Pm with respect to the helium-like counterparts [54, 55].

Beta decay can also be investigated on an event-by-event basis, from which the single-ion decay spectroscopy stems. By virtue of a Schottky resonator—a Radio Frequency (RF) cavity that detects the statistical Schottky noise of ions—with an extraordinary sensitivity and a fine time resolution [11], the fates of stored ions can be tracked for each particle. The lifetime is deducible by counting the decay events as a function of elapsed time. Surprisingly, a sinusoid-modulated exponential curve with a period of about 7 s was observed for two kinds of ions, namely $^{140}\text{Pr}^{58+}$ and $^{142}\text{Pm}^{60+}$ [57]. This peculiar phenomenon immediately stimulated an intense debate about the possible origin in the physics community, as the modulation is not predicted within the present knowledge about the electroweak interaction. So far, no conclusive explanations have been agreed on. For more details, see [57–59] and references cited therein.

In addition to β -decay, systematic studies on α -decay of heavy nuclei in high atomic charge states have been proposed for the ESR to address the electron screening effect on the α -emitters [60, 61]. It is predicted that the decay constant will be affected by a few thousandths, which is an important parameter in nuclear astrophysics for the understanding of nuclear reactions at stellar energies. Although several preparatory tests have been performed at the ESR, the schedule for the whole program is not yet clear [62].

1.1.3 Beta-Delayed Neutron Emission

For a neutron-rich nucleus, if the β -decay energy exceeds the neutron separation energy of the corresponding daughter nucleus, the latter may de-excite by emitting a neutron rather than a high energy photon [63]. This process is named β -delayed neutron emission (β_{n}^-). It starts to play a role in the freeze-out phase of the r-process, where the neutron source ceases and the synthesized nuclei β -decay back to the stability [64]. Astrophysical models have shown that β_{n}^- is imperative to moderate the staggering in the simulated abundance curve of the nuclides, so as to be consistent with the observation [65]. Also, the experimental data of the β_{n}^- -decay are important for the safety control in nuclear reactors, in particular throughout the shutdown stage [66].

A storage ring is suitable for studying the β_{n}^- -decay as well [67]. The mother ions can be monitored by a Schottky resonator, while the daughter ions can be intercepted by particle detectors housed in pockets next to the vacuum chamber (fig. 1.1) [68]. Note that this detection scheme was successfully demonstrated at the ESR, where $^{207}\text{Pb}^{81+}$ and $^{207}\text{Pb}^{82+}$ were measured by an capacitive Schottky pickup and a particle detector on the inner side in an arc section, respectively [53]. In the CR, two opposite pocket positions are foreseen in the middle of both arc sections. With the neutron-rich secondary beam

provided by the FAIR, investigations on the β_n^- -decay will become one of the highlight experimental programs addressed at the CR.

1.2 Mass Measurement with Storage Rings

A storage rings is a trapping device in which ions circulate periodically for an extended period of time. The revolution frequency f_{rev} of an ion depends on its mass-to-charge ratio m/q and velocity v . The quantitative relation among their relative deviations can, to a first-order approximation, be formulated as [7]

$$\frac{\delta f_{\text{rev}}}{f_{\text{rev}}} = -\frac{1}{\gamma_t^2} \frac{\delta(m/q)}{(m/q)} + \left(1 - \frac{\gamma^2}{\gamma_t^2}\right) \frac{\delta v}{v}, \quad (1.1)$$

where γ is the relativistic factor and γ_t is the transition energy of the ring, which is governed by the ion optics.

It is clear in eq. (1.1) that f_{rev} is influenced not only by m/q , but also by v . That is to say, the revolution frequencies of ions of the same kind are subject to their velocity spread in the ring. In order to turn a storage ring to a precision mass spectrometer, the influence from the second term in eq. (1.1) has to be minimized. To this end, two distinct approaches have been exploited by:

- reducing the velocity spread $\delta v \rightarrow 0$ by means of beam coolings [69–71];
- operating the ring at the transition energy $\gamma - \gamma_t \rightarrow 0$ [72].

These two approaches correspondingly give rise to the *Schottky Mass Spectrometry* (SMS) and the *Isochronous Mass Spectrometry* (IMS). The harvest of nuclear masses measured with two complimentary techniques at the ESR and CSRe is compiled into fig. 1.3.

1.2.1 Schottky Mass Spectrometry

The SMS is named after W. Schottky, who first discovered a new kind of noise when he was studying the fluctuation of electron current in a vacuum tube [74]. The noise arose from the finite number of randomly distributed electrons in the current. Later, it was revealed that proton beams in the Intersecting Storage Rings (ISR) at CERN also exhibit such a noise [75]. Usually, the Schottky noise of an ion beam in a storage ring is non-interceptively coupled by a pickup, followed by amplifications, and finally analyzed in frequency domain by the Fourier transformation. Among the vast information contained in a Schottky noise spectrum [76], the revolution frequency of the ion and the corresponding momentum spread are of the SMS' concern [77]. In order to enhance the mass resolving power and improve the measurement precision, the momentum spread is to be reduced by applying various cooling techniques to the beam.

Beam Cooling

The purpose of cooling is to contract the beam distributions in size and momentum, i.e. to increase the phase space density. So far, three cooling techniques—laser cooling, electron cooling, and stochastic cooling—have successfully been applied to hot ions in a storage ring [78].

The laser cooling slows ions down by virtue of radiation pressure. The method was first proposed by T. W. Hänsch and A. L. Schawlow [69]. When a laser is illuminated head-on towards an ion beam, an absorption resonance will appear once the Doppler-shifted laser frequency coincides with one of the atomic transitions of the ions. Shortly after that, the ions will de-excite by emitting photons isotropically in their own co-moving frame. Effectively, the ensemble of ions receives unidirectional momentum transfer. Due to the Doppler resonance, fast ions are decelerated while slow ions are nearly intact.

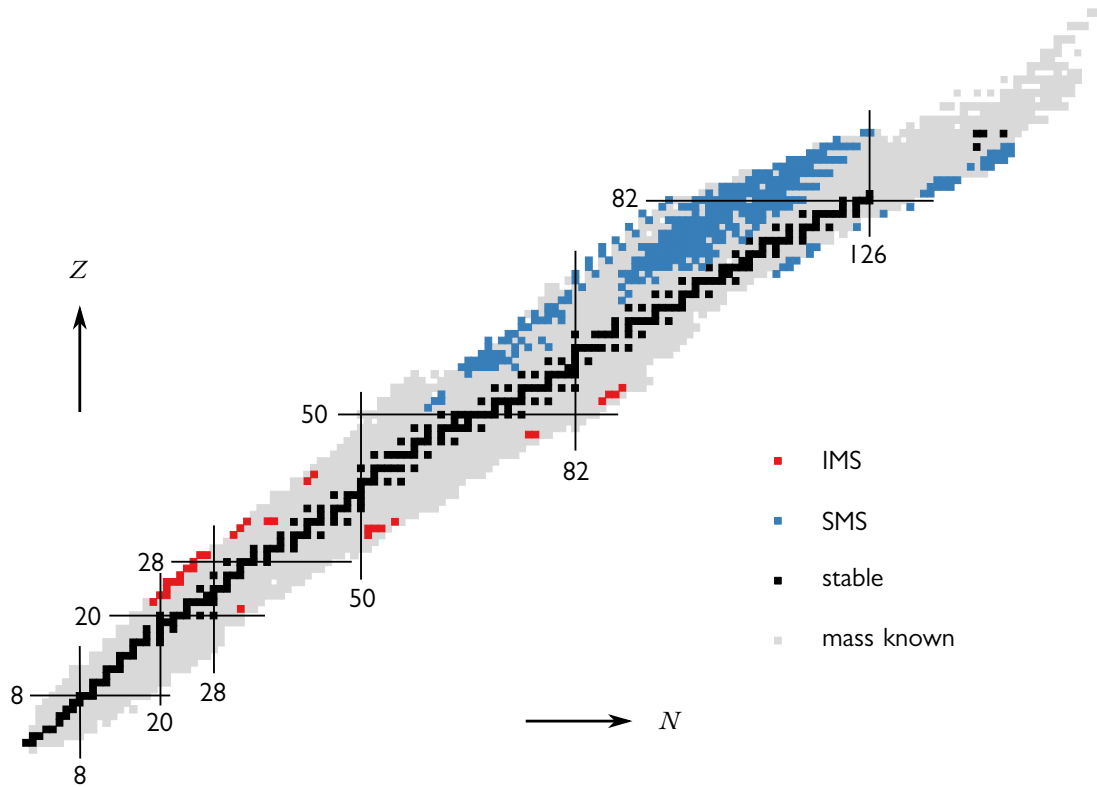


Figure 1.3 Chart of the nuclides featuring the achievements of the mass measurements at the ESR and CSRe. Each square denotes a nuclide. The blue ones are the nuclides whose masses were measured via the Schottky Mass Spectrometry (SMS), while the red ones were measured via the Isochronous Mass Spectrometry (IMS). The stable nuclides are colored in black. The gray squares are the nuclides with experimentally known masses according to the latest Atomic Mass Evaluation (AME2012) [73]. (Adapted from [1].)

By sweeping the laser frequency, the velocity spread of ions can gradually be reduced [79]. However, the laser cooling is not a versatile technique, because of a limited number of available laser frequencies and the request for bound electrons.

The idea of using a cold electron beam to cool a hot ion beam was conceived by G. I. Budker [71]. A well collimated, monochromatic electron beam prepared from a cathode is merged with an ion beam, of which the mean velocity should be matched to that of the electrons. A plasma is hence formed in the overlapping region. The Coulomb interaction inside the plasma tends to equilibrate the temperatures of the electrons and ions. The heated electrons are attracted by the anode and then collected by the collector, while fresh and cold electrons are continuously injected from the cathode. Eventually the ion beam will end up with the same velocity as that of the electron beam [80]. The electron cooling is a universal method that can even be applied to bare ions. However, it is not so efficient for very hot ion beams, since the cooling time is proportional to the cube of the velocity spread, i.e. $T_{\text{cool}} \propto \delta v^3$.

The stochastic cooling was invented by S. van der Meer [70]. It requires a pickup and a kicker station carefully arranged along the ring. The distance between them is a quarter, possibly plus half-integers, wavelength of the betatron oscillation, such that the position displacement at the pickup station can be translated to the impulse at the kicker station to correct the orbit. By this means, the betatron oscillation gets damped. A similar principle can be applied to the longitudinal direction as well [81]. This technique is designed for a certain ion velocity though, the total phase space volume can be reduced significantly within one second. It is often adopted as a pre-cooling to save the subsequent electron cooling time due to the cubic dependence on the velocity spread [82]. For a typical mass measurement, the cool-

ing cycle of a secondary beam is about a few seconds, and the momentum spread can, after undergoing the phase transition to a one-dimensionally ordered beam, be narrowed down to 2×10^{-7} [83].

1.2.2 Isochronous Mass Spectrometry

In the case of IMS, the storage ring is tuned to a special ion-optical mode, namely the isochronous mode, usually with a smaller transition energy γ_t to fall into the energy range of stored ions. For the ions that fulfill the isochronism condition $\gamma = \gamma_t$, the orbital change compensates the velocity deviation so as to retain the same revolution frequency [84]. As a side effect of the isochronous setting, the dispersion function becomes larger, which suppresses the momentum acceptance of the ring by up to one order of magnitude compared to the one in the standard mode [85].

Nevertheless, the IMS is preferable to the SMS for short-lived exotic nuclei, since no cooling procedures are employed. The revolution timestamps of every ion inside the ring are registered by a Time-Of-Flight (TOF) detector, which comprises a very thin carbon foil coated with cesium iodide, and a Micro-Channel Plate (MCP) [12, 13]. At each time when the ion penetrates the foil, secondary electrons are released from the surface and guided to the MCP, signaling the completion of one lap. Due to the energy loss in the foil, any ion can only circulate about one millisecond till it terminate on the vacuum chamber [2]. Fortunately, two-hundred-microsecond data are enough to determine the revolution frequencies with sufficient precisions to allow for competitive mass measurements of the nuclei [86].

In practice, the isochronism condition cannot strictly be fulfilled for a broad spectrum of nuclides because of the *anisochronism effect* [87]. This effect can broaden peak widths in the revolution time spectrum, and may even distort the Gaussian shape of some peaks for the ions that are considerably off the transition energy [88], which imposes systematic errors on the mean revolution times. Therefore, precision measurements necessitate corrections for the anisochronism effect.

Anisochronism Effect

Generally speaking, the anisochronism effect stems from two sources, namely the chromatic aberration of the ion optics and the diversity of the stored ion species [89]. The former is extrinsic whereas the latter is intrinsic.

For a realistic storage ring, imperfections—such as misalignment, fringe field, and closed-orbit distortion—are inevitable. All of these factors contribute to a variable transition energy, i.e. γ_t depends on the revolution orbit. The imperfections can be corrected by introducing higher-order fields in the ring. Much effort is being devoted to the optimization of the magnetic lattices in various storage rings [90, 91].

Even if γ_t stays constant, the anisochronism still takes effect for most kinds of ions. It is clear in eq. (1.1) that the isochronism condition can only be fulfilled for a specific species with a certain γ (fig. 1.4). In other words, the revolution times for other species are smeared out due to the inevitable momentum spreads. The asymmetric distribution of the magnetic rigidities of ions, which can often happen due to the production mechanism and transmission scheme, will also distort the peak shape in the revolution time spectrum. Therefore, additional means are required to ensure precise and accurate measurement results.

One way could be to restrict the magnetic rigidities of the injected ions by placing a slit in the fragment separator upstream from the storage ring. This so-called $B\rho$ -tagging method was successfully demonstrated at the ESR (fig. 1.4) [88]. The result showed that the mass resolving power was improved by up to one order of magnitude and the accuracy was more than twice better. However, a drawback of this method was the strong reduction of the transmission efficiency.

Meanwhile, it was proposed to determine the velocity of each ion inside the ring in parallel to

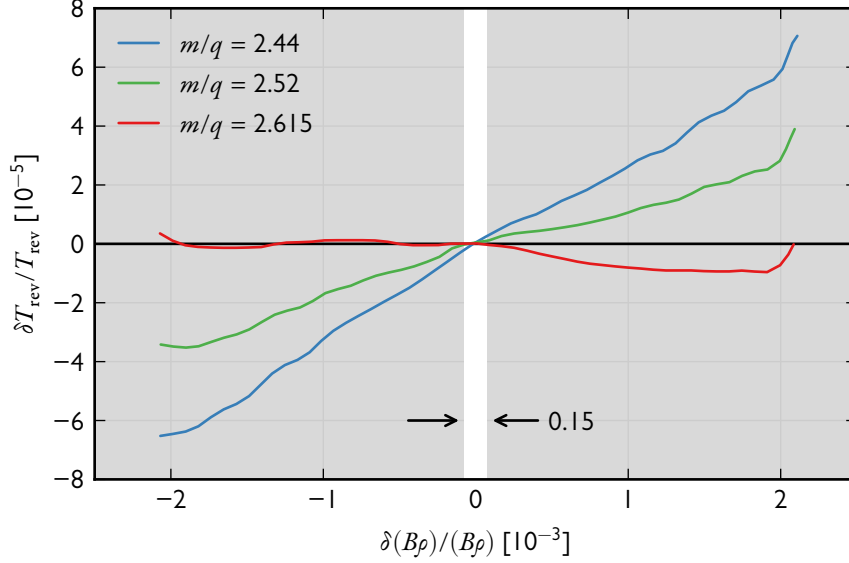


Figure 1.4 Isochronism curves of the ESR for ions with different mass-to-charge ratios. The abscissa is the relative change of the magnetic rigidity of an ion species, while the ordinate is the relative change of its revolution time. The red curve was measured by sweeping the voltage of the electron cooler when the ESR was operated in the isochronous mode. The blue and green ones were deduced by assuming the identical orbital length for ions with the same magnetic rigidity. The white band in the middle indicates a selected window of the $B\rho$ -tagging method to restrict the momentum spread of the ions during that experiment. (Adapted from [88].)

the measurement of its revolution time [92]. Later, this approach was realized at the CSRe with two newly installed TOF detectors in a straight section (fig. 1.2). The mass resolving power is expected to increase significantly. Since this method does not constrain the transmission efficiency, it is in particular advantageous for the nuclei with extremely low yields.

1.2.3 Schottky Spectroscopy in Isochronous Mode

The successful commissioning of an intensity-sensitive and time-resolving Schottky resonator at the ESR (fig. 1.1) has opened up an innovative window towards the Schottky spectroscopy in the isochronous mode [11]. Investigations on nuclear masses and lifetimes could be addressed at a storage ring simultaneously with almost no upper limits in time. In particular, the fast response and fine resolution of the Schottky resonator allow for the measurements of short-lived nuclei with lifetimes of the order from millisecond to second, which fills the gap left by the IMS and SMS.

Figure 1.5 shows a Schottky power spectrogram from a pilot experiment conducted at the ESR in the isochronous mode [93]. A mass resolving power of 10^5 was achieved, which was comparable to that obtained with a TOF detector. The traces of the helium-like $^{213}\text{Ra}^{86+}$ and hydrogen-like $^{213}\text{Fr}^{86+}$ can neatly be separated in fig. 1.5, while the time resolution is merely 32 ms.

1.3 Motivation

Having demonstrated the potential of the Schottky spectroscopy in the isochronous mode, the Schottky resonator also inspired a cavity-based method to correct for the anisochronism effect. By additionally employing a position-resolving cavity at the dispersive location of the ring, the revolution orbits—and hence the magnetic rigidities—of the stored ions can be distinguished. Recalling the defi-

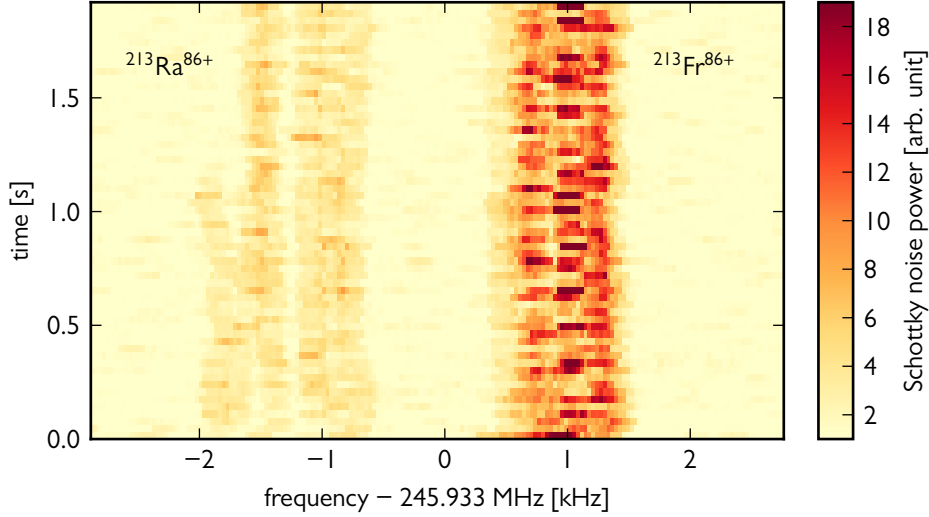


Figure 1.5 Schottky power spectrogram of two ion species in the ESR when it was operated in the isochronous mode. The signal was detected by an intensity-sensitive and time-resolving Schottky resonator, and displayed at a higher harmonic of the revolution frequency. On the left hand side, a single ion of $^{213}\text{Ra}^{86+}$ can unambiguously be identified, since the trace is abruptly terminated due to decay.

nition of the magnetic rigidity:

$$B\rho = \gamma v \left(\frac{m}{q} \right), \quad (1.2)$$

essentially, the velocities of the ions are measured. Similar to the double-TOF technique, the correction for the anisochronism effect can thus be applied with an intensity and a position cavity.

It is important to note that the cavity-doublet technique excels in several aspects due to its non-interceptive detection nature and broad dynamic range of the detectable signal strength. Every stored ion above a certain charge threshold can be detected by the cavity doublet without interfering the motion of the ion. On the contrary, the carbon foils of the TOF detectors obstruct the revolutions of the ions such that the latter can survive no longer than half a millisecond, irrespective of their intrinsic radioactive properties, which consequently sets an upper limit on the measurable lifetimes. The size of the foil also imposes a practical constraint on the acceptance of the ring, and hence a stringent requirement on the lattice magnets. Moreover, the TOF detection efficiency will strongly be suppressed by dozens of ions passing through the foil in one shot, because the arrival time of each ion is hardly possible to identify from the superposed multi-particle signal [94]. An even larger beam intensity will harm the foil and could permanently damage it. Therefore, in spite of the acceptance of the ring and the yields of the secondary nuclei, the total number of stored ions at each injection is carefully controlled for the TOF-based IMS. In contrast, this will not be the case for the cavity doublet, and in fact, high-intensity beams are more favored to efficiently accumulate statistics.

To surpass the limits of the double-TOF technique, the feasibility of using a cavity doublet for the isochronous mass measurements has been explored. The thorough details about the principle of the position detection by a cavity, the methodology of the correction for the anisochronism effect, the design of position cavities, and the benchtop test of prototypes are put forward in the rest of this dissertation.

2 CAVITY BASICS



An ideal cavity is a void space enclosed by conducting walls, in which ElectroMagnetic (EM) fields are confined. In practice, additional holes exist on the walls to allow for coupling the cavity with the surroundings [95]. The RF Cavity is a key device that can commonly be found on any linear or circular accelerator. It is used to interact with beams, mainly, with its electric field.

Nowadays, there are enormous cavities of different kinds deployed to serve numerous purposes [96]. Based on the wave mode, they can be divided into travelling wave cavities (high acceleration efficiency) and standing wave cavities (high detection sensitivity). Based on the electrical conductivity of the walls, there are normal-conducting cavities (room temperature) and superconducting cavities (cryogenic environment). Based on the direction of the EM energy flowing through the couplers, a cavity can be either a beam diagnostic device (e.g. current monitor, position monitor), or a beam manipulating device (e.g. acceleration cavity, crab cavity, buncher, chopper). Based on the orientation of the EM fields, a cavity can have Transverse Magnetic (TM; great coupling strength with beams), Transverse Electric (TE; little power loss on walls), and Transverse ElectroMagnetic (TEM; mostly used in low frequency regime) fields.

Due to the practical reason that the new position cavity is intended to detect relativistic single ions, only the standing wave cavity in the TM modes are treated henceforth.

2.1 Standing Wave Cavity

A typical standing wave cavity exhibits a cylindrical shape with various cross sections (e.g. circular, rectangular, and elliptic). In order to allow for the beam passage, a pair of opposite apertures are usually machined on both flat ends of the cavity. In contrast, couplers are usually mounted on the curved wall.

For the sake of simplicity, first consider a fully closed cavity without any holes in it. According to classical electrodynamics, the EM fields inside a source-free cavity is governed by the homogeneous Maxwell's equations [97]:

$$\nabla \cdot \tilde{\mathbf{E}} = 0, \quad (2.1)$$

$$\nabla \cdot \tilde{\mathbf{H}} = 0, \quad (2.2)$$

$$\nabla \times \tilde{\mathbf{E}} = -\mu_0 \frac{\partial \tilde{\mathbf{H}}}{\partial t}, \quad (2.3)$$

$$\nabla \times \tilde{\mathbf{H}} = \varepsilon_0 \frac{\partial \tilde{\mathbf{E}}}{\partial t}. \quad (2.4)$$

Further assume that the electrical conductivity of the walls is zero. This leads to the boundary condi-

tions:

$$\mathbf{n} \times \tilde{\mathbf{E}} = 0, \quad (2.5)$$

$$\mathbf{n} \cdot \tilde{\mathbf{H}} = 0. \quad (2.6)$$

Here, $\tilde{\mathbf{E}}$ is the electric field, $\tilde{\mathbf{H}}$ is the magnetic field, and \mathbf{n} is the normal vector to the boundary. Moreover, ε_0 and μ_0 are the permittivity and permeability in vacuum, respectively.

The general solutions of EM fields are too complicated to be written down. However, due to the linearity of eqs. (2.1) to (2.6), the principle of superposition holds: The sum of any two solutions is still a valid solution. Hence, one can designate some special solutions with the simplest form as the primitives, which are conventionally termed as *eigenmodes*, or *modes*. Thereafter, any solution can be expressed as a proper superposition of those modes [95]. Within the context of TM modes, the longitudinal component of the magnetic field vanishes. Instead, the electric field largely coincides with the beam path, which offers a strong coupling between the cavity and beam.

It can be shown that the explicit form of an eigenmode is the product of a sinusoidal temporal and a complex spatial function [97]. When expressed via the phasor notation, it reads

$$\tilde{\mathbf{E}}(\mathbf{x}, t) = \mathbf{E}(\mathbf{x})e^{-i\omega_0 t}, \quad (2.7)$$

$$\tilde{\mathbf{H}}(\mathbf{x}, t) = \mathbf{H}(\mathbf{x})e^{-i(\omega_0 t - \varphi)}, \quad (2.8)$$

where \mathbf{x} represents spatial coordinates, t is time, ω_0 is the *angular eigenfrequency*, and φ denotes the phase difference between the magnetic and electric field. The spatial functions \mathbf{E} and \mathbf{H} describes the EM field patterns in this mode at a particular moment. After taking the oscillating exponential factor into account, the EM fields are actually varying periodically. Consequently, standing waves are established inside the cavity.

The phase difference φ can be computed, for instance, by substituting eqs. (2.7) and (2.8) into eq. (2.3):

$$\nabla \times \mathbf{E} = i\omega_0 \mu_0 \mathbf{H}e^{i\varphi}. \quad (2.9)$$

Since both \mathbf{E} and \mathbf{H} are real, the imaginary part $ie^{i\varphi}$ on the right hand side of eq. (2.9) must cancel out. It appears that two values $\varphi = \pm\pi/2$ both fulfill the condition. In fact, they essentially describe the same scenario: either the magnetic field is $\pi/2$ behind the electric field, or the flipped magnetic field is $\pi/2$ ahead of the electric field. To avoid any possible confusions, $\varphi = \pi/2$ is adopted exclusively. In a similar manner, eq. (2.4) together with eqs. (2.7) and (2.8) leads to

$$\nabla \times \mathbf{H} = -\omega_0 \varepsilon_0 \mathbf{E}. \quad (2.10)$$

According to eqs. (2.5) and (2.6), the electric field must be perpendicular to the walls, and the magnetic field must be tangential. Otherwise, they have to vanish on the walls. Because of the fixed dimensions of the cavity, only particular wave patterns with certain wavelengths can fit into the cavity. Therefore, the eigenfrequency only takes some discrete values, which are determined by the dimensions of the cavity. In particular, two modes—namely monopole and dipole mode—are of practical interest. Their EM field patterns are illustrated in fig. 2.1, in the case of a pillbox cavity. The monopole mode can easily be excited with the strongest magnitude. The concentration of its electric field around the center makes it perfectly suitable for either the beam acceleration or the beam intensity detection. On the other hand, the dipole mode lies in frequency next to the monopole mode. The mirror symmetry of its EM fields is usually used for the beam position detection [98].

The stored energy inside a cavity is carried by the electric and magnetic field. The contribution from each part can be calculated by integrating the time-averaged energy density over the cavity volume

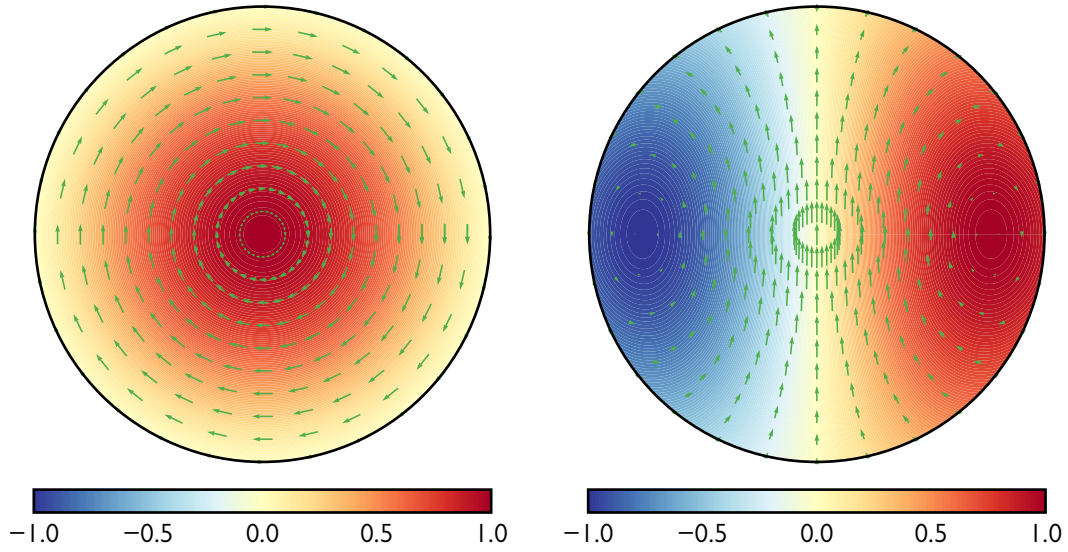


Figure 2.1 EM field patterns for the monopole mode (left) and the dipole mode (right) in a pill-box cavity. The fields are presented in a circular cross section perpendicular to the axial direction. The electric field strength is normalized and color-coded, where positive represents the field pointing out of the page and negative represents the opposite direction. The magnetic field is illustrated with arrows, of which the head points to the field direction and the length is proportional to the field strength.

V [95]:

$$W_e = \int_V dV \frac{1}{2} \operatorname{Re} \left(\frac{\epsilon_0}{2} \tilde{\mathbf{E}} \cdot \tilde{\mathbf{E}}^* \right) = \int_V dV \frac{\epsilon_0}{4} \mathbf{E}^2, \quad (2.11)$$

$$W_m = \int_V dV \frac{1}{2} \operatorname{Re} \left(\frac{\mu_0}{2} \tilde{\mathbf{H}} \cdot \tilde{\mathbf{H}}^* \right) = \int_V dV \frac{\mu_0}{4} \mathbf{H}^2, \quad (2.12)$$

where W_e and W_m are the time-averaged electric and magnetic energy, respectively. The asterisk denotes complex conjugate. By virtue of the vector identity

$$\nabla \cdot (\mathbf{E} \times \mathbf{H}) \equiv \mathbf{H} \cdot (\nabla \times \mathbf{E}) - \mathbf{E} \cdot (\nabla \times \mathbf{H}), \quad (2.13)$$

eqs. (2.9) and (2.10) jointly give rise to the difference between W_e and W_m :

$$W_e - W_m = \frac{1}{4\omega_0} \int_V dV \nabla \cdot (\mathbf{E} \times \mathbf{H}). \quad (2.14)$$

According to the divergence theorem, the volume integral on the right hand side of eq. (2.14) can be replaced by a surface integral:

$$W_e - W_m = \frac{1}{4\omega_0} \oint_A d\mathbf{A} \mathbf{n} \cdot (\mathbf{E} \times \mathbf{H}), \quad (2.15)$$

which essentially equals zero since $\mathbf{E} \times \mathbf{H}$ is, as a corollary of the boundary conditions, everywhere tangential to the surface A .

Because the electric field oscillates synchronously with the magnetic field with $\pi/2$ phase off, the same amount of energy is being transformed back and forth between these two kinds of fields. As one

reaches its maximum magnitude, the other fades out. The total energy W , on the other hand, remains constant:

$$W = W_e + W_m \quad (2.16)$$

$$= \int_V dV \frac{\epsilon_0}{2} \mathbf{E}^2 = \int_V dV \frac{\mu_0}{2} \mathbf{H}^2. \quad (2.17)$$

2.2 Detuning by Perturbations

The boundary of a cavity defines the configurations of the EM standing waves and their associated frequencies. Any deformation on the cavity walls will change the field patterns and, most probably, also the frequencies. The quantitative relation between an infinitesimal change (i.e. perturbation) of the boundary and the resultant frequency shift (i.e. detuning) was first derived by J. Müller [99], and then reformulated by J. C. Slater in a succinct form [100]:

$$\frac{\delta\omega}{\omega_0} = \frac{(\mu_0 \mathbf{H}^2 - \epsilon_0 \mathbf{E}^2) \delta V}{4W}. \quad (2.18)$$

Here, $\delta\omega = \omega - \omega_0$ is the *detuning angular frequency*, ω is the detuned angular frequency by the perturbation, and δV is the volume removed from the cavity. The EM fields \mathbf{E} and \mathbf{H} are the local values at δV . Once the boundary is pushed inwards, the frequency will increase if the magnetic field is stronger at the perturbed location, and decrease if the electric field is stronger there. Only in some rare situations where the electric and magnetic field balance, the frequency remains the same.

Equation (2.18) provides a useful guidance to designing a tuner for a cavity, in case the eigenfrequency of a specific mode needs to be altered in reality. Often, a cylindrical stub, or plunger in jargon, is mounted on the side of the cavity for the detuning. The frequency changes as the plunger is advanced or retracted. In general, the magnetic field is dominant on the edge in the TM modes, therefore, the plunger should preferably be placed at the location of the strongest magnetic field.

Apart from perturbing the boundary, a cavity can be detuned as well by inserting a dielectric object [101, 102]. This can be understood by imagining an exaggerative scenario where the cavity is filled with a dielectric medium. The speed of light in this medium is always smaller than that in free space, whereas the wavelength should not change since the boundary is the same. Consequently, the frequency, which is the ratio of the speed of light to the wavelength, must be smaller. In other words, under no circumstances may a dielectric object raise the frequency.

The simplified expression of the detuning frequency is, based on some reasonable stipulations, given as [101]

$$\frac{\delta\omega}{\omega_0} = -\frac{\epsilon_0(\epsilon_r - 1) \mathbf{E} \cdot \mathbf{E}' \delta V}{4W}, \quad (2.19)$$

where ϵ_r is the relative permittivity of the dielectric object, δV is its volume, and \mathbf{E} is the unperturbed electric field at where the object is placed while \mathbf{E}' is the perturbed one there. Likewise, eq. (2.19) is more accurate when the perturbing object is infinitesimally small.

In practice, eq. (2.19) finds its application in profiling the electric field strength inside a cavity. To this end, a small dielectric bead is usually used as the perturbing object due to its simple geometry. Let r_b be the radius of the bead. Recall that the electric field \mathbf{E}' within a sphere in a homogeneous external field \mathbf{E} is [102]

$$\mathbf{E}' = \frac{3}{\epsilon_r + 2} \mathbf{E}, \quad (2.20)$$

eq. (2.19) can, in the quasi-static approximation, be reformulated to

$$\frac{\delta\omega}{\omega_0} = -\frac{\pi\varepsilon_0(\varepsilon_r - 1)r_b^3\mathbf{E}^2}{(\varepsilon_r + 2)W}. \quad (2.21)$$

The usage of eq. (2.21) is dual: Either the relative permittivity of an unknown material can be characterized provided that the cavity dimensions are well controlled and the electric field is analytically clear; Or the electric field of a cavity under test can be determined with a well known bead. The size of the perturbing bead should be insignificant, such that eq. (2.21) can deliver accurate results. Calculations have shown that the ratio between the radii of the bead and cavity ought to be smaller than 0.083 to limit the error to no more than 1 % [102]. Additionally, the bead must be kept away from the walls in order to avoid the image charge effect, which will cause an extra amount of detuning frequency [103].

2.3 Figures of Merit

Due to the induction of the magnetic field inside a cavity, there exists an image current flowing on the inner surface of the metallic walls with the same magnitude as the beam current but in the opposite direction [104]. At room temperature, any metal has a nonzero resistivity, therefore the ohmic loss of the EM energy is inevitable. A dimensionless quantity, named *quality factor* Q_0 , is thus assigned to the cavity to characterize the capability of preserving the EM energy [105]:

$$Q_0 = \frac{\omega_0 W}{P_{\text{diss}}}, \quad (2.22)$$

where P_{diss} is the dissipated power on the walls, which can be expressed as

$$P_{\text{diss}} = -\frac{dW}{dt}. \quad (2.23)$$

It is then straightforward from eqs. (2.22) and (2.23) to find that W decays exponentially with a lifetime of Q_0/ω_0 . However, it should be noted that with the presence of the ohmic loss, the cavity is actually detuned from ω_0 . For a high- Q (10^3 and above) cavity, which is commonly used, the change is so small that it is often omitted.

In order to maintain the EM fields inside the cavity, energy compensation, either by an RF generator or by a beam, is obligatory. This scenario is essentially a driven oscillation, which can mathematically be modeled as [105]

$$\frac{d^2\mathcal{F}}{dt^2} + \frac{\omega_0}{Q_0} \frac{d\mathcal{F}}{dt} + \omega_0^2\mathcal{F} = D e^{-i\omega t}, \quad (2.24)$$

where \mathcal{F} represents either the electric field or the magnetic field, D is the amplitude of the driving force, and ω is the driving angular frequency. The solution to eq. (2.24) consists of a transient term which diminishes eventually, and a persistent term which oscillates at the driving frequency. The steady amplitude \mathcal{A} in the end is obtained by substituting an ansatz $\mathcal{F} = \mathcal{A}e^{-i\omega t}$ into eq. (2.24):

$$\mathcal{A} = \frac{D}{(\omega_0^2 - \omega^2) - i\omega_0\omega/Q_0}. \quad (2.25)$$

It can be seen from eq. (2.25) that $|\mathcal{A}|$ becomes maximum when $\omega = \omega_0$ (again, in the high- Q approximation). In other words, when the driving frequency is tuned to the eigenfrequency of the cavity, the strongest EM fields are excited inside the cavity. This phenomenon is named *resonance*. A cavity is therefore alias resonator. In the vicinity of the resonant frequency, eq. (2.25) can be approximated to

$$\mathcal{A} = \frac{\mathcal{A}_0}{-2iQ_0(\delta\omega/\omega_0) + 1}, \quad (2.26)$$

where $\mathcal{A}_0 = iDQ_0/\omega_0^2$ is the resonant amplitude.

The stored energy W is proportional to the square of the modulus of \mathcal{A} , which can be derived from eq. (2.26) as

$$W = \frac{W_{\max}}{4Q_0^2(\delta\omega/\omega_0)^2 + 1}, \quad (2.27)$$

where $W_{\max} \propto |\mathcal{A}_0|^2$ is the maximum EM energy. Equation (2.27) defines the *resonance curve* of the cavity, which has the shape of the Lorentzian distribution (fig. 2.2). The quality factor Q_0 can be

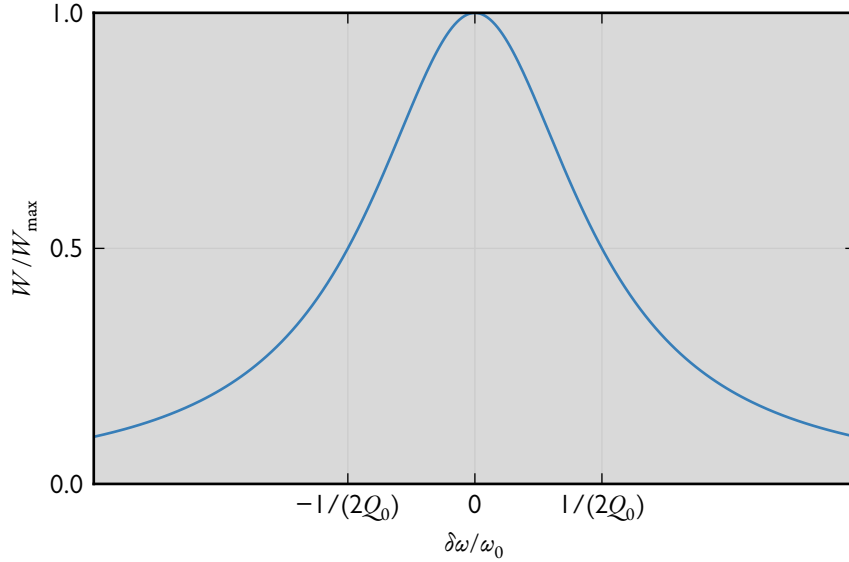


Figure 2.2 Schematic plot of the resonance curve of a cavity with a quality factor of Q_0 .

inferred from this curve via the Full Width at Half Maximum (FWHM):

$$Q_0 = \frac{\omega_0}{\Delta\omega_{\text{FWHM}}}. \quad (2.28)$$

In comparison with the quality factor, the ohmic loss on the cavity walls can also be characterized by a lumped resistor with an *effective shunt impedance* \tilde{R}_{sh} . It is defined as [95]

$$\tilde{R}_{\text{sh}} = \frac{|U_{\text{acc}}|^2}{P_{\text{diss}}}, \quad (2.29)$$

where U_{acc} is the *acceleration voltage* across the cavity gap. Note that for some historical reasons, two versions of the definition are widely used in parallel: One has a factor of one-half whereas the other does not. The one adopted here follows the convention from an early electron linac in Stanford [106].

The acceleration voltage is the amount of voltage a particle sees as it passes the cavity [107]. In contrast to a traveling wave cavity where the particle rides on the acceleration phase, the oscillation of the electric field in a standing wave cavity must be accounted for. Having said that, U_{acc} can be computed by integrating the longitudinal component of the electric field, $\hat{\mathbf{z}} \cdot \tilde{\mathbf{E}}$ with $\hat{\mathbf{z}}$ being the normalized axial basis vector, over the cavity depth d :

$$U_{\text{acc}} = \int_{-d/2}^{d/2} dz \hat{\mathbf{z}} \cdot \tilde{\mathbf{E}} \quad (2.30)$$

$$= \int_{-d/2}^{d/2} dz E_z(\mathbf{x}) e^{-i\omega_0 t(z)}. \quad (2.31)$$

Here, the time t is no longer an independent variable of the spatial coordinates. It is worth noting that in reality, any cavity has an aperture on each end to allow for the beam passage, which causes the EM fields to extend into the adjacent vacuum chamber. As a result, the lower and upper bound of the integral in eq. (2.31) should in principle be extended to $-\infty$ and $+\infty$, respectively. A practical measure is to take the bounds sufficiently far from the cavity where the EM fields are negligible. It is also emphasised in eq. (2.31) that the electric field varies with the transverse coordinates. Therefore, the acceleration voltage is position dependent, and so is the shunt impedance.

The asynchronism effect of a standing wave cavity on a particle can be characterized by the *transit time factor* \mathcal{T} . It is defined as the modulus of the acceleration voltage normalized to a fictional one where the particle sees a frozen electric field [107]:

$$\mathcal{T} = \frac{\left| \int_{-d/2}^{d/2} dz E_z e^{-i\omega_0 t} \right|}{\int_{-d/2}^{d/2} dz E_z}. \quad (2.32)$$

For the simple modes, such as monopole and dipole mode, E_z is uniform in the longitudinal direction. Consequently, eq. (2.32) can further be developed to

$$\mathcal{T} = \frac{1}{d} \int_{-d/2}^{d/2} dz \cos\left(\frac{\omega_0 z}{v}\right) \quad (2.33)$$

$$= \frac{T_0}{\pi t_{\text{tr}}} \sin\left(\frac{\pi t_{\text{tr}}}{T_0}\right), \quad (2.34)$$

where v is the velocity of the particle, $t_{\text{tr}} = d/v$ is the transit time for passing through the cavity, and $T_0 = 2\pi/\omega_0$ is the oscillation period of the electric field. It is clear in fig. 2.3 that \mathcal{T} is close to unity for a short transit time, which means a high acceleration efficiency. It becomes zero when t_{tr} is a multiple

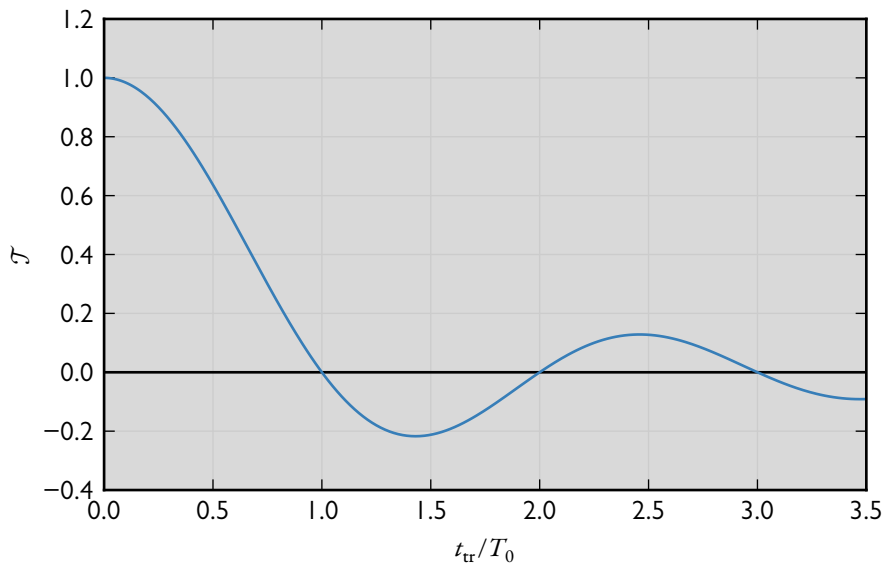


Figure 2.3 Transit time factor of a cavity as a function of normalized transit time of a particle.

of T_0 . It can even be negative for certain transit times, which means that the particle gets decelerated. The realistic design of a cavity should keep a short gap so as to attain a high transit time factor.

Combining eqs. (2.29), (2.31), and (2.32) results in

$$\tilde{R}_{\text{sh}} = R_{\text{sh}} \mathcal{T}^2, \quad (2.35)$$

where the *shunt impedance* R_{sh} has been defined as

$$R_{\text{sh}} = \frac{\left(\int_{-d/2}^{d/2} dz E_z \right)^2}{P_{\text{diss}}}. \quad (2.36)$$

Here, R_{sh} is solely dependent on the cavity while \tilde{R}_{sh} is also dependent on the velocity of the particle because of \mathcal{T} . More often, the *characteristic shunt impedance* R_{sh}/Q_0 is used instead, because it is uniquely determined by the dimensions of the cavity, irrespective of ohmic loss on the walls [107]. In particular, it quantifies the coupling strength between the cavity and beam in terms of transferring energy. The characteristic shunt impedance is given, after substituting eq. (2.36) into eq. (2.22), as

$$\frac{R_{\text{sh}}}{Q_0} = \frac{\left(\int_{-d/2}^{d/2} dz E_z \right)^2}{\omega_0 W}. \quad (2.37)$$

2.4 Power Coupling

For the successful operation of a cavity, an RF coupler is indispensable for bonding the cavity with the surroundings [108]. The flow of the EM energy via the coupler is in general bidirectional, although the exact direction depends on the purpose that the cavity serves. The energy is to be fed into a cavity for the beam acceleration, but extracted from a cavity for the beam detection. In the following, much attention will be paid to the latter due to the objective of the position detection by a cavity.

2.4.1 Coupling Schemes

A coupler is the interface between a cavity and a transmission line, which can be either a coaxial cable (low frequency, little power) or a waveguide (high frequency, huge power). Based on the coupled field, it can be divided into electric, magnetic, and electromagnetic coupler [108], which are schematically shown in fig. 2.4.

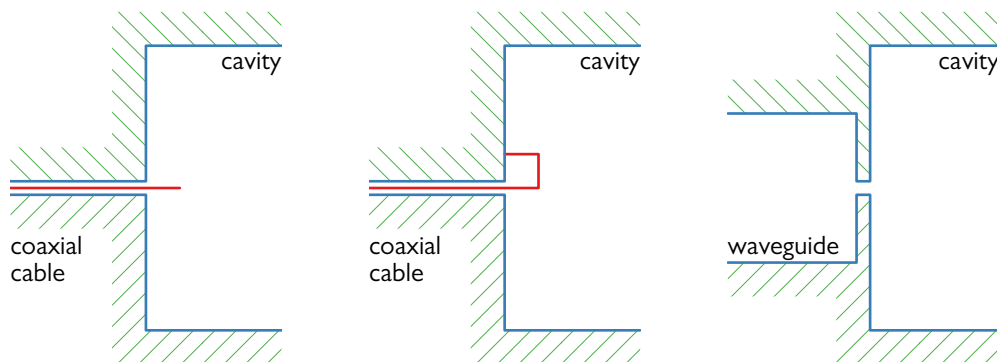


Figure 2.4 Schematics of electric (left), magnetic (middle), and electromagnetic (right) coupler.

An electric coupler is normally a probe extending into a cavity. It can be modeled as an electric dipole \mathbf{P} , of which the moment is determined by its length. The coupling strength is proportional to the scalar product $\mathbf{P} \cdot \mathbf{E}$, where \mathbf{E} is the electric field strength at the location of the coupler. In comparison, a magnetic coupler is a loop placed inside a cavity. It can be modeled as a magnetic dipole

\mathbf{M} , of which the moment is determined by its area. The coupling strength is proportional to the scalar product $\mathbf{M} \cdot \mathbf{H}$, where \mathbf{H} is the magnetic field strength at the location of the coupler. An electromagnetic coupler interacts with both EM fields. It is usually an aperture on the wall of a cavity and connected to a waveguide, through which the EM waves inside the cavity can propagate into the waveguide. The coupling strength has both electric and magnetic contribution.

In analogy with eq. (2.22), the coupled power P_{coup} from the cavity to a load can be described via the *external quality factor* Q_{ext} [108]:

$$Q_{\text{ext}} = \frac{\omega_0 W}{P_{\text{coup}}}. \quad (2.38)$$

The total power loss P_{tot} is thus related to the *loaded quality factor* Q_{load} :

$$Q_{\text{load}} = \frac{\omega_0 W}{P_{\text{tot}}} = \frac{\omega_0 W}{P_{\text{diss}} + P_{\text{coup}}}. \quad (2.39)$$

Substituting eqs. (2.22) and (2.38) into eq. (2.39) simply leads to

$$\frac{1}{Q_{\text{load}}} = \frac{1}{Q_0} + \frac{1}{Q_{\text{ext}}}. \quad (2.40)$$

Moreover, it is convenient to define a ratio, named *coupling coefficient* κ , to characterize the efficiency of the coupler in transferring the EM energy to the load:

$$\kappa = \frac{P_{\text{coup}}}{P_{\text{diss}}} = \frac{Q_0}{Q_{\text{ext}}}. \quad (2.41)$$

In particular when $\kappa = 1$, it is called *critical coupling*, where no incident EM waves are reflected at the coupler and the maximum power flows into the load. Other than that, *overcoupling* and *undercoupling* can be differentiated for $\kappa > 1$ and $\kappa < 1$, respectively [108].

The optimization of a coupler is an art in itself. To name a few, the length of a probe or the orientation of a loop can be adjusted to attain the critical coupling. When a cavity resonates in the monopole mode, a loop should be mounted on the curved wall for the intensity detection due to the dominant magnetic field on the edge. However, in the case of dipole mode, two symmetrically arranged loops on the curved wall or probes on a flat end should be adopted, such that the difference of these two signals rejects the parasitic monopole mode and hence improves the accuracy of the position detection [109].

2.4.2 Frequency Spectrum of Coupled Signal

When a cavity is employed as a beam diagnostic device, the coupled signal contains rich information about the beam dynamics, especially when the signal is analyzed in frequency domain. This is in particular beneficial for a circular accelerator, where a beam passes the cavity periodically, already suggesting some pattern in the frequency spectrum. In the case of a coasting beam, the charged particles spread over the whole ring and circulate independently. The incoherent signal coupled by a cavity is, after deducting the DC component, the Schottky noise of the beam, which allows for investigations on the individual particles, rather than treating the beam as a whole. The Schottky noise also exists for a bunched beam, although on an unfavorable stage in competition with a much stronger coherent signal. Being influenced by the periodic motion of all the bunches, the frequency spectrum also becomes complicated [110]. For the nuclear mass measurements with storage rings, the cocktail beams of exotic nuclei in the experiments are normally un-bunched. Therefore, the signal of a coasting beam will only be treated in the following.

Suppose a particle j with charge q is circulating in a storage ring at a frequency f_{rev} , and the depth of a detecting cavity is negligibly small (thin cavity approximation). As a result, the current \tilde{I}_j of the charged particle seen by the cavity is a train of delta functions [111]:

$$\tilde{I}_j(t) = q \sum_{n=-\infty}^{+\infty} \delta\left(t - t_j - \frac{n}{f_{\text{rev}}}\right), \quad (2.42)$$

where t_j is the time when the particle passes the cavity in its zeroth lap. The Fourier transform of the current I_j is given as

$$I_j(f) = \int_{-\infty}^{+\infty} dt \tilde{I}_j(t) e^{-i2\pi ft} \quad (2.43)$$

$$= qf_{\text{rev}} \sum_{n=-\infty}^{+\infty} \delta(f - nf_{\text{rev}}) e^{-in\vartheta_j}, \quad (2.44)$$

where $\vartheta_j = 2\pi f_{\text{rev}} t_j$, and the relation

$$\sum_{n=-\infty}^{+\infty} e^{-i2\pi n f / f_{\text{rev}}} = f_{\text{rev}} \sum_{n=-\infty}^{+\infty} \delta(f - nf_{\text{rev}}) \quad (2.45)$$

has been used. Equation (2.44) shows that, apart from a DC component ($n = 0$), the current of a charged particle comprises an infinite number of harmonics ($n = \pm 1, \pm 2, \dots$) at the frequencies evenly spaced by f_{rev} .

Now, let N particles of the same species occupy the whole ring while circulating at the same frequency. They are merely distinguished by the initial azimuthal positions $\{\vartheta_j\}$, which are randomly distributed in an interval of $[0, 2\pi)$. The total current I in frequency domain is the sum of eq. (2.44) over the index j :

$$I(f) = qf_{\text{rev}} \sum_{n=-\infty}^{+\infty} \delta(f - nf_{\text{rev}}) \sum_{j=1}^N e^{-in\vartheta_j}. \quad (2.46)$$

It is clear from eq. (2.46) to find that the ensemble average $\langle I \rangle$ contains only the DC component, which is the macroscopic beam current. On the contrary, the Schottky noise, defined as $I_{\text{Sch}} = I - \langle I \rangle$, is the microscopic fluctuation of the beam current.

It is intuitive to speculate that the *power spectral density* S of the Schottky noise is the quadratic of I_{Sch} . In fact, the exact relation is given as [111]

$$\langle I_{\text{Sch}}(f) I_{\text{Sch}}^*(f') \rangle = S(f) \delta(f - f'). \quad (2.47)$$

By virtue of eq. (2.46), the left hand side of eq. (2.47) can be expanded to

$$\langle I_{\text{Sch}}(f) I_{\text{Sch}}^*(f') \rangle = q^2 f_{\text{rev}}^2 \sum_{n, m \neq 0} \delta(f - nf_{\text{rev}}) \delta(f' - mf_{\text{rev}}) \sum_{j, k=1}^N \langle e^{-i(n\vartheta_j - m\vartheta_k)} \rangle \quad (2.48)$$

$$= Nq^2 f_{\text{rev}}^2 \delta(f - f') \sum_{n \neq 0} \delta(f - nf_{\text{rev}}), \quad (2.49)$$

where the expectation $\langle e^{-i(n\vartheta_j - m\vartheta_k)} \rangle$ is nonzero only if $n = m$ and $j = k$. Equating eqs. (2.47) and (2.49) immediately leads to

$$S(f) = Nq^2 f_{\text{rev}}^2 \sum_{n \neq 0} \delta(f - nf_{\text{rev}}) \quad (2.50)$$

$$= 2Nq^2 f_{\text{rev}}^2 \sum_{n=1}^{+\infty} \delta(f - nf_{\text{rev}}). \quad (2.51)$$

The factor of two in eq. (2.51) is based on the fact that the negative frequency is just a mathematical construct for aiding analysis, and should be superposed to the opposite frequency when interpreting the result in the physical world.

According to eq. (2.51), the power spectral density of the Schottky noise is proportional to the particle number. Each particle contributes the same amount of $2q^2\bar{f}_{\text{rev}}^2\delta(f - nf_{\text{rev}})$ to the n th harmonic. In reality, the revolution frequencies of different particles certainly manifest deviations spreading around a mean value \bar{f}_{rev} . Let Φ be the normalized (to unity) distribution of the particles in the revolution frequency. Equation (2.51) should be modified to

$$S(f) = \int_{\tilde{f}_{\text{rev}}}^{\hat{f}_{\text{rev}}} df_{\text{rev}} N\Phi(f_{\text{rev}}) 2q^2\bar{f}_{\text{rev}}^2 \sum_{n=1}^{+\infty} \delta(f - nf_{\text{rev}}) \quad (2.52)$$

$$= 2Nq^2\bar{f}_{\text{rev}}^2 \sum_{n=1}^{+\infty} \int_{\tilde{f}_{\text{rev}}}^{\hat{f}_{\text{rev}}} df_{\text{rev}} \Phi(f_{\text{rev}}) \frac{1}{n} \delta\left(f_{\text{rev}} - \frac{f}{n}\right) \quad (2.53)$$

$$= 2Nq^2\bar{f}_{\text{rev}}^2 \sum_{n=1}^{+\infty} \frac{1}{n} \Phi\left(\frac{f}{n}\right), \quad (2.54)$$

where \tilde{f}_{rev} and \hat{f}_{rev} define the bounds of the revolution frequency spread.

A message conveyed in eq. (2.54) is that, after taking the frequency spread into account, the spectral line at every harmonic is smeared out into a wide Schottky band. Because Φ is defined as a function of the revolution frequency, $f = nf_{\text{rev}}$ must hold at the n th harmonic, which means that the band width Δf and the centroid frequency f_c scale linearly with n . Thus, the relative spread of the revolution frequency can be calculated via $\Delta f/f_c$ at any harmonic. Moreover, the power spectral density at the n th harmonic S_n can be extracted from eq. (2.54), and given as

$$S_n(nf_{\text{rev}}) = \frac{2Nq^2\bar{f}_{\text{rev}}^2 \Phi(f_{\text{rev}})}{n}. \quad (2.55)$$

It is clear in eq. (2.55) that the band height is inversely proportional to n , but the band power—the integral of S_n over the entire band—remains the same. Figure 2.5 illustrates the Schottky bands of a coasting beam with an exaggerated revolution frequency spread. Each band carries the identical information about the beam. As a rule of thumb, to handle the Schottky noise at a higher harmonic is always preferable, provided that the Schottky bands are not overlapped and still distinct from other kinds of noises [112].

If the detecting cavity is exactly tuned into the n th harmonic ($\omega_0 = 2\pi n\bar{f}_{\text{rev}}$), it can be modeled with an intrinsic resistor R_{sh} and a transformer-bridged resistor R_1 , where the transformer models the coupler. These two elements are connected in parallel to an ideal current source I_n , which models the beam [104]. Based on eq. (2.41), the coupling coefficient κ quantitatively relates R_{sh} and R_1 :

$$\kappa = \frac{P_{\text{coup}}}{P_{\text{diss}}} = \frac{R_{\text{sh}}}{R_1}. \quad (2.56)$$

Using eqs. (2.40), (2.41), and (2.56), after some basic circuit analyses, the power flowing into the load is given as

$$P_{\text{coup}} = I_n^2 R_{\text{sh}} \frac{Q_{\text{load}}^2}{Q_0 Q_{\text{ext}}}, \quad (2.57)$$

where I_n^2 is recognized as S_n in eq. (2.55). Therefore, eq. (2.57) can be finalized to

$$P_{\text{coup}} = \frac{2Nq^2\bar{f}_{\text{rev}}^2 \Phi}{n} \frac{Q_{\text{load}}^2}{Q_0 Q_{\text{ext}}} R_{\text{sh}}. \quad (2.58)$$

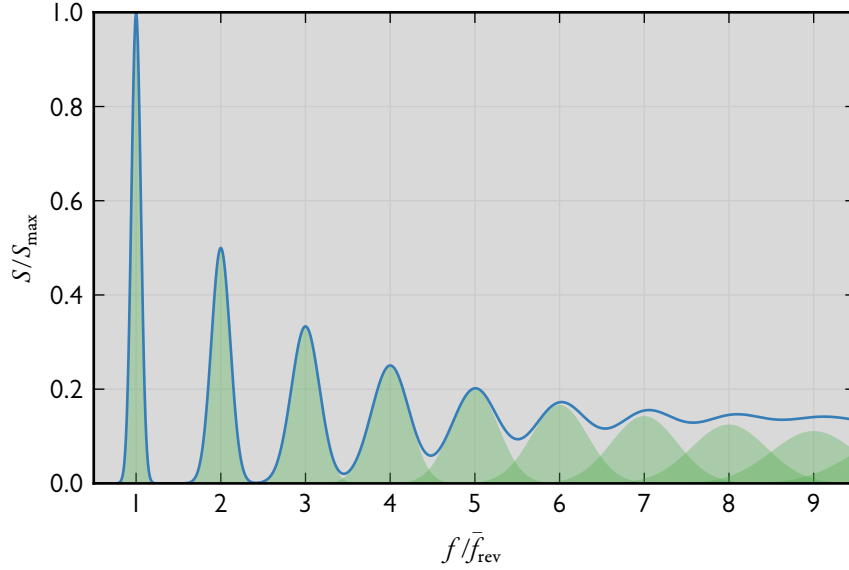


Figure 2.5 Schematic plot of the power spectral density of the Schottky noise of a coasting beam in a storage ring. The green areas centering at every multiple of the mean revolution frequency represent the Schottky bands at different harmonics. The blue curve is the superposition of all the bands. In the plot, the Schottky bands starts to overlap at the fourth harmonic. From the eighth harmonic, the overlapping is so dramatic that the total Schottky noise becomes a plateau. Note that the frequency spread is intentionally exaggerated for a better presentation.

It is worth noting that eq. (2.58) is rooted in the thin cavity approximation. Revoking this approximation mainly results in two consequences: The transit time factor needs to be incorporated such that R_{sh} in eq. (2.58) should be replaced with \tilde{R}_{sh} , and the signal starts to roll off at a frequency of the order of $1/t_{\text{tr}}$, where t_{tr} is the transit time [110]. Also, attention should be paid to the position dependence of the shunt impedance (cf. fig. 2.1). This feature can be exploited to distinguish the revolution orbits of the particles by comparing the signal power. However, as a side effect, the betatron motion of the beam will additionally contribute transverse side bands to the Schottky spectrum [110]. Fortunately, thanks to the low intensity of the cocktail beams in the typical mass measurement experiments, this problem is not a critical concern.

2.5 Correction for Anisochronism Effect

By revisiting eq. (1.2), it is found that the mass-to-charge ratio of an ion is determined by its magnetic rigidity and velocity. The velocity is the product of the orbital length and revolution frequency, where the former is again determined by the magnetic rigidity. In all, m/q is a function of two independent variables, namely $B\rho$ and f_{rev} . By using an intensity cavity of which the shunt impedance barely varies with the horizontal position, only the mean revolution frequency can be attained for each kind of nuclei. It is obviously insufficient to evaluate the nuclear masses without the information about the magnetic rigidities. Consequently, the results are not robustly accurate, and the uncertainties are thus overestimated.

This issue can be overcome by introducing a position cavity adjacent to the intensity cavity [113]. This cavity doublet is then able to measure $B\rho$ along with f_{rev} , given that the momentum dispersion is sufficiently large at the location of the cavity doublet. By fixing the magnetic rigidity and determining the corresponding revolution frequency for each kind of nuclei, the mass-to-charge ratios are solely dependent on the determined revolution frequencies. From there on, the Correlation Matrix Method

can readily be used to evaluate the nuclear masses [114, 115]. It is important to note that this detection scheme with a cavity doublet is intrinsically free of the anisochronism effect, provided that the ion optics of the ring is isochronously optimized. Therefore, the results can significantly be improved in both accuracy and precision.

Having outlined the analysis procedure, it is time to supplement the missing route from a fixed magnetic rigidity to the corresponding revolution frequency. Essentially, it is the correspondence between the revolution frequency and horizontal position that needs to be pursued. Let \parallel and \perp denote the intensity cavity and the position cavity, respectively. Both cavities have been tuned to the same resonant frequency. According to eq. (2.58), the ratio of the coupled power from two cavities is independent of the beam attributes:

$$\left(\frac{P_{\perp}}{P_{\parallel}}\right)_{\text{coup}} = K \left(\frac{R_{\perp}}{R_{\parallel}}\right)_{\text{sh}}, \quad (2.59)$$

where a constant K wraps all the ratios of the quality factors:

$$K = \left(\frac{Q_{\perp}}{Q_{\parallel}}\right)_{\text{load}}^2 \left(\frac{Q_{\parallel}}{Q_{\perp}}\right)_0 \left(\frac{Q_{\parallel}}{Q_{\perp}}\right)_{\text{ext}}. \quad (2.60)$$

The left hand side of eq. (2.59) is a function of the revolution frequency f_{rev} , in contrast to the horizontal position x for the right hand side:

$$\left(\frac{P_{\perp}}{P_{\parallel}}\right)_{\text{coup}} = \mathcal{P}(f_{\text{rev}}), \quad (2.61)$$

$$\left(\frac{R_{\perp}}{R_{\parallel}}\right)_{\text{sh}} = \mathcal{R}(x). \quad (2.62)$$

Eventually, the correspondence between f_{rev} and x is obtained by substituting eqs. (2.61) and (2.62) into eq. (2.59):

$$f_{\text{rev}} = \mathcal{P}^{-1}[K\mathcal{R}(x)] \equiv \mathcal{G}(x), \quad (2.63)$$

where \mathcal{P} is presumed to be invertible, and \mathcal{P}^{-1} denotes its inverse. A counterexample would be the case of the isochronous ions, where f_{rev} is independent of x , or at least the frequency spread is comparable to the frequency resolution of the detection system. Although the present method with a cavity doublet cannot be applied to this very case, it is sufficiently accurate to work with the mean revolution frequency extracted from the Schottky spectrum of the intensity cavity.

Having obtained the *gauge function* \mathcal{G} for each kind of nuclei, it is then straightforward to compute the *representative revolution frequency* f_{rep} by substituting for the horizontal position with an arbitrary value x_{rep} . Once x_{rep} is chosen, it has to remain constant throughout the entire process. However, in practice, functions \mathcal{P} and \mathcal{R} are only experimentally known at a set of discrete points, rather than in a continuous interval. For instance, \mathcal{P} is obtained from the Schottky spectra of both cavities at the frequencies that are evenly spaced by the resolution, while \mathcal{R} is obtained from the benchtop measurements at the sample positions. In order to attain the gauge function, the parametric regression, usually by a polynomial, of the discrete points is a prerequisite for both \mathcal{P}^{-1} and \mathcal{R} . Note that in eq. (2.63), \mathcal{P}^{-1} is directly involved in \mathcal{G} , so f_{rev} should be the dependent variable while $(P_{\perp}/P_{\parallel})_{\text{coup}}$ should be the independent variable for the regression.

The regression uncertainty is dependent on the sample size. More discrete points will lead to a better regression accuracy. The sample size can be augmented by, for instance, improving the frequency resolution in the Schottky spectrum. This is equivalent to the prolongation of the frame length for the Fourier transformation. However, the frequency uncertainty may increase as well due to the instability of the power supplies for the magnets. A judicious compromise of the frequency resolution thus needs

to be found. Alternatively, a long frame of data can be split into several small parts, to which the Fourier transformation is applied separately. The averaged spectrum of them will render a better signal-to-noise ratio. In addition, an average can even be applied among different storage cycles to accumulate statistics, which is beneficial for the rare nuclei with low yields.

3 CONCEPTUAL DESIGN



The design of a position-resolving cavity is essentially a task of optimizing its geometry so as to maximize the gradient of the shunt impedance in a transverse direction, while still complying with realistic constraints in different aspects (e.g. beam dynamics, aperture size). Needless to say, the quantification of the EM fields inside the cavity plays a central role throughout the entire design stage. Yet they can analytically be carried out for only a few simple structures, a numerical approach by means of the Finite Element Method (FEM) provides a more general solution in case the structure becomes complex. Before diving into the iterations of the design right away, it is instructive to take a retrospective look at successful implementations of the RF cavity for the beam position detection.

3.1 Historical Perspective

The concept of integrating a cavity into the beam position detection to enhance the signal-to-noise ratio was originally proposed by R. Bergere *et al.* in 1962 [116]. Figure 3.1 illustrates a symmetric configuration of four identical cavities in their design for an electron linac in Saclay. It was in fact

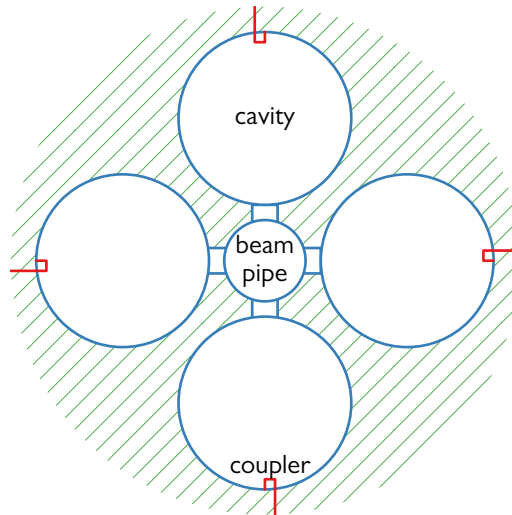


Figure 3.1 Schematic view of a Beam Position Monitor (BPM) with four identical cavities proposed by R. Bergere *et al.*. The cavities are connected to the beam pipe via slots. The beam-induced EM fields are enhanced by the cavities, and then picked up by loop couplers. (Adapted from [116].)

an improvement of a button Beam Position Monitor (BPM) by replacing the coupling buttons with

cavities. The electron-radiated magnetic field propagated via slots and resonated in cavities at 3 GHz. Then, four coupling loops on the edge picked up the field in these cavities.

To detect the beam position by using an RF cavity in its true sense was explored by P. Brunet *et al.* [117], and first realized at Stanford Linear Accelerator Center (SLAC) [118]. The detection system comprised two orthogonally placed rectangular position cavities resonating in the dipole mode, through which electron beams passed directly. In addition, a circular intensity cavity operating in the monopole mode was installed nearby to offer the phase reference for the other two. The magnitude of a phase-calibrated signal of any position cavity implied the amount of a corresponding beam displacement, while the polarity indicated the direction. So if there was no signal, the beam was in the center. Following the pioneering work at SLAC, a handful of rectangular cavities have come into operation for the beam position detection in various accelerator facilities [119–121]. The main advantage of the rectangular shape is the ability to well separate the signals for the horizontal and vertical displacement in frequency domain. This can be obtained by deviating the length and width of a cavity to a considerable degree (fig. 3.2).

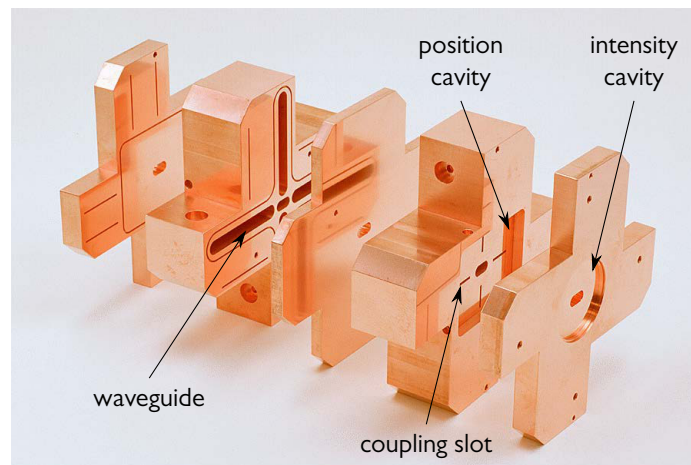


Figure 3.2 Photo of a Beam Position Monitor (BPM) block developed at KEK. The height of the rectangular position cavity is 6 mm, while the width is 12 mm. The signals for the horizontal and vertical displacement are selectively coupled by the orthogonal waveguides via the coupling slots. The resonant frequency is 5.7 GHz for the horizontal direction, and 6.4 GHz for the vertical direction. The circular intensity cavity serves as a reference. (Adopted from [120].)

Being a cousin of the rectangular cavity, a circular counterpart has been adopted much more widely at different laboratories around the world, due to its geometric simplicity for manufacture. Since the debut at Chalk River Laboratories (CRL) in 1979 [122], the circular position cavities have been deployed or designed for the beam diagnostics in Free-Electron Laser (FEL) facilities [123–125], electron positron colliders [126–129], and fixed target accelerators [130, 131]. Due to the rotational symmetry of the circular cavity, there are actually two dipole modes degenerating in frequency with mutually orthogonal field orientations. Consequently, the interference between the two signals for the horizontal and vertical displacement, termed as crosstalk, may become evident for a high-intensity beam. It is therefore quite standard to plug in four identical waveguides, which are evenly spaced by 90° in the azimuthal direction around the cavity, to selectively couple out specific dipole fields and meanwhile reject the monopole contamination. Although most of the circular position cavities are operated in companion with electron beams, only one special design aims at the position detection for heavy ions. Figure 3.3 illustrates the cavity BPM for the CR at FAIR presented by M. Hansli *et al.* [132]. The highlight of this design is the ability to self-calibrate the position signal with the reference signal picked up by a coupling loop in the neutral plane of the dipole mode.

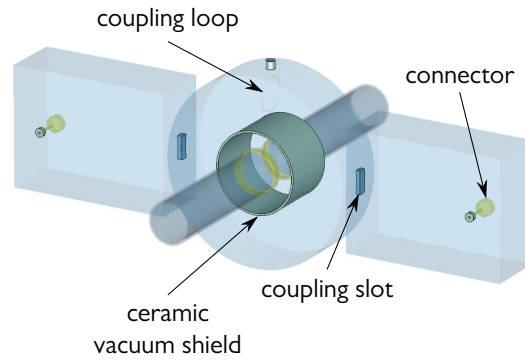


Figure 3.3 Circular Beam Position Monitor (BPM) designed for the CR at FAIR. The dipole mode is coupled out by two opposite waveguides, while the monopole mode is picked up by a loop in the middle. The ceramic shield isolates the cavity from the ultra-high vacuum inside the beam pipe. (Adopted from [132].)

In order to improve the position resolution and intensity sensitivity of a circular cavity, two kinds of modifications can be applied to the cavity geometry. In the left panel of fig. 3.4, the vicinity of the beam pipe is pushed inwards, forming nose cones on both sides of the cavity. It can be shown

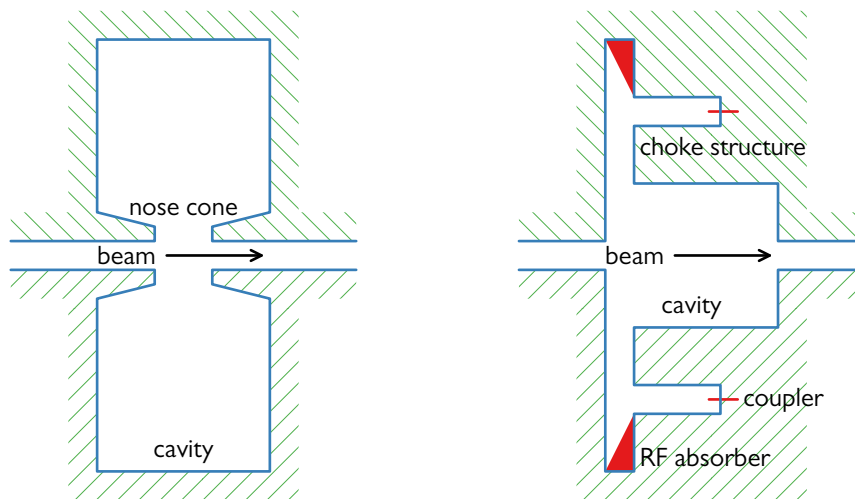


Figure 3.4 Two commonly used modifications to a circular cavity to improve the position resolution and intensity sensitivity. Shown on the left hand side is a so-called re-entrant cavity, where nose cones are formed around the beam pipe on both sides of the cavity. Shown on the right hand side is a so-called choke mode cavity proposed by T. Shintake. The choke structure is an extruded ring coaxial with the beam pipe to pick up the desirable mode. The other modes will be damped by an RF absorber filled on the edge. (Right panel adapted from [133].)

that this deformation significantly concentrates the electric field in the pipe region, thus increases the shunt impedance [134]. The utilization of such a shape has already been implemented worldwide in several designs [135–137]. The right panel of fig. 3.4 sketches a so-called choke mode cavity that was proposed by T. Shintake [133]. It was supposed to trap the desirable mode by a choke structure with a radius of quarter wavelength of that mode, and damp parasitic modes with an RF absorber filled on the

edge. This special arrangement can effectively purify the dipole field in the case of the beam position detection, and eventually lead to a good signal-to-noise ratio.

A common feature shared by the aforementioned designs is that all the cavities resonate in the dipole mode to detect the displacements of bunched beams. Since the electric field in the dipole mode is antisymmetric about the central plane, the shunt impedance is very little near the center. Fortunately, a bunched beam induces a coherent signal inside the cavity, which scales with the square of the particle number and thus compensates the weakness of the coupling strength [110].

However, for a coasting beam in a typical mass measurement experiment, the Schottky signal scales linearly with the particle number. The low intensity of the beam (a few ions for the nuclei of interest) imposes an even greater challenge on the position detection in the dipole mode. To circumvent these limitations, it is proposed to exploit the monopole mode of a cavity and offset the beam pipe to one side [138]. This kind of design can deliver a higher shunt impedance, while still enjoying a large electric field gradient in a half of the cavity. In order to minimize the crosstalk between two transverse directions, it is suggested to stretch the cavity in one direction such that the gradient of the shunt impedance lies mostly in the other direction within the aperture region.

3.2 Design Criteria

Although the conception of a novel position cavity has been established, further developments into a functional design necessitate realistic parameters from a specific storage ring. In fact, the cavity is planned for the deployment in the Collector Ring (CR) at FAIR in Darmstadt, in order to attend to the experimental duties assigned by the Isomeric beams, Lifetimes and MAsses (ILIMA) collaboration [139].

3.2.1 Isochronous Modes of Collector Ring

The CR is the first storage ring cascaded downstream a synchrotron (SIS100) and a fragment separator (Super-FRS). It has a circumference of 221.45 m and a maximum magnetic rigidity of 13 T·m. In order to effectively accept hot radioactive ion beams and, possibly, antiprotons, the CR will be equipped with vacuum chambers in an excessive size (41 cm by 20 cm inside the dipole magnets). The main objective of the CR is to rapidly cool the injected beams by means of the stochastic cooling. The cooled beams will then be transferred to the subsequent rings for physical experiments.

Additionally, the CR can be operated as an isochronous mass spectrometer once the ion optics is tuned isochronously [140]. In order to be able to store a broader nuclide region towards the neutron and proton drip-line, the CR will incorporate three isochronous ion-optical settings with transition energies of 1.43, 1.67, and 1.84 (fig. 3.5). The comparison among these isochronous modes is presented in table 3.1.

Table 3.1 Machine parameters of the CR in three isochronous modes. The kinematic quantities are calculated for the isochronous ions.

Isochronous mode	I	II	III
Transition energy	1.43	1.67	1.84
Velocity [c]	0.715	0.801	0.839
Revolution frequency [MHz]	0.968	1.084	1.136
Kinetic energy [MeV·u ⁻¹]	400	625	790
Transverse acceptance [mm·mrad]	100	100	100
Momentum acceptance [%]	±0.22	±0.46	±0.62

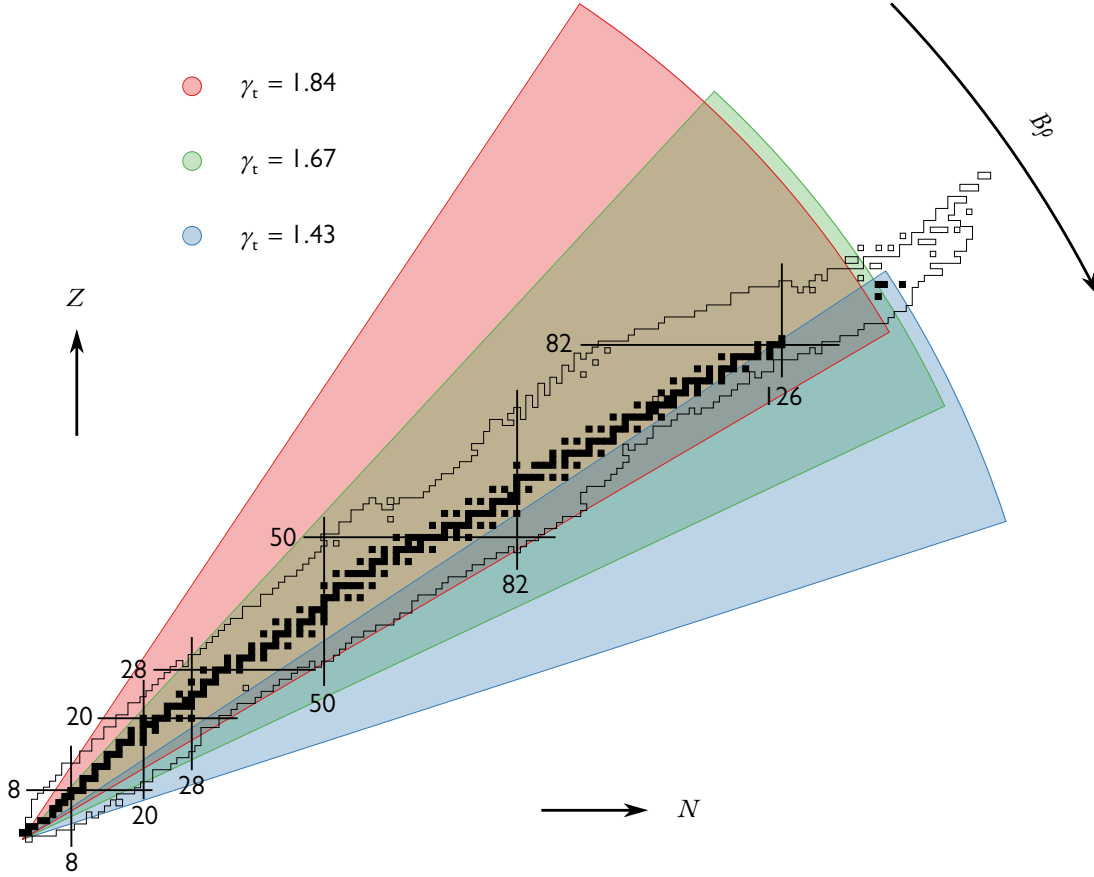


Figure 3.5 Chart of the nuclides featuring the theoretical storage capability of the CR. The black borderline sketches the nuclide region with known masses. The colored sectors schematically indicate the nuclide regions that can be stored in the CR in the isochronous modes with three ion-optical settings. The magnetic rigidity $B\rho$ ranges from 8 T·m to 13 T·m for each transition energy γ_t . (Adapted from [140].)

3.2.2 Requirement Specifications

The experiment programs proposed by the ILIMA aim at precision measurements of the fundamental properties, such as masses and lifetimes, of exotic nuclei near or on the nucleon drip-lines in their ground and isomeric states. Due to the low yields of those nuclei, single-particle sensitivity is required for the position cavity. Moreover, the cavity should enable a good mass resolving power of the order of 10^6 within a short time of 20 ms [141].

The coupled signal from the cavity will be processed in frequency domain. Each frequency spectrum is obtained by gathering a sufficient number (e.g. 1024) of signal samples to apply the Fourier transformation, which leads to a certain latency. A low latency can be attained at a cost of a coarse frequency resolution, due to the reciprocal relation between them. Therefore, the required frequency resolution δf is given as

$$\delta f = \frac{1}{20 \text{ ms}} = 50 \text{ Hz.} \quad (3.1)$$

Note that a factor of two is not directly involved in the calculation though, the result is credible in accord with the Nyquist-Shannon sampling theorem, which states that when digitizing an analog signal, a sampling rate of twice the maximum frequency of the original signal is sufficient to retain its fidelity [142, 143]. This is because in practice, usually two independent Analog-to-Digital Converters (ADCs) with a phase difference of $\pi/2$ digitize the coupled signal synchronously to preserve the full

information of the amplitude and phase [144]. The effective sampling rate is thus doubled.

A coarse frequency resolution can be compensated by selecting a Schottky band at a higher harmonic so as to achieve the required mass resolving power. According to eq. (1.1), by neglecting the second term on the right hand side, the preferable resonant frequency of the cavity f_0 is given as

$$f_0 = \frac{\gamma_{\tau}^2 m \delta f}{\delta m} = 1.84^2 \times 10^6 \times 50 \text{ Hz} = 169.28 \text{ MHz}. \quad (3.2)$$

The transition energy of the third isochronous mode in table 3.1 is taken for the calculation, since it represents the least favorable scenario. Any resonant frequency higher than 169.28 MHz will deliver a better mass resolving power than 10^6 for all the three modes.

On the other hand, a large shunt impedance is a prerequisite for the single-particle sensitivity. To assess the required value, first consider a single ion with a moderate charge state of 60 in the CR. The Schottky signal power P_{Sch} of the ion detected by the cavity can be obtained by integrating the distribution function Φ in eq. (2.58), which gives rise to

$$P_{\text{Sch}} = (qf_{\text{rev}})^2 \left(\frac{R_{\text{sh}}}{Q_0} \right) Q_{\text{load}}, \quad (3.3)$$

where a critical coupling is assumed. Next consider the thermal effect as the only contribution to the noise, of which the power P_{th} amounts to [145, 146]

$$P_{\text{th}} = 4k_{\text{B}} T \delta f, \quad (3.4)$$

where k_{B} is the Boltzmann's constant and T is the absolute temperature of the detection system. The ion optics of the CR is assumed to be stable during 20 ms, such that the bandwidth of the ion is limited to the frequency resolution δf . The signal-to-noise ratio is conservatively estimated to be four-to-one for the ion on the central orbit. By virtue of eqs. (3.3) and (3.4), this ratio leads to

$$\frac{R_{\text{sh}}}{Q_0} = \frac{4k_{\text{B}} T \delta f P_{\text{Sch}}}{Q_{\text{load}} (qf_{\text{rev}})^2 P_{\text{th}}} = 37.7 \Omega, \quad (3.5)$$

where T is taken as a room temperature of 295 K and Q_{load} is moderately assumed to be 10^3 . The revolution frequency in the first isochronous mode in table 3.1 is taken for the calculation, again because it represents the least favorable scenario.

To summarize, all the design specifications of the position cavity are prescribed in table 3.2.

Table 3.2 Design specifications of the position-resolving cavity in accordance with the requirements assigned by the ILIMA collaboration. The characteristic shunt impedance is for the central orbit.

Item	Value	Unit
Width of aperture	41	cm
Height of aperture	20	cm
Resonant frequency	169.28	MHz
Time resolution	20	ms
Frequency resolution	50	Hz
Charac. shunt impedance (middle)	37.7	Ω

3.3 Analytic Sketch

The base geometry of the position cavity is selected to be a rectangular prism or an elliptic cylinder. These kinds of shapes are simple, robust, and easy to manufacture. Most importantly, the RF properties can precisely be understood by analytic means. Since no preferences on any shape is evident at the moment, they will be equally treated and regularly compared throughout the design process.

3.3.1 Rectangular Cavity

A plain, fully closed rectangular cavity with height a , width b , and depth d is illustrated in fig. 3.6, along with an associated Cartesian coordinate system, of which the origin is located in the center and the z -axis points to the beam passage direction.

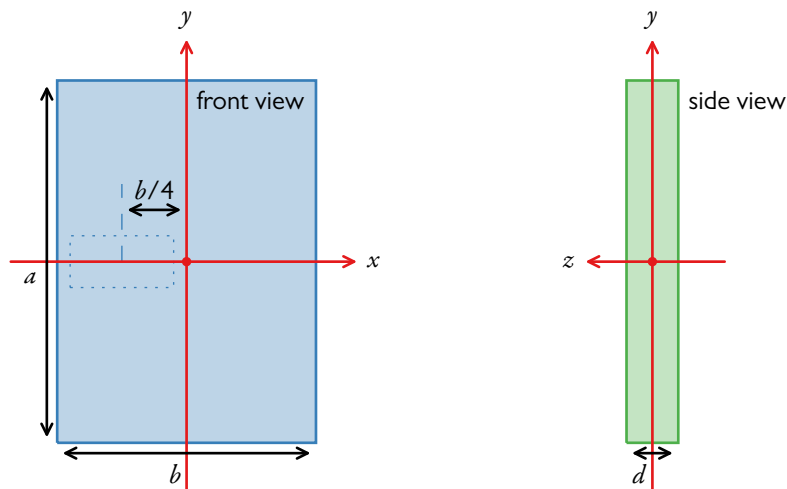


Figure 3.6 Schematic views of a rectangular cavity. The origin of the Cartesian coordinates is in the center of the cavity. The x -, y -, and z -axes lie in the horizontal, vertical, and longitudinal directions, respectively. The orientation of the coordinates follows the convention in the accelerator community. The location of the aperture is indicated with a dotted rectangle in the front view.

The mathematical expressions of the EM fields inside the cavity can be obtained by solving Maxwell's equations, and essentially, after the separation of the temporal and spatial part, by solving the Helmholtz equations in the Cartesian coordinate system:

$$\nabla^2 \mathbf{E} + \left(\frac{\omega_0}{c}\right)^2 \mathbf{E} = 0, \quad (3.6)$$

$$\nabla^2 \mathbf{H} + \left(\frac{\omega_0}{c}\right)^2 \mathbf{H} = 0, \quad (3.7)$$

where c is the speed of light in free space, \mathbf{E} and \mathbf{H} are the spatial parts of the electric and the magnetic field strength, respectively.

While a more general solution of the EM fields is documented in appendix A.1, a particular one of the electric field in the monopole mode is transcribed as follows:

$$E_x = 0, \quad (3.8)$$

$$E_y = 0, \quad (3.9)$$

$$E_z = E_0 \cos\left(\frac{\pi x}{b}\right) \cos\left(\frac{\pi y}{a}\right), \quad (3.10)$$

where E_0 is a scaling factor. Note that eq. (3.10) slightly differs from eq. (A.35), because the origin of the coordinate system has been translated from a vertex of the cavity to the center. The resonant frequency f_0 is determined by the dimensions via

$$f_0 = \frac{c}{2} \sqrt{\frac{1}{a^2} + \frac{1}{b^2}}. \quad (3.11)$$

With the quantitative distribution of the electric field obtained, it is now feasible to calculate the characteristic shunt impedance of the cavity. Substituting eqs. (3.10) and (3.11) into eq. (2.37), and using eq. (2.17) eventually result in

$$\frac{R_{\text{sh}}}{Q_0} = \frac{8\mu_0 cd}{\pi\sqrt{a^2 + b^2}} \cos^2\left(\frac{\pi x}{b}\right) \cos^2\left(\frac{\pi y}{a}\right). \quad (3.12)$$

It is clear in eq. (3.12) that the characteristic shunt impedance is also determined by the dimensions of the cavity, but independent of the field strength or the total energy. Second, it varies with transverse coordinates x and y : It peaks in the center where $x = y = 0$, then gradually decreases as x and y slide towards the lateral, and finally vanishes at the boundary where $x = \pm b/2$ or $y = \pm a/2$. Because of this feature, an aperture can be machined, for instance, on the left side of the cavity to allow for the beam passage. The exact location is indicated with a dotted rectangle in the front view of the cavity in fig. 3.6. Within the aperture region, the shunt impedance monotonically increases from left to right.

Ideally, the gradient of the shunt impedance ought to align with the x -axis in that region to eliminate the x - y crosstalk. In other words, the contours of the *shunt impedance map* should be straight and perpendicular to the horizontal direction. However, from eq. (3.12), a certain deviation from the ideal case is inevitable. This is in particular prominent near the center of the cavity, i.e. at the right end of the aperture. A quantity named *skewness* is introduced to characterize to which extent, in reality, the contour deviates from a straight line. It is defined as the horizontal span of the rightmost contour that connects the upper-right and lower-right vertex of the aperture. To rephrase it in mathematical language, let $(-x_v, y_v)$ be the upper-right vertex. Due to the mirror symmetry, $(-x_v, -y_v)$ must be the lower-right vertex. Suppose that the rightmost contour intersects the axis of symmetry at $(-x_i, 0)$, then the skewness s is given as $s = x_i - x_v$. Note that all the variables are positive, since the minus sign is explicitly written.

Recalling the aperture size in table 3.2, the intercept can be calculated by equating the shunt impedances at those two points:

$$\frac{R_{\text{sh}}}{Q_0} \left(20.5 - \frac{b}{4}, 10\right) = \frac{R_{\text{sh}}}{Q_0} (-x_i, 0), \quad (3.13)$$

which results in a skewness of

$$s = \frac{b}{\pi} \arccos \left[\cos \left(\frac{20.5\pi}{b} - \frac{\pi}{4} \right) \cos \left(\frac{10\pi}{a} \right) \right] - \frac{b}{4} + 20.5, \quad (3.14)$$

where all the variables are in a unit of centimeter.

The skewness can be reduced by increasing the aspect ratio a/b , i.e. by stretching the height and/or squeezing the width. It is obvious that the width of the cavity should at least be twice as much as that of the aperture. There is also a certain limit for the stretch of the height due to practical constraints, such as the available space to accommodate the cavity, and the ultra-high vacuum requirement in the CR. Besides, the expansion of the cavity will reduce the resonant frequency, to which a lower bound has been assigned in table 3.2. In all, the optimization of the design is to seek an adequate compromise after taking these factors into account.

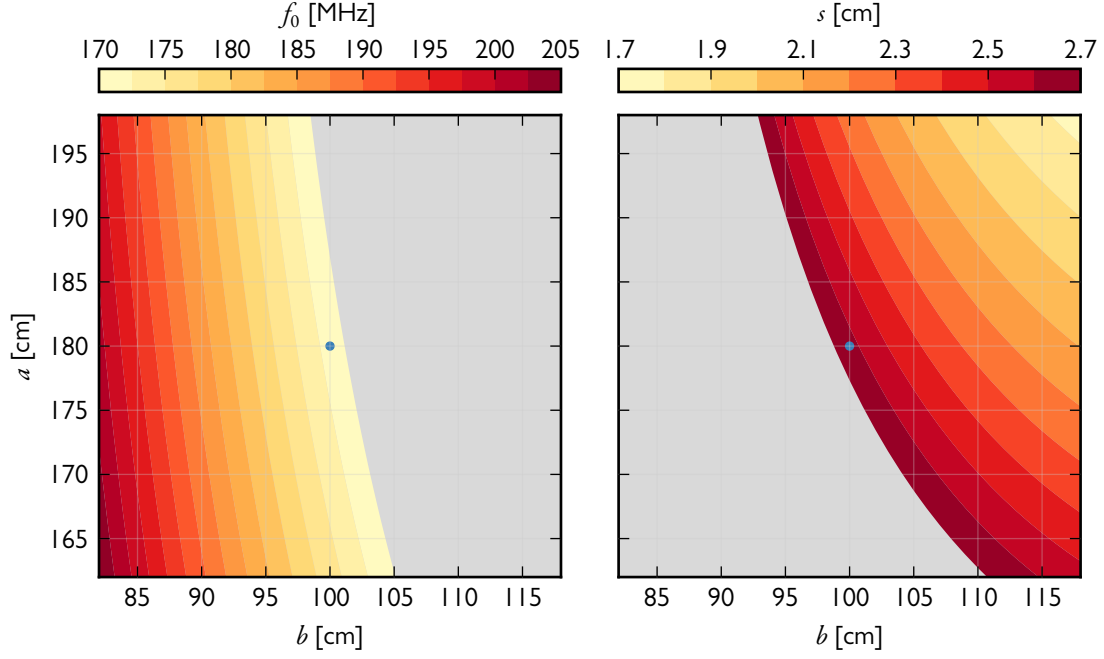


Figure 3.7 Dependence graph for the design of a rectangular position cavity. Shown on the left hand side is the dependence of the resonant frequency on the transverse dimensions of the cavity. The design specifications favor a higher resonant frequency. Shown on the right hand side is the dependence of the skewness on the transverse dimensions. A lower skewness is favored for the design. For both subgraphs, the infeasible regions are colored in gray. The optimum point is marked with a blue dot.

The *dependence graph* of f_0 and s on (a, b) can visually assist in selecting the optimum value. Figure 3.7 shows such a graph, where the color-coded resonant frequency and skewness are presented in the left and right panel, respectively. Except for the gray areas which mean infeasible for both subgraphs, the combination (a, b) favors dark red for the f_0 -subgraph, but light yellow for the s -subgraph. The optimum $(a, b) = (180, 100)$ is finally selected in the overlapped region of two feasible areas.

Consequently, the resonant frequency is determined to be 171.48 MHz, and the skewness is 2.63 cm. According to eq. (3.12), R_{sh}/Q_0 now solely depends on d . Therefore, the requirement of the shunt impedance in table 3.2 can be translated onto the depth of the cavity. By substituting $(x, y) = (-b/4, 0)$ into eq. (3.12), it is found that d should be greater than 16.18 cm. An even larger depth can lead to a higher characteristic shunt impedance, but also a lower transit time factor. Therefore, the effective shunt impedance may not increase accordingly. A depth of 16 cm is eventually decided on. As can be seen from fig. 3.8, the transit time factors are very close to unity for all the transition energies.

By virtue of eq. (3.12), the shunt impedance map within the aperture is drawn in fig. 3.9. Although the contour is more curved at the right end of the aperture, this may not be a critical issue because most ions are expected to pass through in the middle, where the contours are quite straight. Due to the same reason, the low magnitude of the shunt impedance at the left end can only weaken the signal to a limited extent. For the sake of convenience, the key parameters of the rectangular cavity are listed in table 3.3.

3.3.2 Elliptic Cavity

An elliptic cavity with height a , width b , and depth d is illustrated in fig. 3.10, together with an associated Cartesian coordinate system. The origin of the coordinates is located in the center, while

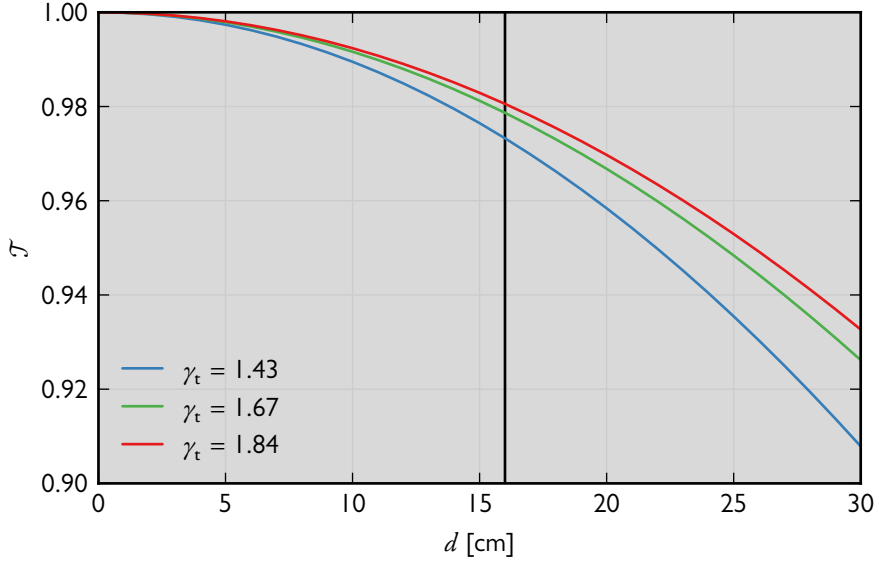


Figure 3.8 Transit time factors as a function of the depth of the rectangular cavity for the three transition energies. The vertical line at 16 cm indicates the selected value.

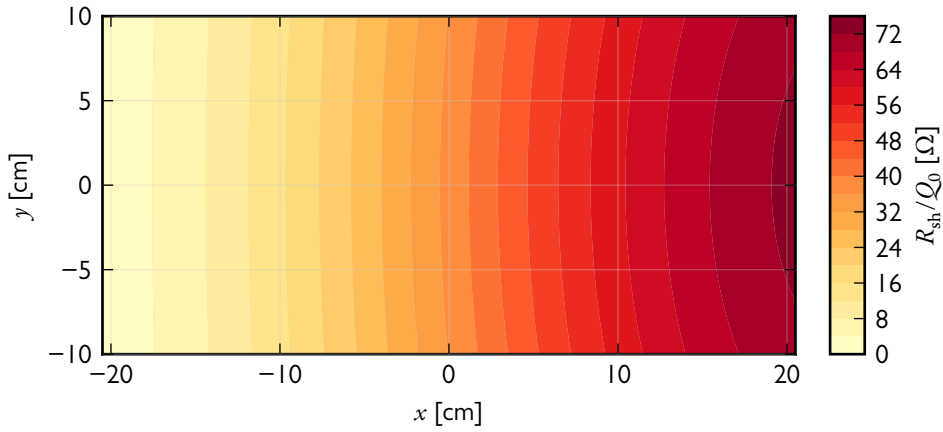


Figure 3.9 Shunt impedance map of the rectangular cavity in the aperture region. Note that the coordinates are based on a new Cartesian system, of which the origin has been translated to the center of the aperture.

the z -axis lies in the beam passage direction. To analytically solve the EM fields inside the cavity, it is convenient to expand eqs. (3.6) and (3.7), however, in an elliptic cylindrical coordinate system. Its origin and z -axis are the same as those in the Cartesian coordinate system, whereas the rest coordinates (ν, ϑ) in the transverse plane can be transformed to (x, y) via

$$x = r \sinh \nu \cos \vartheta, \quad (3.15)$$

$$y = r \cosh \nu \sin \vartheta, \quad (3.16)$$

Table 3.3 Design parameters of the rectangular cavity. The characteristic shunt impedances are sampled at the left end, in the middle, and at the right end of the horizontal axis of symmetry of the aperture.

Item	Value	Unit
Height	180	cm
Width	100	cm
Depth	16	cm
Skewness	2.63	cm
Resonant frequency	171.48	MHz
Charac. shunt impedance (left)	1.5	Ω
Charac. shunt impedance (middle)	37.3	Ω
Charac. shunt impedance (right)	73.1	Ω

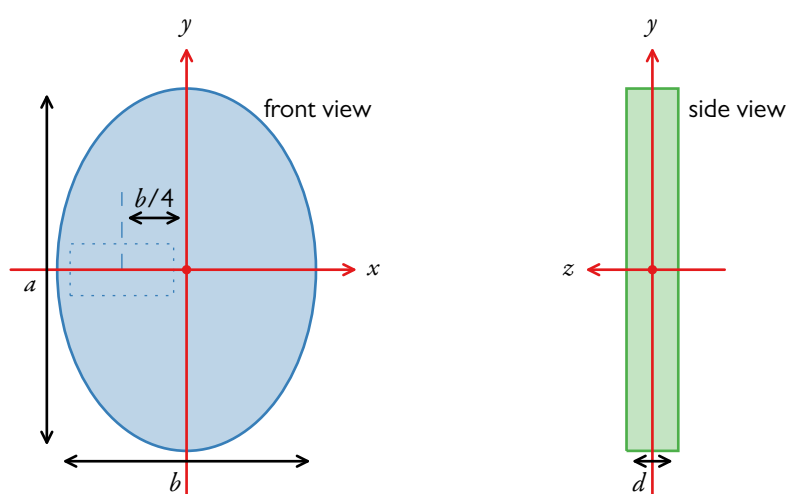


Figure 3.10 Similar to fig. 3.6, for an elliptic cavity.

where the radial coordinate ν is a nonnegative real number, and the azimuthal coordinate ϑ is between 0 and 2π . The electric field in the monopole mode is given as

$$E_\nu = 0, \quad (3.17)$$

$$E_\vartheta = 0, \quad (3.18)$$

$$E_z = E_0 \text{Ce}_0(\nu; \tilde{u}) \text{ce}_0\left(\vartheta + \frac{\pi}{2}; \tilde{u}\right), \quad (3.19)$$

where E_0 is a scaling factor, ce_0 is the even Mathieu equation of order zero, Ce_0 is the even modified Mathieu equation of order zero, and \tilde{u} is a particular parameter that is determined by the ratio b/a . The reader is advised to refer to appendix A.3 for more details. Note that eq. (3.19) slightly differs from eq. (A.86), because the elliptic coordinates have been rotated counterclockwise by $\pi/2$. Moreover, the resonant frequency f_0 of the monopole mode is determined by a and b via

$$f_0 = \frac{2c}{\pi} \sqrt{\frac{\tilde{u}}{a^2 - b^2}}. \quad (3.20)$$

The characteristic shunt impedance of the elliptic cavity can be calculated by substituting eqs. (3.19) and (3.20) into eq. (2.37), and using eq. (2.17):

$$\frac{R_{\text{sh}}}{Q_0} = \frac{2\mu_0 cd}{\sqrt{\tilde{u}(a^2 - b^2)}} \frac{\text{Ce}_0^2(\tilde{\nu}; \tilde{u}) \text{ce}_0^2(\tilde{\vartheta} + \pi/2; \tilde{u})}{\int_0^{\text{artanh}(b/a)} d\tilde{\nu} \int_0^{2\pi} d\tilde{\vartheta} (\sinh^2 \tilde{\nu} + \cos^2 \tilde{\vartheta}) \text{Ce}_0^2(\tilde{\nu}; \tilde{u}) \text{ce}_0^2(\tilde{\vartheta} + \pi/2; \tilde{u})}, \quad (3.21)$$

where $\tilde{\nu}$ and $\tilde{\vartheta}$ are dummy variables.

The dependence of f_0 on (a, b) is visualized in the left panel of fig. 3.11. The skewness can be de-

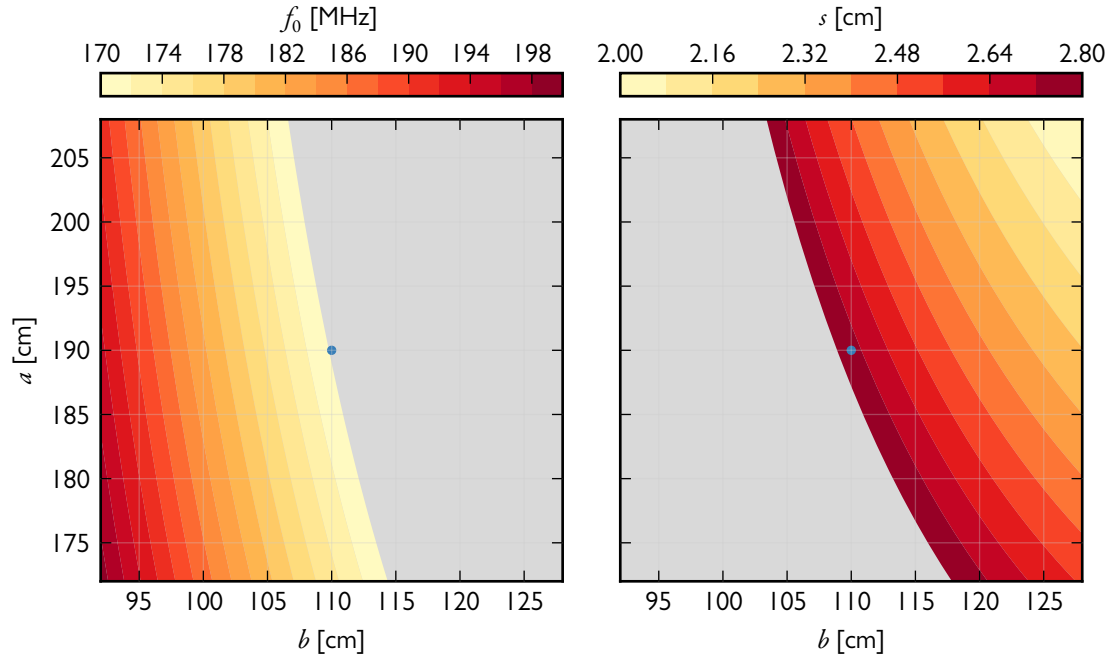


Figure 3.11 Similar to fig. 3.7, for an elliptic cavity.

finied in the same manner as before. However, an analytic formula of s is impossible to attain. The dependence of s on (a, b) by numerical means is visualized in the right panel of fig. 3.11. Based on the dependence graph, the optimum $(a, b) = (190, 110)$ is hence chosen, which leads to a resonant frequency of 169.76 MHz and a skewness of 2.75 cm.

According to eq. (3.21), a minimum depth of 15.63 cm is compulsory for the elliptic cavity to fulfill the requirement of the shunt impedance in table 3.2. The final decision is made on 16 cm, which happens to be identical for both rectangular and elliptic cavity. Likewise, the transit time factors and shunt impedance map for the elliptic cavity are plotted in figs. 3.12 and 3.13, respectively. The key parameters of the elliptic cavity are listed in table 3.4.

Although the two cavities are intentionally designed to be comparable, some subtle differences are still in existence. For instance, the height and width of the elliptic cavity are a little larger than those of the rectangular cavity, which results in a slightly lower resonant frequency. By comparison between figs. 3.9 and 3.13, it is found that the contour of the shunt impedance map is straighter for the rectangular cavity. However, the quantitative comparison between tables 3.3 and 3.4 reveal that the elliptic cavity exhibits a bit higher shunt impedance in the whole aperture region. The transit time factors, on the other hand, are nearly the same for both cavities.

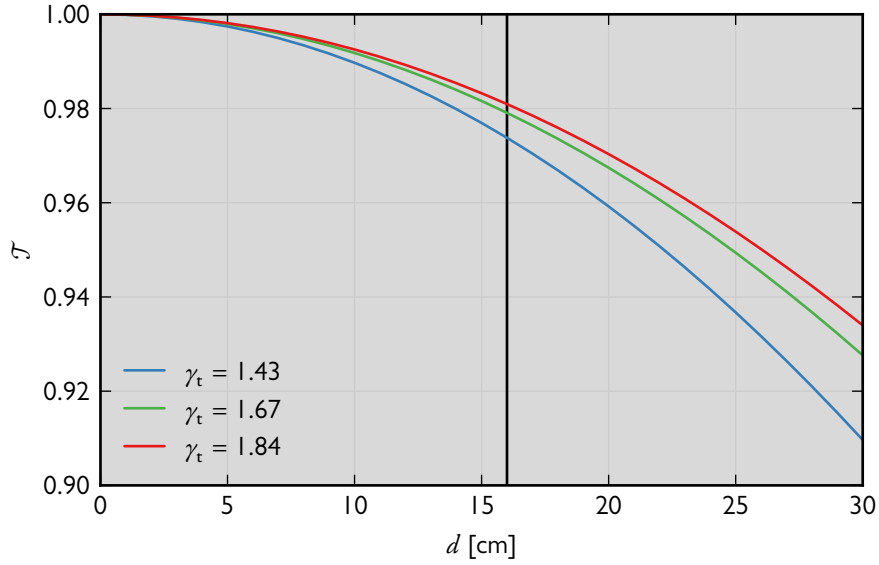


Figure 3.12 Similar to fig. 3.8, for the elliptic cavity.

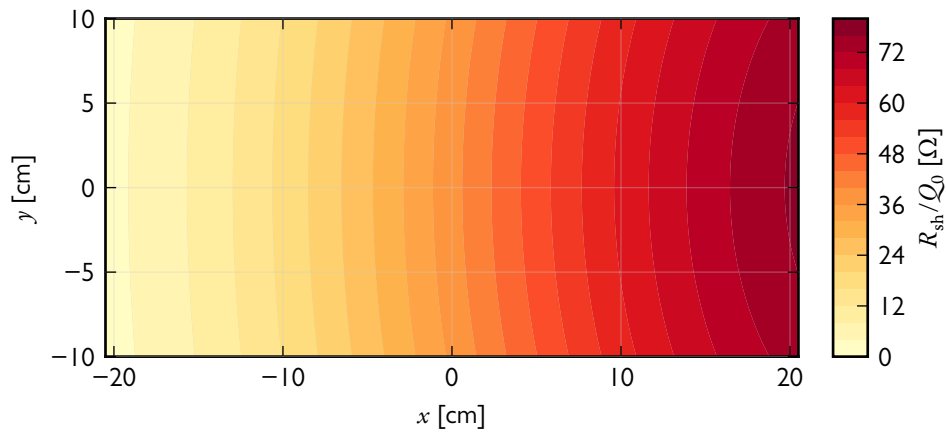


Figure 3.13 Similar to fig. 3.9, for the elliptic cavity.

Table 3.4 Similar to table 3.3, for the elliptic cavity.

Item	Value	Unit
Height	190	cm
Width	110	cm
Depth	16	cm
Skewness	2.75	cm
Resonant frequency	169.76	MHz
Charac. shunt impedance (left)	2.8	Ω
Charac. shunt impedance (middle)	38.6	Ω
Charac. shunt impedance (right)	76.8	Ω

3.4 Computational Refinement

Once the structure of a cavity becomes complex, the analytic approach is no longer adequate to carry on the design process. Fortunately, computer codes by numerical means are available to take over

to solve Maxwell's equations in a meshed volume. Here, a proprietary software—CST MICROWAVE STUDIO[®]—is adopted to simulate EM fields inside the rectangular and elliptic cavity, when beam pipes and plungers are incorporated.

Before the tool is deployed, it should be benchmarked in order to demonstrate its reliability. The calculations of the resonant frequency and shunt impedance are hence repeated by the CST for both cavities. The simulated values are listed in table 3.5. By comparison to tables 3.3 and 3.4, it is found

Table 3.5 Benchmarking of the CST by calculating the resonant frequencies and the characteristic shunt impedances of both cavities. The indicated locations in parentheses are the same as those described in table 3.3.

Cavity	Rectangular	Elliptic
Resonant frequency [MHz]	171.48	169.76
Charac. shunt impedance (left) [Ω]	1.5	2.8
Charac. shunt impedance (middle) [Ω]	37.2	38.6
Charac. shunt impedance (right) [Ω]	73.1	76.8

that the simulated results are in excellent agreement with the analytic solutions.

3.4.1 Apertures with Beam Pipes

In order to allow for the beam passage, two opposite rectangular apertures need to be machined on the flat ends of the cavity. The center of the aperture is horizontally offset from the center of the cavity to the left side by a quarter width of the cavity. In addition, a beam pipe is attached to each aperture to mimic the vacuum chamber in the CR. The length of the pipe is three times as much as the depth of the cavity, i.e. 48 cm.

The two kinds of cavities together with the beam pipes are modeled with the CST, and the electric fields are simulated subsequently. Afterwards, the characteristic shunt impedances are calculated according to eq. (2.37). Note that the CST has internally normalized the EM fields to a total energy of 1 J. The definite integral of E_z in the numerator in eq. (2.37) is approximated by using the trapezoidal rule between $z = \pm 56$ cm with a step of 0.2 cm.

The results are visualized in the shunt impedance maps in figs. 3.14 and 3.15 for both cavities.

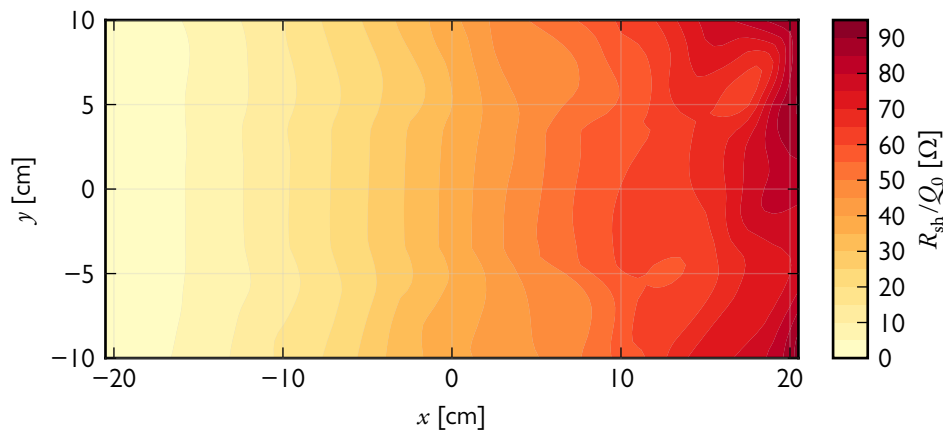


Figure 3.14 Shunt impedance map of the rectangular cavity in the aperture region with beam pipes attached.

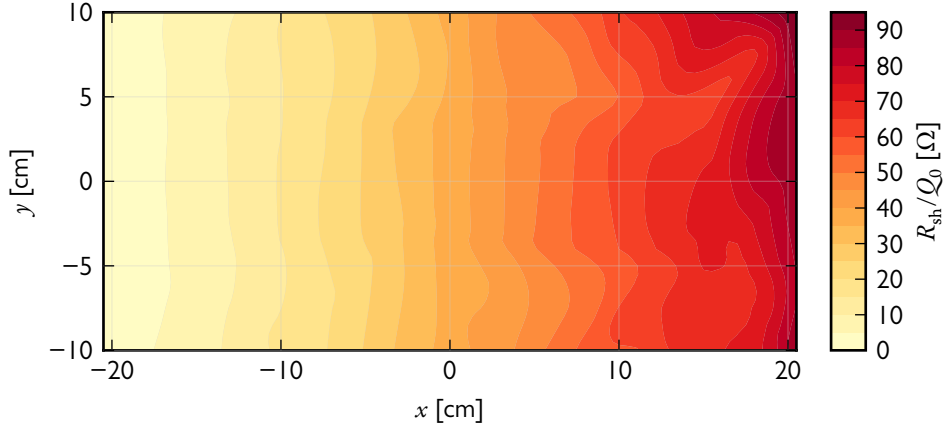


Figure 3.15 Similar to fig. 3.14, for the elliptic cavity.

Unfortunately, an abnormal pattern is presented for both cavities. This is due to the abrupt edges of the apertures, where the EM fields are severely distorted by the discontinuity of the boundary condition. As a remedy, the edges are rounded by a radius of 1.2 cm (fig. 3.16). The resultant shunt impedance

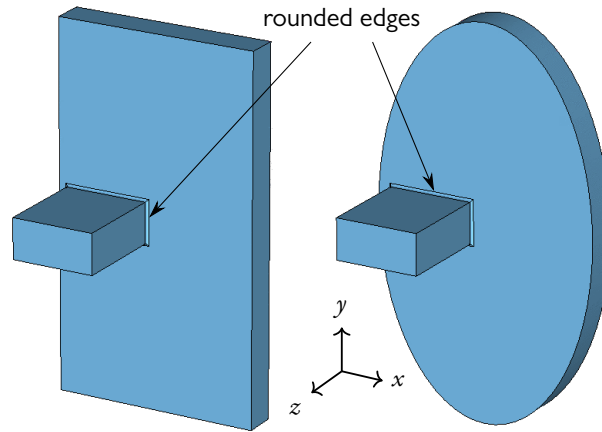


Figure 3.16 Three-dimensional models of the rectangular and elliptic cavity used for the simulation with the CST. The edges formed between the cavities and beam pipes are rounded by a radius of 1.2 cm.

maps are presented in figs. 3.17 and 3.18.

It is apparent from figs. 3.17 and 3.18 to find that in spite of the ripples folded on the contours, the shunt impedances follow a general ascending trend from left to right. The contours in the right half are denser than those in the left half, which means a better position resolution ought to be expected near the cavity center, whereas in the middle region the contours still resemble straight lines. The dynamic ranges of the shunt impedances are also enhanced to more than 80Ω , because of the extra electric fields extending into the beam pipes from the neighborhoods.

3.4.2 Higher-Order Modes

Although the position cavity is designed to resonate in the monopole mode with the lowest resonant frequency, the coupled signal may get contaminated by other Higher-Order Modes (HOMs). This can be caused by a significant presence of the electric field in a HOM in the aperture region, which interacts with the beam as it passes through the cavity. This effect will even become prominent, if the

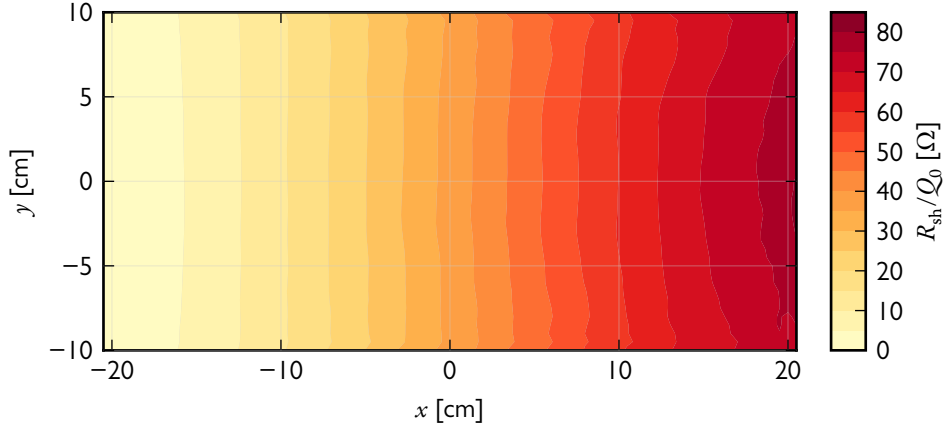


Figure 3.17 Shunt impedance map of the rectangular cavity in the aperture region with pipes attached and edges rounded.

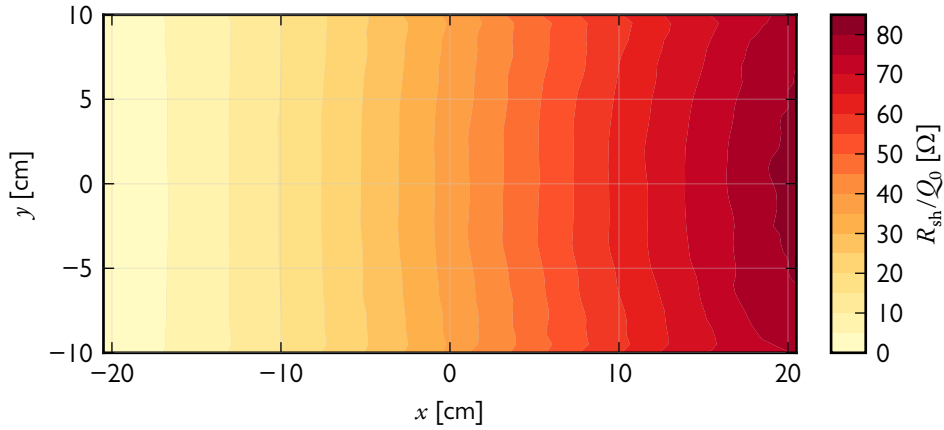


Figure 3.18 Similar to fig. 3.17, for the elliptical cavity.

resonance curve of the HOM is so broad that it extends to the frequency regime of the monopole mode. To study the possible contaminations by the HOMs, the EM fields in two other modes, namely dipole and tripole mode, are also simulated with the CST.

The resonant frequencies of two cavities in the monopole, dipole, and tripole mode are listed in table 3.6 for comparison. It is then apparent that the three modes of the elliptical cavity spread a little

Table 3.6 Resonant frequencies of the first three modes in the rectangular and elliptical cavity.

Eigenmode	Rectangular f_0 [MHz]	Elliptical f_0 [MHz]
Monopole	171.546	170.043
Dipole	218.956	228.083
Tripole	292.860	300.622

more sparsely in frequency. Moreover, the shunt impedance maps in the HOMs for both cavities are presented in figs. 3.19 to 3.22. By comparison between figs. 3.19 and 3.21, the shunt impedance maps are similar for the rectangular and elliptical cavity. The rather low magnitude of the shunt impedance implies a weaker coupling strength between the cavity and beam in the dipole mode than that in the

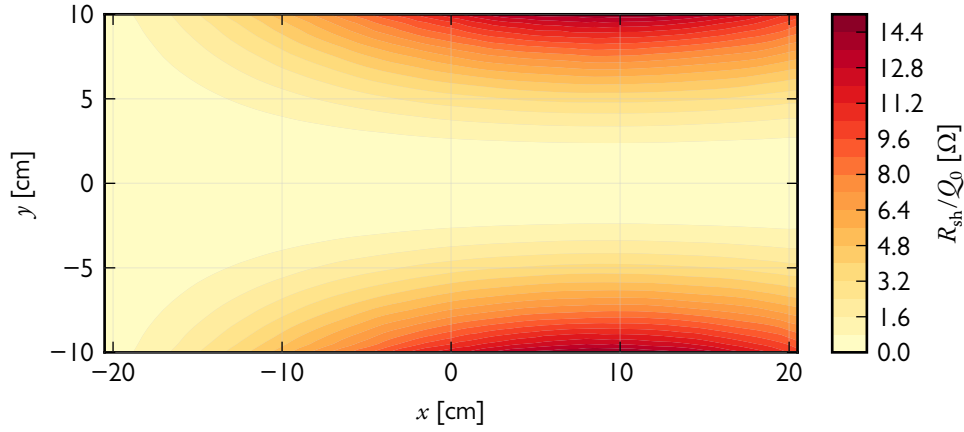


Figure 3.19 Similar to fig. 3.17, for the dipole mode.

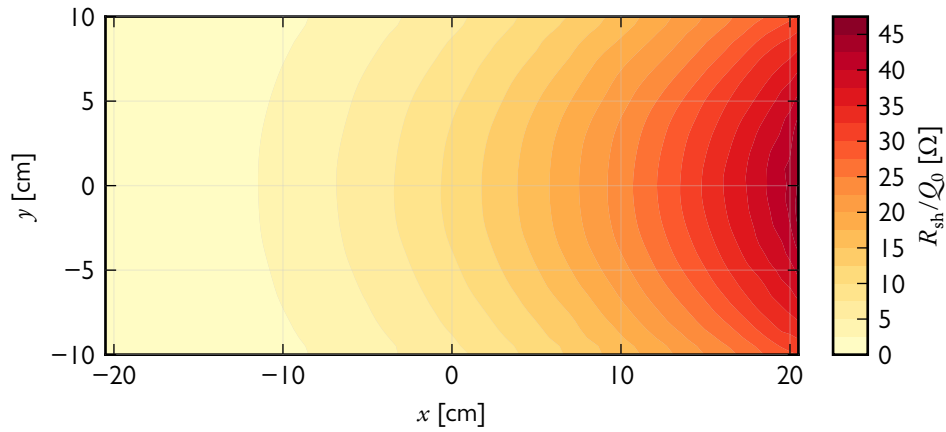


Figure 3.20 Similar to fig. 3.17, for the tripole mode.

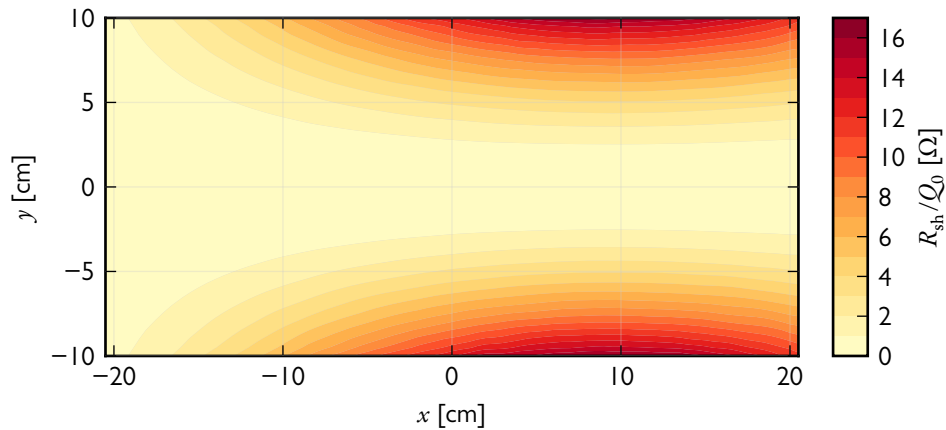


Figure 3.21 Similar to fig. 3.19, for the elliptic cavity.

monopole mode. In contrast, according to figs. 3.20 and 3.22, the shunt impedance maps exhibit distinct patterns in the tripole mode for the two cavities. Although the shunt impedance is insignificant for the elliptic cavity, it surely presents a moderate magnitude for the rectangular cavity in particular near the cavity center. However, according to table 3.6, the tripole mode is much separated from the

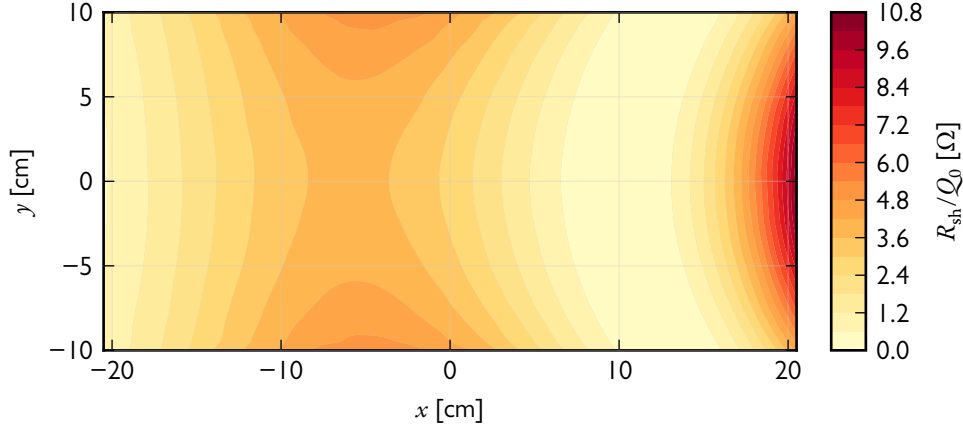


Figure 3.22 Similar to fig. 3.20, for the elliptic cavity.

monopole mode in frequency, and can hence be rejected by a proper band-pass filter.

As a precautionary measure, several probe couplers terminated by 50Ω resistances can be mounted onto the position cavity to damp the dipole and tripole mode [138]. They will be located on a flat end of the cavity at the antinodes of the electric fields in the HOMs so as to efficiently absorb the EM energies from these parasitic modes. By means of simulation, the coordinates (x, y) of the antinodes in centimeter, after being rounded to the nearest integer, are listed in table 3.7 for the rectangular and elliptic cavity. Note that for the tripole mode, there is in fact one more antinode lying in the horizontal

Table 3.7 Transverse coordinates of the antinodes of the electric fields in the Higher-Order Modes (HOMs) for the rectangular and elliptic cavity. The origin of the coordinates is in the center of each cavity.

HOM	Rectangular		Elliptic	
	x [cm]	y [cm]	x [cm]	y [cm]
Dipole	-2	± 42	-2	± 40
Tripole	-4	± 60	-12	± 52

central plane of the cavity. However, this location is reckoned not suitable for mounting a damping coupler because it will act on the monopole mode as well.

3.4.3 Installation of Plungers

Since the CR will be operated in the three isochronous modes with various transition energies, the resonant frequency of the position cavity will fall into the Schottky bands of the isochronous ions at different harmonics. In order to maximize the signal-to-noise ratio, the resonant frequency f_0 should preferably align with the revolution frequency f_{rev} of the isochronous ion at the corresponding harmonic. Based on the revolution frequencies in table 3.1, and the simulated resonant frequencies of the rectangular cavity (171.55 MHz) and the elliptic cavity (170.04 MHz), the target resonant frequencies of both cavities can be calculated for all the isochronous modes. The results are listed in table 3.8.

Consequently, the detuning interval of the resonant frequency is [171.536, 172.356] MHz for the rectangular cavity, and [170.188, 170.4] MHz for the elliptic cavity. This can be attained by installing plungers into the cavity. The installation spots are on the circumference of the cavity on the right hand side, such that the plungers will not interfere too much with the electric field in the aperture region,

Table 3.8 Target resonant frequencies of the rectangular and elliptic cavity in accord with the revolution frequencies in the three isochronous modes.

Mode	Isochronous		Rectangular		Elliptic	
	f_{rev} [MHz]	Harmonic	f_0 [MHz]	Harmonic	f_0 [MHz]	
I	0.968	178	172.304	176	170.368	
II	1.084	159	172.356	157	170.188	
III	1.136	151	171.536	150	170.400	

but can also detune the resonant frequency by reshaping the boundary on the edge. For the sake of symmetry, two cylindrical plungers with a radius of 6 cm are placed in the horizontal planes at $y = \pm a/4$ for each cavity (fig. 3.23). Due to the curvature of the side face of the elliptic cavity, the plungers are

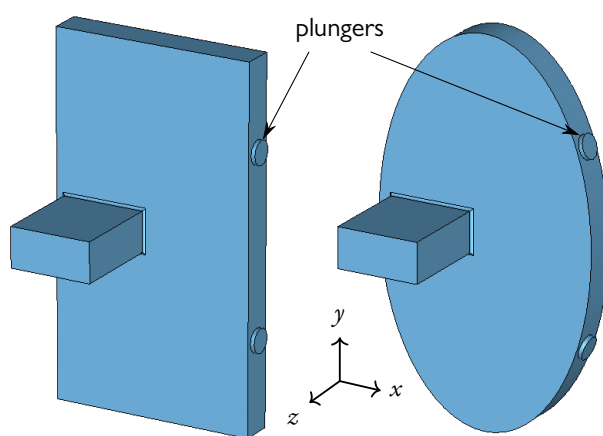


Figure 3.23 Three-dimensional models of the rectangular and elliptic cavity featuring plungers installed on the circumferences. The locations of plungers are offset halfway from the horizontal central plane to either side. The orientation of the plungers for the elliptic cavity are also rotated by an angle of $\pm 18.5^\circ$ to meet the curvature of the circumference.

angled at 18.5° to orthogonally fit into the surface.

In the detuning procedure, two plungers will be moved inwards or outwards by a stepper motor with the same displacement. The dependencies of the resonant frequency f_0 on the plunger position x_{pl} are simulated with the CST for the rectangular and elliptic cavity, which are shown in figs. 3.24 and 3.25, respectively. The green area indicates the detuning interval of the resonant frequency, while the red dot stands for the initial resonant frequency where the plungers align with the cavity wall. Clearly, a wider tunable range is required for the rectangular cavity, which corresponds to a displacement range of nearly 5 cm.

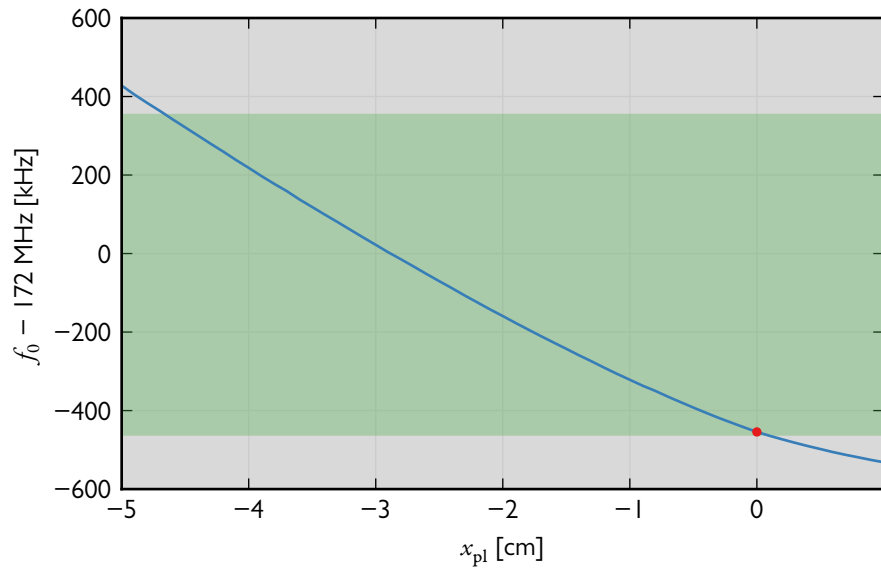


Figure 3.24 Detuned frequency of the rectangular cavity as a function of the plunger position. The negative position means that the plungers are inside the cavity. The green band represents the target zone, while the red dot indicates the initial resonant frequency.

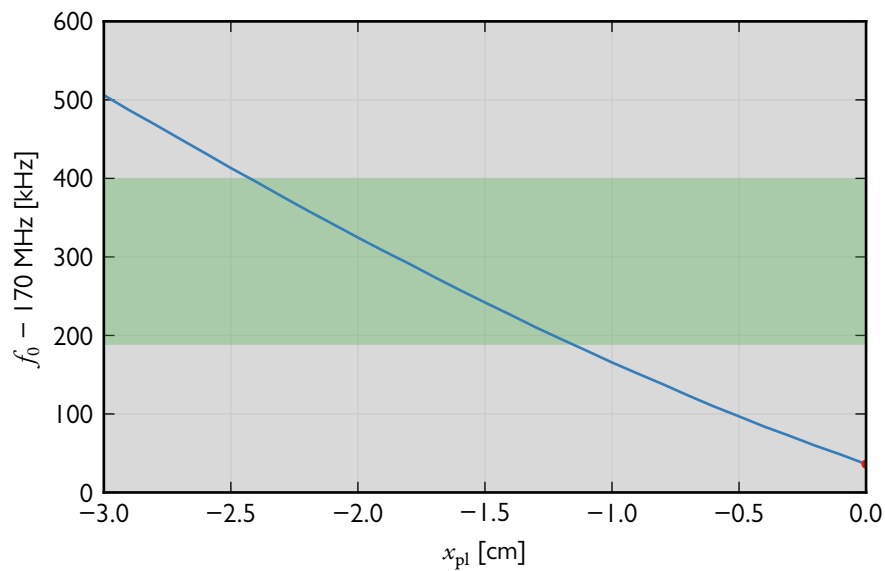


Figure 3.25 Similar to fig. 3.24, for the elliptic cavity.

4 EMPIRICAL JUSTIFICATION



As an old proverb goes, “the proof of the pudding is in the eating”. One cannot judge the quality of anything until one has tried, used, or experienced it. The same holds for the development of a cavity. No matter how convincing the analytic and computational results in chapter 3 may look like, without being tested in practice, it is nothing but a design concept. When the concept is being put into realization, it will most likely face a lot of practical challenges arising from different aspects in an unexpected way. Therefore, technically speaking, the development will never be finished until the position cavity is installed into the CR and functions normally as expected. Unfortunately, this long-term goal is already beyond the time scale of the present thesis work. But for now, some empirical actions, such as manufacture of prototypes and benchtop tests on them, have been taken to advance one step closer towards the final goal.

4.1 Prototype Cavities

Based on the conceptual design, two scaled prototypes of the rectangular and elliptic cavity have been considered to manufacture. All the dimensions—the heights, widths, and depths of the cavities, as well as those of the beam pipes—are scaled down by a factor of four in order to adapt to the test bench. Moreover, the rounding radius of the edges of the apertures and the radius of the plungers are also reduced by the same factor. The new sizes are listed in table 4.1. According to eqs. (3.11) and (3.20),

Table 4.1 Dimensions of the scaled prototype cavities, as well as the associated parts.

Item	Height [cm]	Width [cm]	Depth [cm]	Radius [cm]
Rectangular	45	25	4	–
Elliptic	47.5	27.5	4	–
Pipe	5	10.25	12	–
Plunger	5	–	–	1.5
Rounded Edge	–	–	–	0.3

the new resonant frequency will be four times as much as the original one, which is 686.18 MHz for the rectangular prototype and 680.17 MHz for the elliptic prototype. On the contrary, the characteristic shunt impedance will not be affected by the scaling according to eqs. (3.12) and (3.21).

Apart from the two prototypes, a calibration cavity is additionally designed. It will be used to determine the relative permittivity of a dielectric bead, which is crucial for profiling the electric fields inside the prototypes by means of perturbation. The shape of a circular pillbox is selected for the calibration cavity, because it is so simple that the cavity can precisely be manufactured, and the EM fields can analytically be computed. The radius of the cavity is 16.8 cm such that the resonant frequency of

the monopole mode—682.98 MHz according to eq. (A.60)—lies between the resonant frequencies of both prototypes. Only by this means can the determined relative permittivity be helpful in the frequency region of interest. During the calibration process, the bead with a diameter of 5 mm will be placed in the center of the cavity. In order to minimize the image charge effect, the depth of the cavity is chosen to be 10 cm. The three-dimensional models of the cavity family are depicted in fig. 4.1.

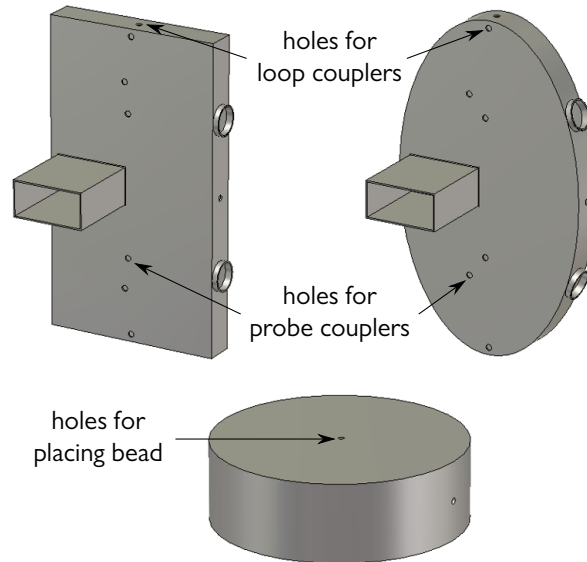


Figure 4.1 Three-dimensional models of the rectangular, elliptic, and circular prototype cavity. The pairs of the big holes on the sides of the rectangular and elliptic cavity are reserved for plungers. The small holes on the three cavities are intended for different purposes. The unoccupied ones will be blocked by screws. See the text for more details.

For the capability of mounting couplers, a number of holes are to be bored through on the cavity walls, of which some are visible in fig. 4.1. These holes will then be threaded to match a BNC bulkhead jack connector. The boring locations of the holes are mirror symmetric about the horizontal central plane of the cavity. For all the three cavities, the holes on the circumferences are intended for mounting loop couplers to pick up the magnetic fields, while the ones on the flat ends serve different purposes. In the cases of the rectangular and elliptic cavity, the holes on the front faces coincide with the antinodes of the electric fields, based on, after scaling down by a factor of four, table 3.7, and will be used for mounting probe couplers to damp the HOMs, except for those lateral holes which are used for coupling signals with loop couplers. The hole on the lid of the circular cavity allows for suspending the perturbing bead with a cotton thread. During the benchtop tests, the unoccupied holes will be blocked by screws so as to restore the boundary condition at these locations. For this reason, the hole is in fact a placeholder, which is extensible for the supplementary features on demand.

The prototypes have been manufactured by Kreß GmbH in Biebergemünd, based on the engineering drawings in appendix B. Each cavity was machined in two parts: a flat lid and a hollow body with the circumference. The body part was milled out of a bulk of aluminium alloy AlMgSi1. This kind of material is well known for its light weight, good electrical conductivity, and high corrosion resistance. For the lid, the material was changed to AlMg4.5Mn due to its excellent flatness tolerance and exceptional shape stability. Afterwards, these two parts were assembled by screwing firmly with helical thread inserts used. In contrast to welding, this can retain the shape of each part without introducing any heat distortion whatsoever. Like the cavity bodies, the beam pipes were also made of AlMgSi1, whereas the blocking screws and plungers were made of stainless steel 1.4301 due to its great hardness for being compatible with threading. The inner edges of the rectangular cavity and those of the beam

pipes in the longitudinal direction are rounded by a radius of 3 mm instead of being right angles, due to the size limit of the milling cutter. The thickness of all the cavity walls are at least 10 mm, which is the length of the blocking screws. Therefore, the holes were first counterbored to reduce the local thickness wherever necessary. To help the rectangular and elliptic cavity stand on the test bench, a pair of upright holders were also built for each of them. The final products are pictured in fig. 4.2.

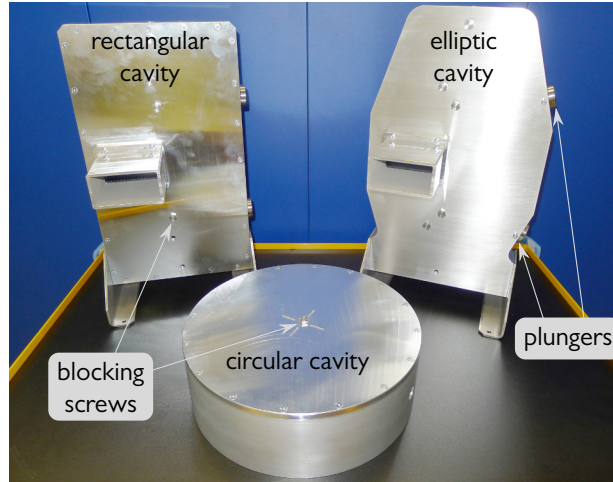


Figure 4.2 Photograph of the rectangular, elliptic, and circular prototype cavity.

4.2 Scattering Parameters

The scattering parameters (S -parameters) play a central role in characterizing the RF responses of a multi-port network to EM stimuli in the microwave regime [147]. For high frequencies, the concepts of voltage and current are no longer adequate to describe a circuit, because the EM wavelengths are so short that the circuit elements are actually distributed over the whole network, and quite often, it is not so easy to accurately define the reference planes. Therefore, the so-called power wave can be adopted instead, if the power relations among different ports of the network are the main concern [148].

While a more general definition about the power wave in a multi-port network has been given in [148], a basic two-port network is treated here, which is illustrated in fig. 4.3. At the n th port with $n = 1$ or 2 , the incident power wave a_n and the reflected power wave b_n are defined as

$$a_n = \frac{V_n + Z_0 I_n}{2\sqrt{Z_0}}, \quad (4.1)$$

$$b_n = \frac{V_n - Z_0 I_n}{2\sqrt{Z_0}}, \quad (4.2)$$

where V_n and I_n are the voltage and current flowing into the port, respectively, and Z_0 is an arbitrary reference impedance, but normally chosen to be the characteristic impedance of the transmission line. The incident and reflected power at this port are simply $|a_n|^2$ and $|b_n|^2$, respectively.

Now assume that the network only contains linear elements. The relations between $\{b_n\}$ and $\{a_n\}$ can thus be expressed by a set of linear equations:

$$b_1 = S_{11}a_1 + S_{12}a_2, \quad (4.3)$$

$$b_2 = S_{21}a_1 + S_{22}a_2, \quad (4.4)$$

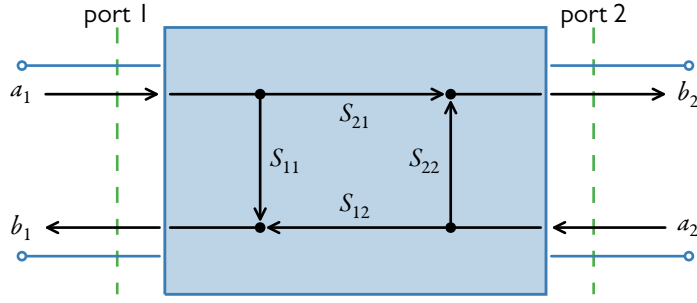


Figure 4.3 Two-port network featuring the S -parameters between the ports. An incident power wave is represented by an arrow pointing inwards a port, while an arrow pointing outwards represents a reflected power wave.

or in the matrix form:

$$\begin{pmatrix} b_1 \\ b_2 \end{pmatrix} = \begin{pmatrix} S_{11} & S_{12} \\ S_{21} & S_{22} \end{pmatrix} \begin{pmatrix} a_1 \\ a_2 \end{pmatrix}, \quad (4.5)$$

$$\mathbf{b} = \mathbf{S}\mathbf{a}, \quad (4.6)$$

where \mathbf{S} is known as the power wave scattering matrix. Each element of the matrix is an S -parameter.

For instance, S_{11} can be calculated via

$$S_{11} = \left. \frac{b_1}{a_1} \right|_{a_2=0} = \frac{Z_1 - Z_0}{Z_1 + Z_0}, \quad (4.7)$$

where eqs. (4.1) and (4.2) have been substituted in, and Z_1 is the shunt impedance looking into the first port. The right hand side of eq. (4.7) is recognized as the reflection coefficient at the first port. Actually, all the diagonal elements in a scattering matrix are the reflection coefficients at the corresponding ports of a multi-port network [148]. On the other hand, the off-diagonal elements quantify the transmission behaviors between any two ports.

For a two-port network, if $S_{12} = S_{21}$ then it is reciprocal. Most passive elements—such as resistor, capacitor, inductor, and transformer—are reciprocal. If $S_{11} = S_{22}$ also holds, then the network is symmetric as well. Moreover, the network is lossless if \mathbf{S} is unitary, i.e. $\mathbf{S}^\dagger \mathbf{S} = \mathbf{1}$, where the dagger denotes conjugate transpose.

In general, the S -parameters are complex numbers, so are the impedances. Equation (4.7) actually projects the impedance plane to the reflection coefficient plane in complex domain via the Möbius transformation [149]:

$$\Gamma_1 = \frac{Z_1/Z_0 - 1}{Z_1/Z_0 + 1}. \quad (4.8)$$

This has been demonstrated to be a powerful tool, and been exploited intensively in microwave engineering. The most widely used application may be the renowned Smith chart [150]. It is essentially the polar representation of the reflection coefficient, but with circular grids added to indicate the corresponding impedances before the transformation. It has proven to be extremely useful for analyzing lumped element circuits and solving matching problems.

In the high- Q approximation, an RF cavity can be modeled as a parallel circuit with a resistor, a capacitor, and an inductor in the vicinity of its resonance [151]. The resistance is a constant, whereas the capacitance and inductance vary with frequency. In the impedance plane, as the frequency sweeps, the locus is a straight line perpendicular to the real axis, where the intercept is on the resonance. Correspondingly, the locus of the reflection coefficient is a circle, due to the property of the circle inversion of the Möbius transformation. The size of the circle indicates the coupling coefficient κ , e.g. the former collapses to a point when $\kappa = 0$. An accurate estimation of the coupling coefficient can be obtained by a linear fractional curve fitting of the reflection coefficient [151].

The transmission coefficient S_{21} , on the other hand, is usually interpreted in a Cartesian coordinate system where the square of its magnitude is plotted versus the frequency. It is the ratio between the delivered power at port 2 and the available power at port 1, and hence proportional to the EM energy stored in the cavity. According to eq. (2.27), $|S_{21}|^2$ can be fitted by a Lorentzian function. Afterwards, the resonant frequency and quality factor are straightforward to obtain from the fitting parameters. Note that the quality factor here is the loaded one Q_{load} , since the couplings at two ports are present.

In practice, the S -parameters of a cavity can be measured by a Vector Network Analyzer (VNA). Usually the two ports of a Device Under Test (DUT) are connected with the test ports on the VNA via phase-stable precision cables. Depending on the S -parameter to be measured, the RF generator at each port is accordingly switched on or off. The incident and reflected power waves at each port are separated by a directional coupler. Then, these two courses of waves are processed by the independent reference and measurement channels, respectively. The ratio between them are analyzed by a built-in computer and displayed on the screen. In order to minimize systematic errors, the VNA ought to be calibrated at both ports under the Match, Open, Short, and Through (MOST) conditions prior to the test.

4.3 Static Test

The benchtop tests on the prototypes proceed in two subsequent steps, namely static and dynamic test. In the former, a cavity under test is staying still for the measurements of several scalar RF properties, such as the resonant frequency and quality factor. The effect of the ambient temperature and the detuning by perturbations are also addressed in the static test.

4.3.1 Test Bench Setup

The setup of the test bench is pictured in fig. 4.4. It mainly consists of two measuring instruments, i.e. a VNA and a digital multimeter, a controlling PC, and a cavity under test. Two loop couplers are mounted on the circumference of the cavity. The coupler is based on a BNC bulkhead jack connector soldered with a silver wire on top of it (fig. 4.5). It is then screwed into a side hole of the cavity, and locked by a nut squeezing against a star washer (fig. 4.6). The VNA (Rohde & Schwarz ZVL6) is first calibrated with a calibration kit (Rohde & Schwarz ZV-Z135), then connected to the two couplers via high-quality microwave cables (HUBER+SUHNER SUCOFLEX_104_PE) to measure the S -parameters of the cavity. In addition, the multimeter (Agilent 34410A) logs the ambient temperature with a thermistor (Agilent E2308A) during the test. Both instruments are remotely controlled by the PC running on a Linux system. They are communicated over Ethernet through an Ethernet hub with the PC.

On the software side, a dedicated Java application has been prepared to handle all the communications between the PC and instruments. First, the PC sends out instructions with the syntax of the Standard Commands for Programmable Instruments (SCPI) to the VNA and multimeter to initiate the measurement. Afterwards, the PC retrieves measured data from the instruments when they have

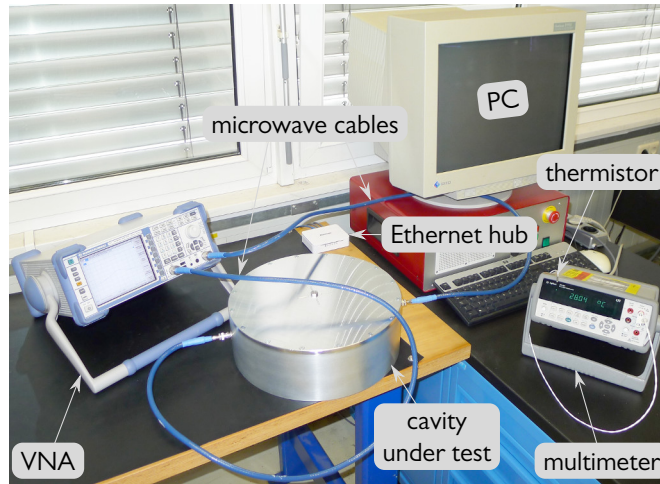


Figure 4.4 Setup of the static test bench. The cavity under test is exemplified by the circular one. The Vector Network Analyzer (VNA) measures the S -parameters, while the multimeter together with the thermistor monitors the ambient temperature. The PC coordinates the entire test process. See the text for more details.

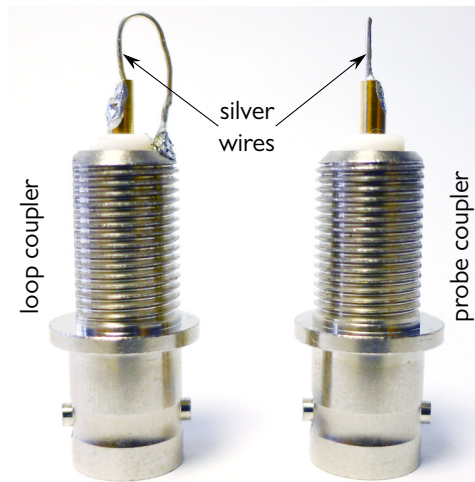


Figure 4.5 Closeup of a loop and a probe coupler based on BNC bulkhead jack connectors. The loop and probe are made from silver wires, and soldered on top of the connectors.

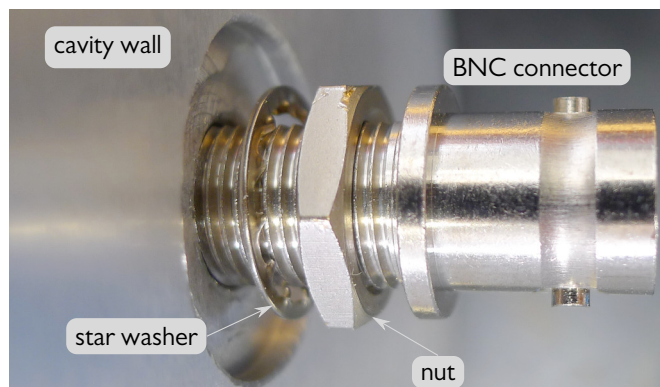


Figure 4.6 Closeup of mounting a BNC connector, which can be locked by the nut squeezing against the star washer.

taken ten consecutive measurements and averaged the results. The data are then written to the local disk in the form of plain text, and can later be accessed by any networked computer within GSI.

4.3.2 Debut of Prototypes

The first impression on the prototypes in terms of RF properties is presented by their S -parameters. From the S_{21} measurements, the resonant frequencies and quality factors can be deduced. Although the presence of the two loop couplers will inevitably influence the measured results, their effect can be minimized by carefully turning the orientations of the loops such that the resonance circles of S_{11} and S_{22} almost collapse to points. This condition will always be examined for the three cavities throughout the entire benchtop test.

The frequency span for the measurements is selected to be approximately three times as much as the FWHM of the resonance curve of a cavity. The span is then evenly sampled to 801 frequencies by the VNA, at which the reflection and transmission coefficients are measured. The S_{11} and S_{22} of the circular cavity are plotted in a polar system in fig. 4.7, while the $|S_{21}|^2$ is plotted against f in a Cartesian system in fig. 4.8.

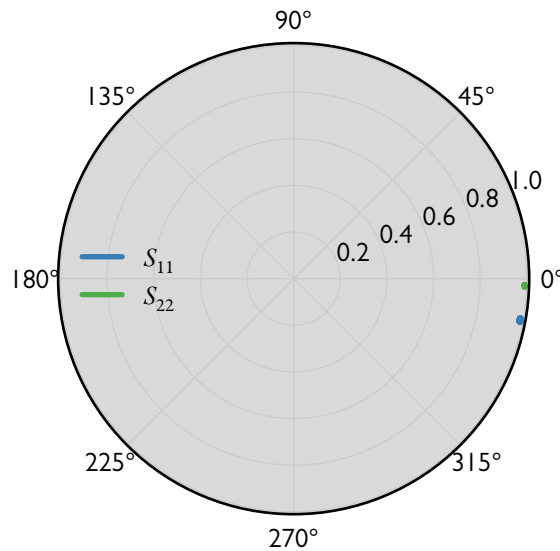


Figure 4.7 Reflection coefficients of the circular cavity in a polar system. The coupling coefficients at both ports are negligible, since the resonance circles almost collapse to points.

It is clear in fig. 4.7 that the coupling coefficient is negligible. Therefore, the quality factor obtained from fig. 4.8 is almost the unloaded one. By fitting the resonance curve in fig. 4.8 with a Lorentzian function, the resonant frequency f_0 is 682.770 63(8)(68) MHz, and the unloaded quality factor Q_0 is 14 845(62). Note that the uncertainty of the resonant frequency comprises statistic (first) and systematic (second) contribution. The statistic uncertainty is a result of the parametric fitting by incorporating an intrinsic uncertainty of 0.3 dB for each point on the trace, while the systematic uncertainty is due to an instability of 10^{-6} of the internal reference frequency of the VNA. When computing the unloaded quality factor by using eq. (2.28), both uncertainties are taken into account.

Likewise, the same loop couplers are mounted laterally on the front face of either the rectangular or the elliptic cavity for test. The results of the transmission measurements of both cavities are plotted in figs. 4.9 and 4.10, while the plots for the reflection measurements are very similar to fig. 4.7, and thus omitted for brevity. The variance among the magnitudes of the resonance curves in figs. 4.8 to 4.10 is caused by the slightly different coupling coefficients for the three cavities.

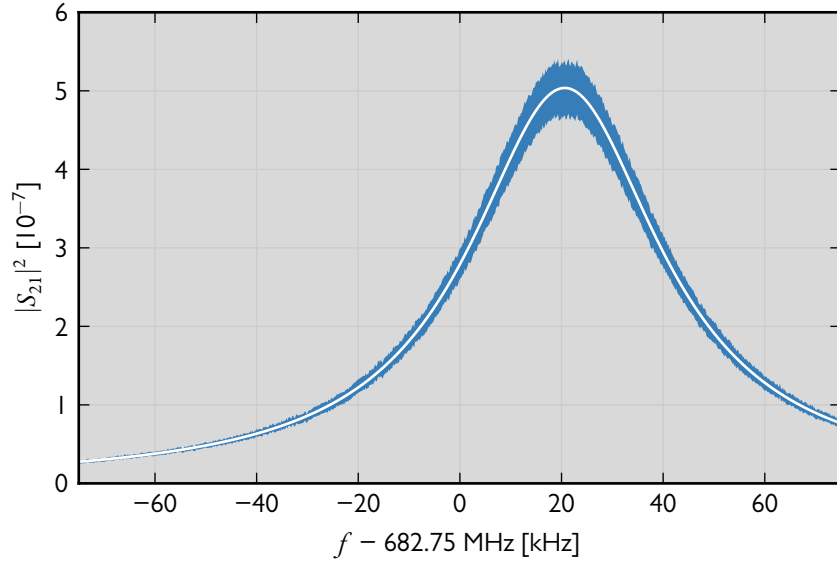


Figure 4.8 Resonance curve of the circular cavity. Shown in blue is the measured $|S_{21}|^2$ together with an uncertainty of 0.3 dB at each trace point. Shown in white is the fitted Lorentzian function.

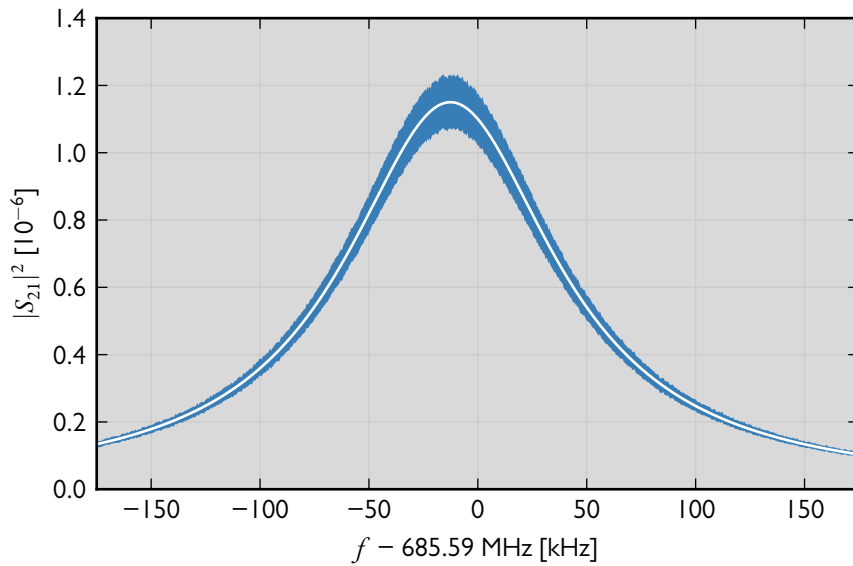


Figure 4.9 Similar to fig. 4.8, for the rectangular cavity.

Table 4.2 Measured resonant frequencies f_0 and unloaded quality factors Q_0 of the three cavities. The corresponding uncertainties are denoted by σ .

Cavity	f_0 [MHz]	$\sigma(f_0)_{\text{stat}}$ [kHz]	$\sigma(f_0)_{\text{sys}}$ [kHz]	Q_0	$\sigma(Q_0)$
Circular	682.770 63	0.08	0.68	14 845	62
Rectangular	685.577 40	0.18	0.69	5815	24
Elliptic	679.507 02	0.17	0.68	6136	26

The resonant frequencies and quality factors of the three cavities are compiled in table 4.2. Note that all the three resonant frequencies are slightly off the simulated ones, which can be attributed to the perturbation by the loop couplers. The quality factor of the circular cavity is more than twice larger

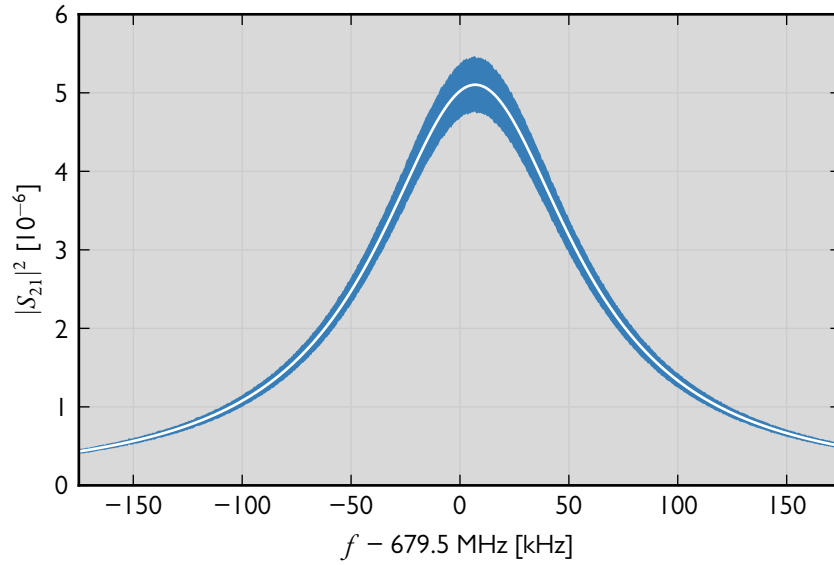


Figure 4.10 Similar to fig. 4.8, for the elliptic cavity.

than those of the other two, because the EM fields are better confined inside.

4.3.3 Drift of Resonant Frequency

It is worth noting in table 4.2 that the measurement technique is so sensitive that less than one kilohertz difference can be distinguished out of more than half a gigahertz. Since the cavities are exposed to a regular environment and no particular measures of temperature control are applied, it is of practical importance to investigate the effect of the ambient temperature on the cavities. As a result, the resonant frequency of the circular cavity and the ambient temperature have been monitored continually for about 54 h. The plots of them versus the duration are presented in fig. 4.11.

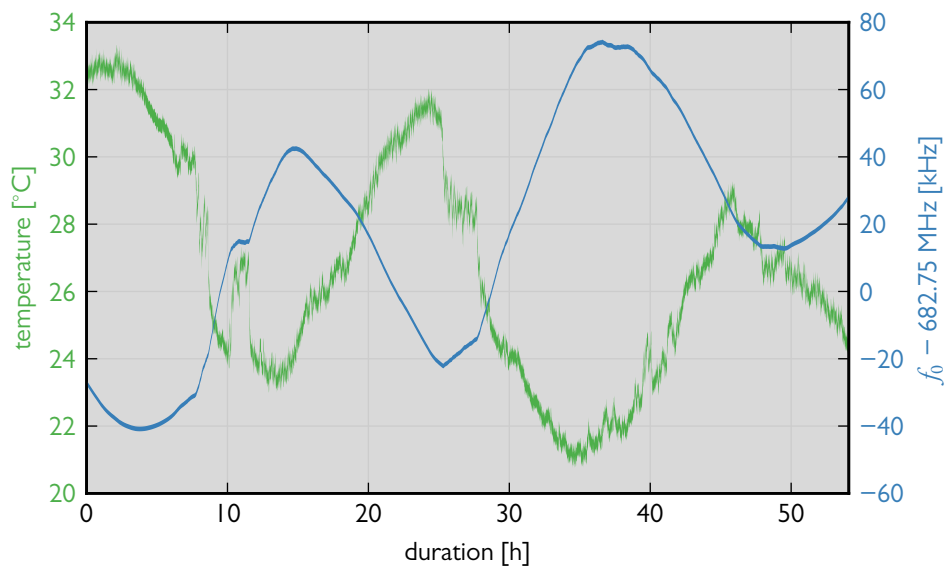


Figure 4.11 Drifts of the ambient temperature and the resonant frequency of the circular cavity during a long period. The widths of the curves represent their associated uncertainties, which is ± 0.2 °C for the temperature, and obtained from the fitting for the frequency.

A strong correlation between the resonant frequency and ambient temperature can clearly be spotted in fig. 4.11. This can be explained by the thermal expansion of the material. When the environment becomes warmer, the cavity walls stretch longer, which enlarges the inner volume. Since the resonant frequency is, in general, inversely proportional to the cavity dimensions, it gets lower. It is important to note that any material requires a response time to adapt to a new temperature. Consequently, the blue curve in fig. 4.11 is much smoother than the green one, and lags by nearly one hour. Besides, the fact that a temperature burst at the tenth hour only causes a short plateau in the blue curve can also be attributed to this reason.

A little quantitative comparison has been performed as well between the frequency shift and temperature drift. Taking the period from 25 h to 35 h as an example, the frequency shifts about 95 kHz while the temperature drifts about 10 °C. The relative change of the resonant frequency is

$$\frac{95 \text{ kHz}}{682.75 \text{ MHz}} = 1.39 \times 10^{-4}. \quad (4.9)$$

According to the material datasheet, the thermal linear expansion coefficient is $23.4 \times 10^{-6} \text{ }^\circ\text{C}^{-1}$ at room temperature, which leads to the relative change of the cavity radius:

$$(23.4 \times 10^{-6} \text{ }^\circ\text{C}^{-1}) \times 10 \text{ }^\circ\text{C} = 2.34 \times 10^{-4}. \quad (4.10)$$

The two quantities are of the same order of magnitude. The small difference may be due to the response time of the material. The feature of the cavity being sensitive to the ambient temperature necessitates a counteract in the dynamic test, since it usually lasts for several hours.

4.3.4 Determination of Relative Permittivity

For the perturbation measurements, a ceramic bead with a diameter of 5 mm is adopted as the perturbing object. The bead is bored through the center with a small hole, and pierced by a cotton thread with a knot at an end (fig. 4.12). It is then placed inside the circular cavity across the top hole, followed

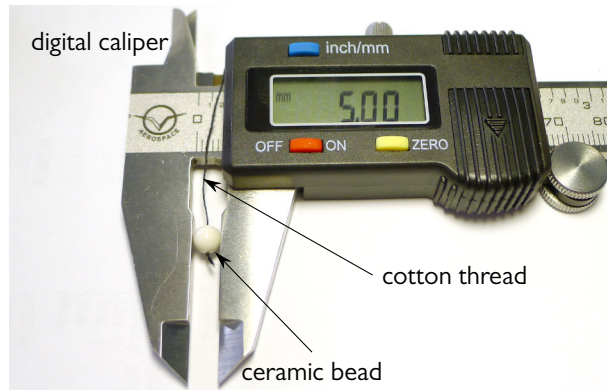


Figure 4.12 Closeup of the ceramic bead demonstrating its size in millimeter.

by blocking the hole with a screw. The rather low relative permittivity of the cotton (around two) makes it quite suitable for suspending the bead in the air, such that the detuning frequency is mainly caused by the bead. To ensure that the bead is in the center of the cavity, the hole has intentionally been offset from the center by its radius, and the inner length of the thread is adjusted to 5 cm.

The relative permittivity of the bead is determined from the detuning frequency based on eq. (2.21). To simplify the calculation, it is better to reformulate eq. (2.21) to

$$\frac{\partial f}{f_0} = -\frac{\alpha_b \mathbf{E}^2}{W}, \quad (4.11)$$

where

$$\alpha_b = \frac{\pi \varepsilon_0 (\varepsilon_r - 1) r_b^3}{\varepsilon_r + 2} \quad (4.12)$$

is the *form factor* that only depends on the bead. The electric field \mathbf{E} at the location of the bead, and the total EM energy \mathcal{W} in eq. (4.11) can be developed by virtue of eqs. (2.17) and (A.56). In the course of the derivation, the indefinite integral equation

$$\int dx x J_0^2(ax) = \frac{x^2}{2} [J_0^2(ax) + J_1^2(ax)] \quad (4.13)$$

will be helpful. Here, J_0 and J_1 are the Bessel functions of order zero and one, respectively.

In the end, the form factor can be computed via

$$\alpha_b = -\frac{\pi \varepsilon_0 J_1^2(j_{01}) a^2 d \delta f}{2 f_0}, \quad (4.14)$$

where j_{01} is the first root of J_0 , a is the radius of the cavity, and d is the depth of the cavity. Besides, δf is the detuning frequency and f_0 is the reference frequency without the perturbation. The comparison between the two separate transmission measurements before and after the bead is placed inside the cavity is presented in fig. 4.13. The reference frequency f_0 is 682.775 87(8)(68) MHz, while the detuned

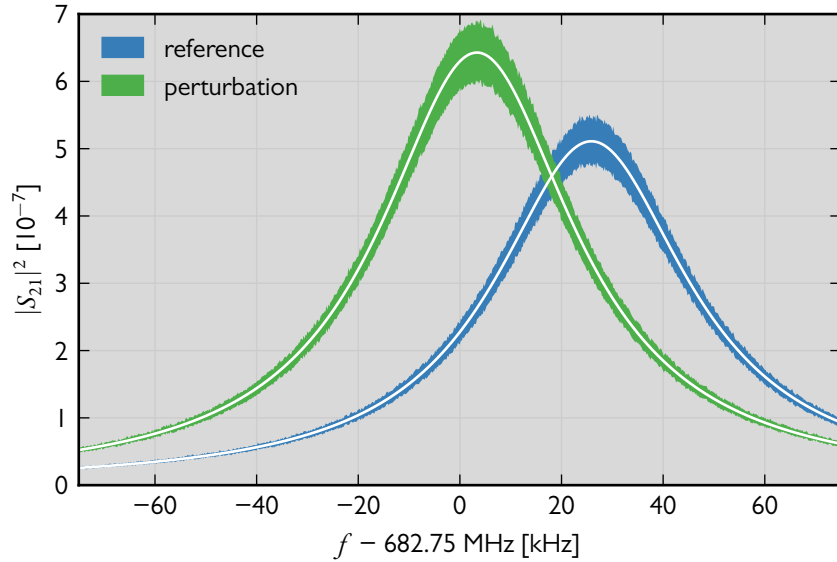


Figure 4.13 Transmission measurements of the circular cavity before and after the perturbation by the ceramic bead. The measured data together with the associated uncertainties are represented by filled areas. The fitted Lorentzian functions are shown with white curves.

frequency f is 682.753 35(7)(68) MHz. The form factor is obtained accordingly:

$$\alpha_b = 3.489(17) \times 10^{-19} \text{ F} \cdot \text{m}^{-2}. \quad (4.15)$$

The uncertainty of the radius a and the depth d of the circular cavity is estimated to be 0.02 mm based on the manufacture precision. Note that only the statistic uncertainties of f_0 and f propagate into δf , since the systematic ones are canceled out by the subtraction.

Subsequently, the relative permittivity of the bead is calculated by inverting eq. (4.12):

$$\varepsilon_r = \frac{\pi \varepsilon_0 r_b^3 + 2\alpha_b}{\pi \varepsilon_0 r_b^3 - \alpha_b}. \quad (4.16)$$

The result is 13.2(8), where the uncertainty of the bead radius is estimated to be 0.01 mm.

4.3.5 Detuning by Plungers

To investigate the detuning effect of the plungers, the transmission coefficients are measured for both cavities, while the plungers are manually turned stepwise with a step of 1 mm. The position of the plungers x_{pl} ranges from -5 mm to 5 mm, where the negative value means that the plungers are inside the cavity. The resonant frequency of the cavity at each step is obtained afterwards via a parametric fitting. The results are shown in figs. 4.14 and 4.15 for the rectangular and elliptic cavity, respectively.

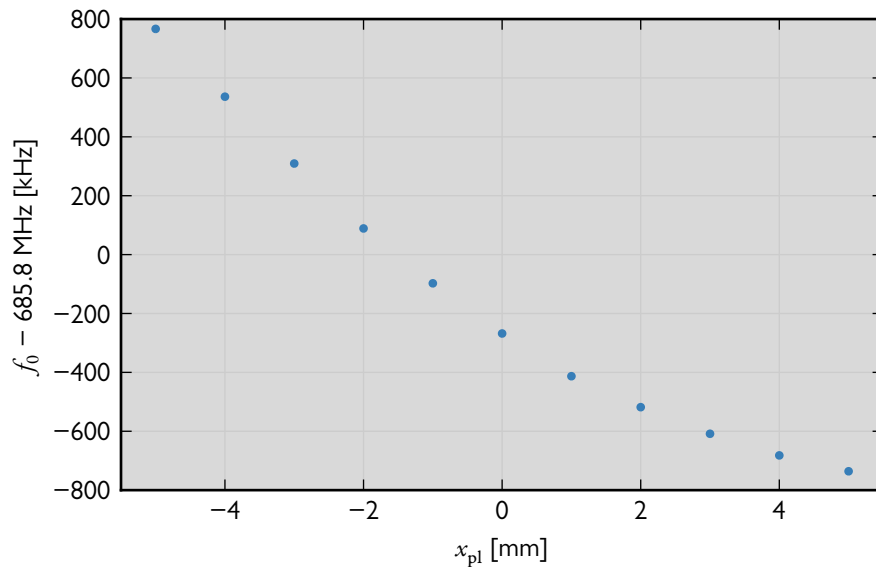


Figure 4.14 Detuned frequency of the rectangular cavity as a function of the plunger position. The negative position means that the plungers are inside the cavity. The uncertainty is invisible, since it is smaller than the marker size.

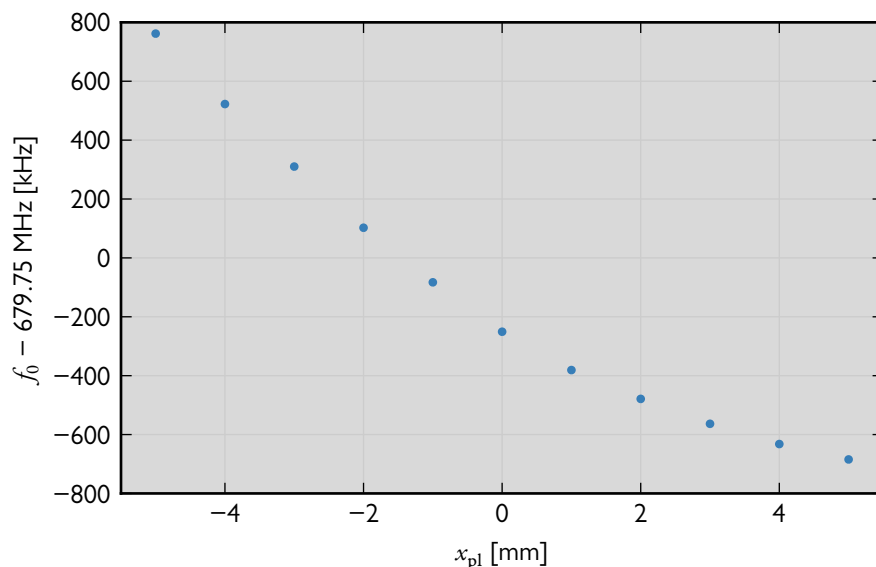


Figure 4.15 Similar to fig. 4.14, for the elliptic cavity.

It is interesting to note in figs. 4.14 and 4.15 that both cavities exhibit nearly the same tunable range. However, the elliptic cavity manifests a slightly higher relative detuning due to its lower resonant frequency.

4.3.6 Damping of Higher-Order Modes

The parasitic higher-order modes can be damped by probe couplers terminated by 50Ω resistances. Similar to the loop coupler, the probe coupler is also based on a BNC connector soldered with a silver wire on top of it (fig. 4.5). There are in all four of them mounted on the front face of either the rectangular or the elliptic cavity for test. The frequency spans of the transmission measurements are now extended to accommodate the first three resonances for both cavities. The number of trace points is also increased to 1601.

The comparison between the S_{21} 's before and after the damping couplers are mounted on the rectangular cavity is presented in fig. 4.16. It is clear in fig. 4.16 that all the modes are affected though,

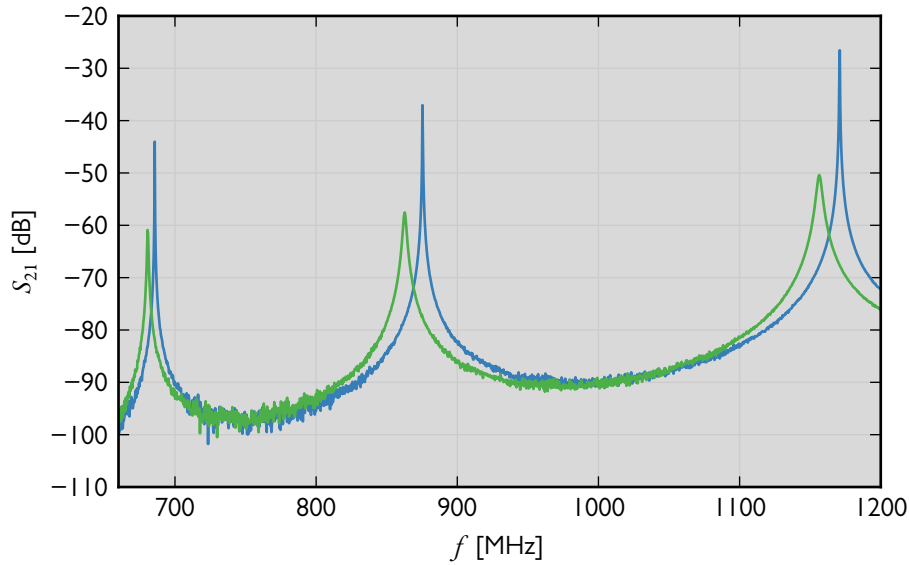


Figure 4.16 Transmission curves of the rectangular cavity containing the first three resonances. The blue one is measured before the damping couplers for the Higher-Order Modes (HOMs) are mounted to the cavity, while the green one is measured after that. The uncertainty is invisible, since it is smaller than the line width.

the dipole and tripole mode are much more damped by the couplers. Meanwhile, their resonance frequencies and quality factors become smaller also due to the influence of the couplers. The quantitative comparison about the resonant frequencies and signal strengths on resonance is tabulated in table 4.3.

Table 4.3 Comparison about the first three resonances of the rectangular cavity before and after the damping couplers for the Higher-Order Modes (HOMs) are mounted.

Eigenmode	Without damping		With damping		Difference	
	f_0 [MHz]	S_{21} [dB]	f_0 [MHz]	S_{21} [dB]	Δf_0 [MHz]	ΔS_{21} [dB]
Monopole	685.65	-44.0	680.59	-60.9	-5.06	-16.9
Dipole	875.33	-37.0	862.84	-57.6	-12.49	-20.6
Tripole	1170.98	-26.7	1156.46	-50.4	-14.52	-23.7

Likewise, the transmission curves of the elliptic cavity before and after the damping couplers are mounted is presented in fig. 4.17. The resonant frequencies and signal strengths of the first three modes in the elliptic cavity are listed in table 4.4.

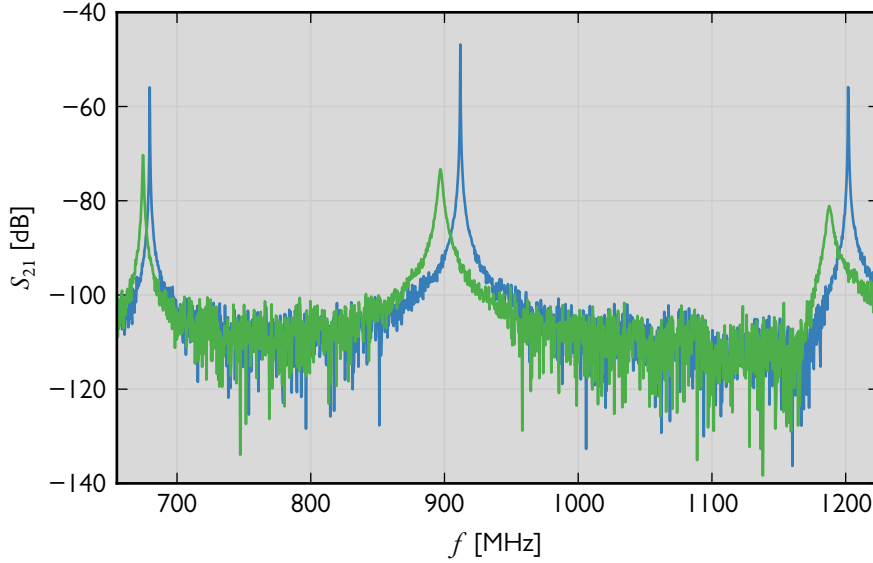


Figure 4.17 Similar to fig. 4.16, for the elliptic cavity.

Table 4.4 Similar to table 4.3, for the elliptic cavity.

Eigenmode	Without damping		With damping		Difference	
	f_0 [MHz]	S_{21} [dB]	f_0 [MHz]	S_{21} [dB]	Δf_0 [MHz]	ΔS_{21} [dB]
Monopole	679.58	-55.9	674.59	-70.3	-4.99	-14.4
Dipole	911.86	-46.9	896.89	-73.3	-14.97	-26.4
Tripole	1201.84	-55.9	1187.59	-81.1	-14.25	-25.2

4.4 Dynamic Test

During the dynamic test, the electric field inside the beam pipe is profiled by placing the ceramic bead at various sample positions for each cavity. Afterwards, the shunt impedance in the aperture region is accordingly computed.

Usually the cavity under test is seated at a fixed position, while the bead is pulled by a stepper motor via pulleys. As a result, this method is known as the bead-pull perturbation. However, the method suffers from the stretch problem of the supporting thread for the bead, which causes the bead vibrating during the movement and may introduce positioning errors. To circumvent this issue, a different scheme is adopted in the present dynamic test, where the bead is fixed and the cavity is moved instead.

4.4.1 Test Bench Setup

The setup of the test bench is pictured in fig. 4.18, together with an associated Cartesian coordinate system. Note that the origin of the system is actually in the center of the beam pipe, but translated in fig. 4.18 only for a better visibility. In addition to all the devices that are used before, several new equipments are incorporated in the dynamic test. First of all, a motorized displacement unit (isel LES series) is employed to bear the cavity under test to various positions. It consists of two linear actuators lying orthogonally in the horizontal plane, as well as two auxiliary passive supports. The unit was shipped with a motor controller (isel iMC-S8), which is capable of remote control. However, it only provides a serial port for communication. As a result, a serial-Ethernet converter bridges the PC and motor controller to translate commands. The VNA is seated on the same actuator as the cavity is, such

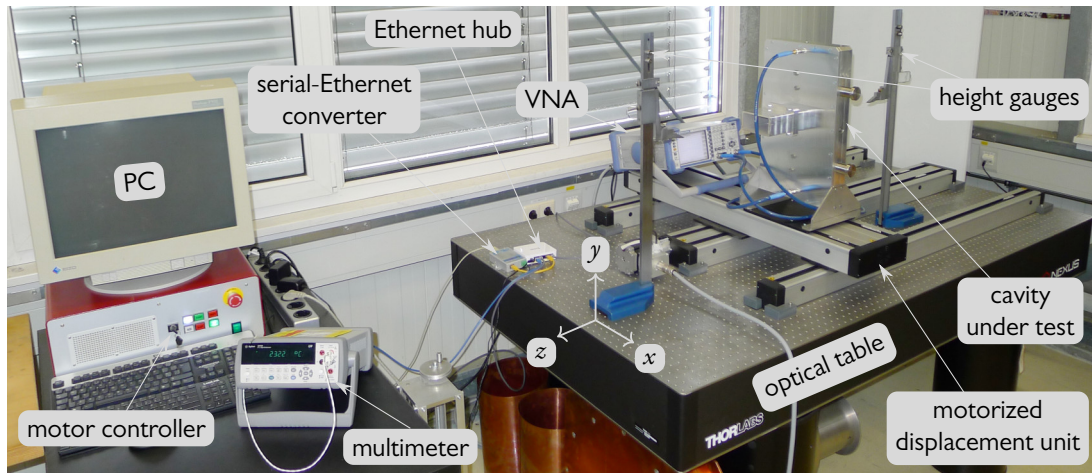


Figure 4.18 Setup of the dynamic test bench. The origin of the Cartesian coordinate system is in the center of the beam pipe, but translated in the photograph for a better visibility. The orientation of the coordinates follows the convention in the accelerator community. All the devices in fig. 4.4 are retained. The cavity is borne by the motorized displacement unit to various positions in the horizontal plane. The height gauges support the ceramic bead via a cotton thread, and also allow for fine adjustments in the vertical direction. See the text for more details.

that it co-moves with the cavity in the z direction to reduce the stretch of the microwave cables. A cotton thread with the ceramic bead is crossed through the beam pipe and fastened on two height gauges (Vogel 341116) on either side of the cavity (fig. 4.19). Apart from being a holder for the thread, the

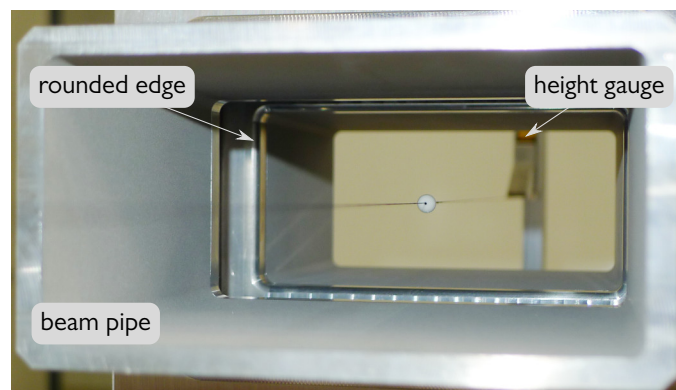


Figure 4.19 Closeup of the ceramic bead placed in the center of the beam pipe. It is supported by a pair of height gauges via a cotton thread crossing through the center of the bead. The captured height gauge is on the far side of the camera, while the other one stands behind. The rounded edges of the apertures are also visible in the photograph.

height gauge also allows for a precise adjustment in the y direction with its vernier scale. Finally, an optical table (Thorlabs T1220C) with a feature of passive vibration damping serves as a stable base for the movement system.

The Java application has correspondingly been adapted. Its main improvement is the ability to efficiently coordinate the movement-measurement cycles. In the present test, the motorized unit displaces the cavity to a predefined position at a speed of $5 \text{ cm} \cdot \text{s}^{-1}$. Then, the application pauses for 0.1 s for re-establishing stable EM fields inside the cavity, and damping, although least likely, the vibration of the bead due to the cavity movement. Afterwards, the VNA and multimeter perform ten consecutive measurements, average results, and transfer them back to the PC. After the data have been written to a text

file, the PC initiates another cycle. It is worth noting that the positioning uncertainty of the motorized unit is negligible, as this has been proven by a long-term test run, where the cavity exactly returned to the starting point after 100 times of repetitive two-dimensional movements.

4.4.2 Profiling Detuned Frequency

The detuned frequency in the beam pipe is profiled with the ceramic bead in the horizontal central plane. The profiling area is 27 cm by 9 cm that covers the entire horizontal extent of the beam pipe. The area is first meshed into a grid with a spacing of 5 mm in either direction, which is the same as the diameter of the bead. Then, the cavity is displaced in an x -major order to traverse all the grid nodes. That is to say, the cavity subsequently goes through all the points with the same x -coordinate till it advances to the next one. Afterwards, the detuned frequency of the cavity is extracted from the S_{21} measurement for each position.

The profiled frequency map of the rectangular cavity is visualized in fig. 4.20. It is apparent in

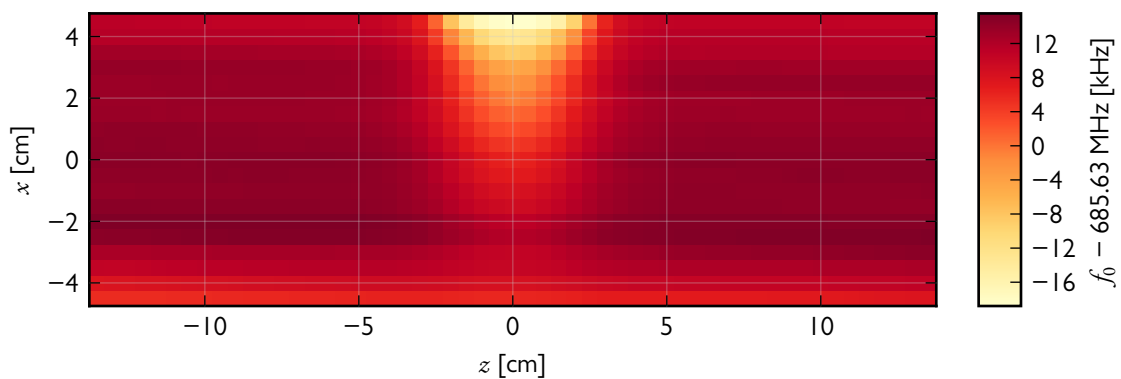


Figure 4.20 Detuned frequency map of the rectangular cavity in the whole beam pipe at $y = 0$. The coordinates are the same as those shown in fig. 4.18. The cavity gap is between $z = \pm 2$ cm.

fig. 4.20 that the detuning is prominent in the top central region, which is close to the cavity center. This agrees with the expectation, since the electric field mostly concentrates there. It is also noticeable in fig. 4.20 that the resonant frequency is still detuned even outside the cavity gap, which is between $z = \pm 2$ cm. This can be attributed to the extension of the electric field into the beam pipe. The frequency tends to be constant towards both ends of the beam pipe, but exhibits a variation in the x direction. This is due to the thermal effect, since the complete profiling process lasts for more than five hours. A similar map for the elliptic cavity is visualized in fig. 4.21, where the thermal effect is more prominent.

Due to the influence of the ambient temperature, a single reference measurement without the perturbation is clearly no longer adequate for accurately deducing the profile of the electric field. It is thus proposed to adopt a multi-reference scheme to correct for this parasitic effect. Specifically, a reference measurement at the location of an insignificant electric field will be performed prior to each perturbation measurement in the region of interest. The insignificance of the electric field can be indicated by the invariance of the detuned frequency in the z direction. To this end, the topmost slice of the detuned frequency map in figs. 4.20 and 4.21, where the electric field extends the furthest into the beam pipe, is focused on to define the practical borders of the field. Their corresponding plots are shown in figs. 4.22 and 4.23.

Based on figs. 4.22 and 4.23, an interval from -5.5 cm to 5.5 cm in the z direction is visually selected for the perturbation measurements. The reference position is selected to be even further away from the middle to prepare for contingencies. In fact, two symmetric reference positions at $z = \pm 10$ cm

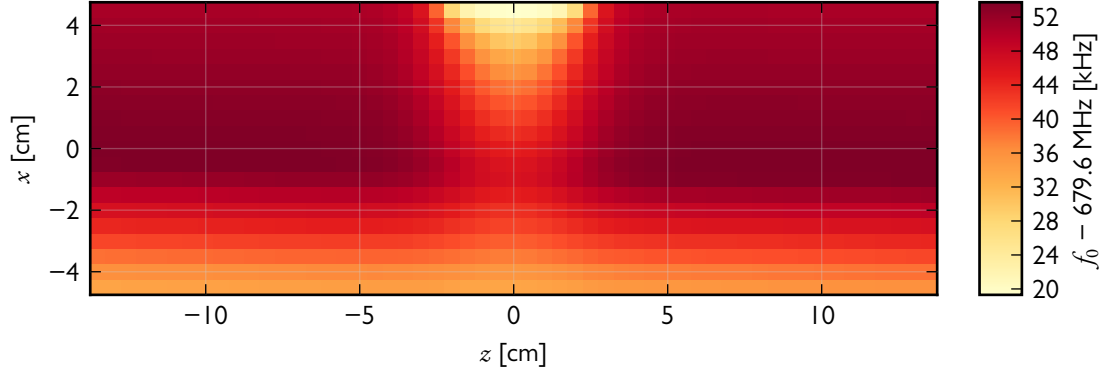


Figure 4.21 Similar to fig. 4.20, for the elliptic cavity.

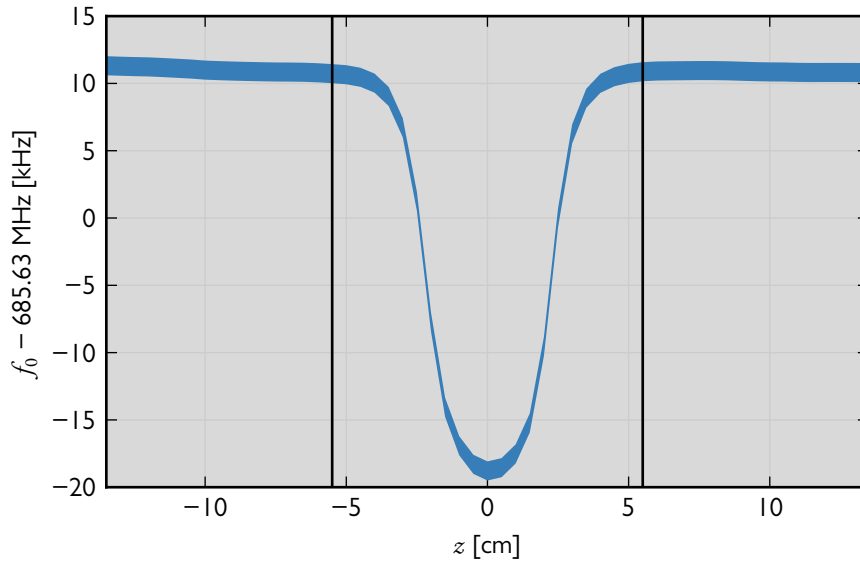


Figure 4.22 Detuned frequency of the rectangular cavity as a function of z , where $x = 4.5$ cm and $y = 0$. The coordinates are the same as those shown in fig. 4.18. The width of the curve represents the associated uncertainty. The pair of vertical lines at $z = \pm 5.5$ cm indicate the profiling range in the z direction for the perturbation measurements.

are nominated, out of which the nearer one to the current position is chosen for each perturbation measurement to save the total profiling time.

4.4.3 Profiling Electric Field

Likewise, the electric field is profiled on a grid of 11 cm by 9 cm with a spacing of 5 mm in either direction. A perturbation measurement and its corresponding reference measurement are performed for all the grid nodes in an x -major order. Then, the profiling plane is translated in the y direction, and the whole process is repeated. In all, nine planes from -2 cm to 2 cm with a spacing of 5 mm are traversed to cover the vertical extent of the beam pipe.

For the calculation of the electric field from the detuned frequency, it is convenient to reformulate eq. (2.37) to

$$\frac{R_{\text{sh}}}{Q_0} = \left(\int_{-d/2}^{d/2} dz \frac{E_z}{\sqrt{\omega_0 W}} \right)^2, \quad (4.17)$$

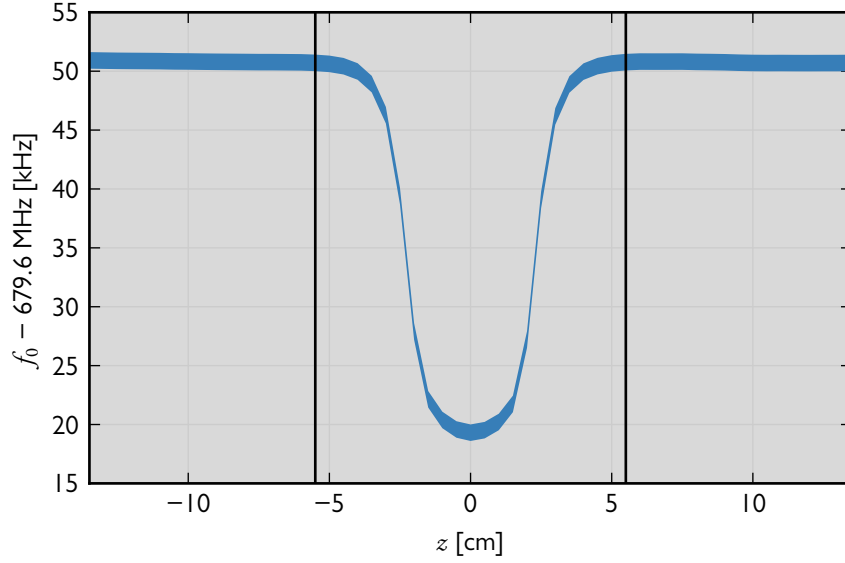


Figure 4.23 Similar to fig. 4.22, for the elliptic cavity.

where the integrand $E_z/\sqrt{\omega_0 W}$ is the *normalized electric field*, and the integral range should now be replaced with the profiling interval in the z direction. By virtue of eq. (4.11), it is related to the detuning frequency via

$$\frac{E_z}{\sqrt{\omega_0 W}} = \sqrt{\frac{-\delta f}{2\pi\alpha_b f_0^2}}, \quad (4.18)$$

provided that the electric field \mathbf{E} only has a z -component E_z .

In reality, the detuning frequency δf is not guaranteed to be negative semidefinite, i.e. the detuned frequency f may become even larger than the reference frequency f_0 due to the statistical fluctuation in the measurement. This is most likely to happen for the perturbation measurement with a very weak electric field. Therefore, the raw data need some polish before substituting into eq. (4.18), otherwise it will lead to nonphysical results. In order to neutralize the singularities, the detuning frequency is artificially assigned to zero if its absolute value is no greater than its uncertainty. The physical interpretation is that the detuning frequency is negligible within the resolution of the measuring system.

After the polish, the resultant maps of the normalized electric fields in the horizontal central planes are visualized in figs. 4.24 and 4.25 for the rectangular and elliptic cavity. The field maps in other planes present a similarity to figs. 4.24 and 4.25. By means of perturbation, it is finally possible to see the gradual variation of the electric field in the beam pipe, which is in good agreement with the expectation.

4.4.4 Profiling Shunt Impedance

Having profiled the electric field, the shunt impedance is straightforward to obtain by integrating the normalized electric field along the z -axis according to eq. (4.17). The integral is numerically approximated based on the mid-ordinate rule. The measured shunt impedances in the horizontal central planes are plotted in figs. 4.26 and 4.27 for the rectangular and elliptic cavity. The ascending trend in figs. 4.26 and 4.27 ensures the position-resolving abilities of both cavities. The rather high characteristic shunt impedance around the middle also reflects the intensity sensitivity for both cavities.

Three representative R_{sh}/Q_0 's at the left end, in the middle, and at the right end are listed in table 4.5 for the rectangular and elliptic cavity. By comparing the values in table 4.5 with those in tables 3.3

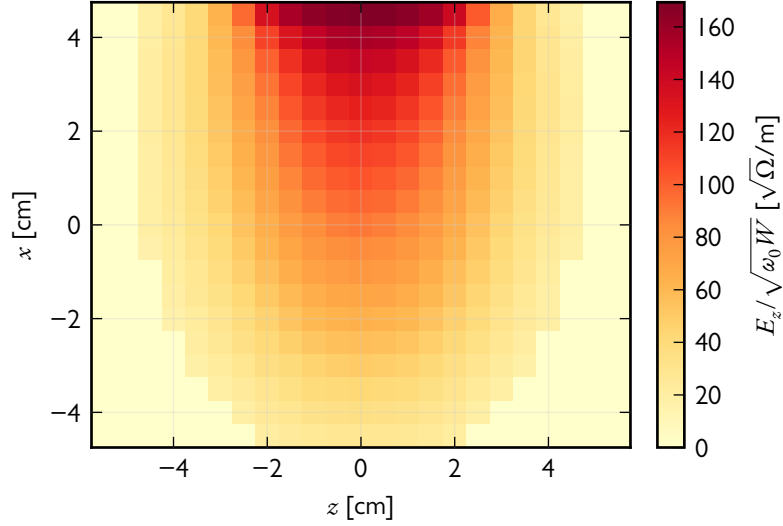


Figure 4.24 Normalized electric field of the rectangular cavity in the beam pipe at $y = 0$. The coordinates are the same as those shown in fig. 4.18.

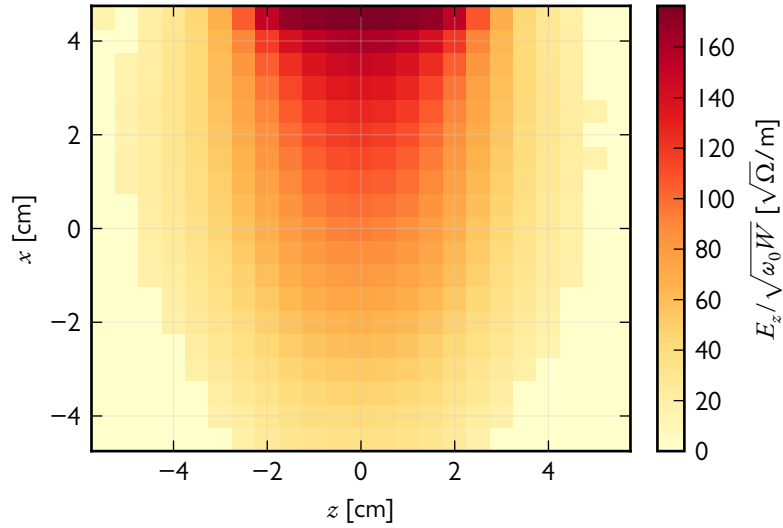


Figure 4.25 Similar to fig. 4.24, for the elliptic cavity.

Table 4.5 Characteristic shunt impedances at the left end, in the middle, and at the right end of the beam pipe for the rectangular and elliptic cavity. The corresponding uncertainties are denoted by σ .

Location	Rectangular		Elliptic	
	R_{sh}/Q_0 [Ω]	$\sigma(R_{\text{sh}}/Q_0)$ [Ω]	R_{sh}/Q_0 [Ω]	$\sigma(R_{\text{sh}}/Q_0)$ [Ω]
Left	1.30	0.17	2.47	0.25
Middle	29.11	0.79	30.44	0.79
Right	93.04	1.25	106.48	1.49

and 3.4, it is found that the measured ones in general exhibit a little deficiency except at the right end, where the values are suspiciously excessive. This anomalous phenomenon is also observed in other horizontal planes, as shown in the shunt impedance maps in figs. 4.28 and 4.29 for the rectangular and

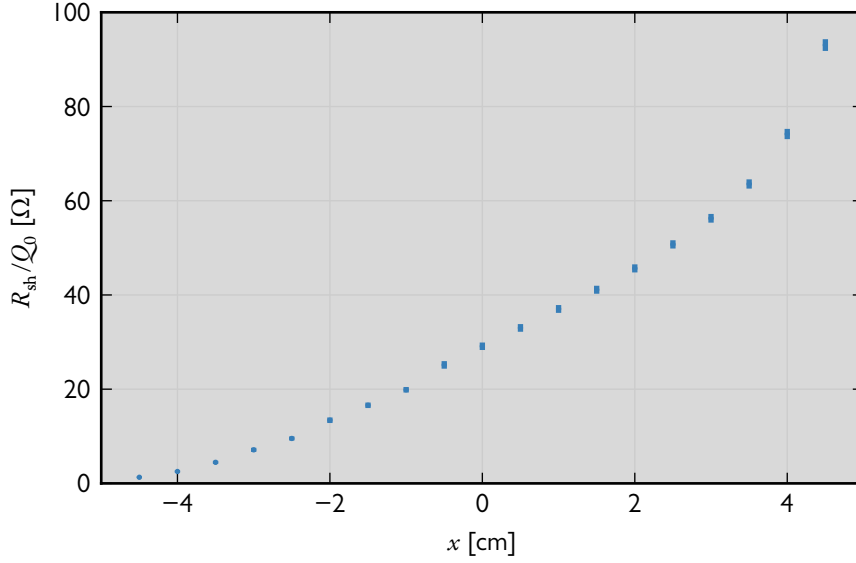


Figure 4.26 Characteristic shunt impedance of the rectangular cavity as a function of x at $y = 0$. The coordinates are the same as those shown in fig. 4.18. The length of each bar represents the associated uncertainty.

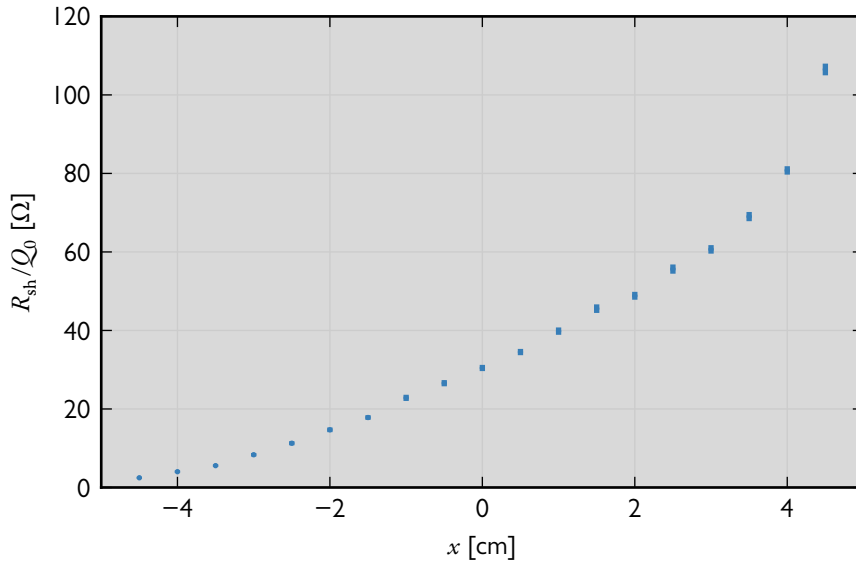


Figure 4.27 Similar to fig. 4.26, for the elliptic cavity.

elliptic cavity, respectively. It is interesting to note in figs. 4.28 and 4.29 that the shunt impedance seems enhanced as well at the top and on the bottom. In fact, this apparent enhancement is an artifact of the perturbation method.

First of all, at the locations of the anomalies the ceramic bead is very close (around 3 mm) to the walls of the beam pipes. Therefore, the image charge effect has to be accounted for, which is embodied in a correction term χ to be added to eq. (4.18) when calculating the normalized electric field [152]:

$$\frac{E_z}{\sqrt{\omega_0 W}} = \sqrt{\frac{-\delta f}{2\pi(1 + \chi)\alpha_b f_0^2}}, \quad (4.19)$$

where χ is a polynomial of the ratio between the bead radius r_b and twice the distance from the bead

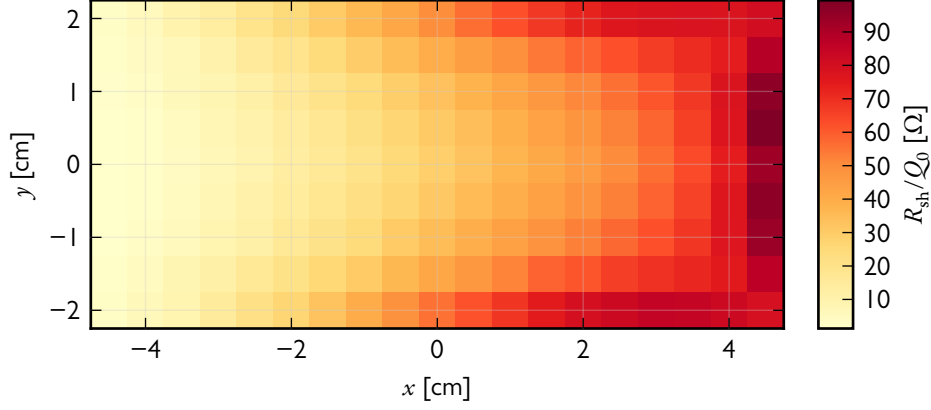


Figure 4.28 Shunt impedance map of the rectangular cavity in the aperture region. The coordinates are the same as those shown in fig. 4.18.

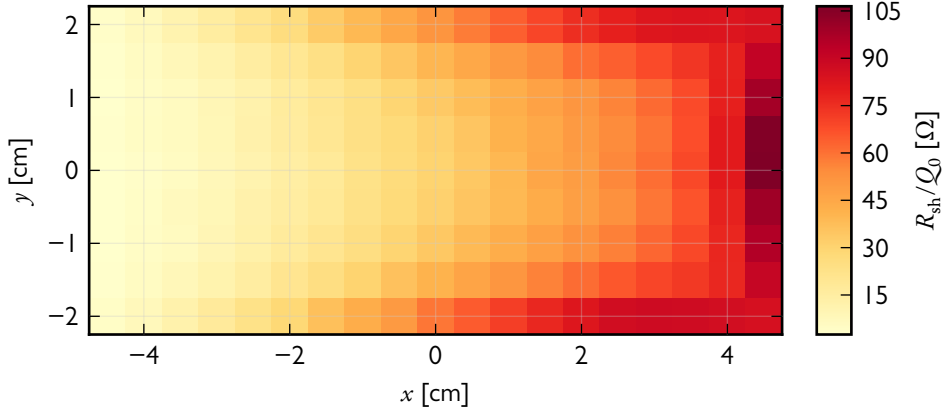


Figure 4.29 Similar to fig. 4.28, for the elliptic cavity.

center to the wall l_b . It is given as

$$\chi \left(\frac{r_b}{2l_b} \right) = \frac{4(\varepsilon_r - 1)}{\varepsilon_r + 2} \left(\frac{r_b}{2l_b} \right)^3 + \frac{16(\varepsilon_r - 1)^2}{(\varepsilon_r + 2)^2} \left(\frac{r_b}{2l_b} \right)^6 + \frac{144(\varepsilon_r - 1)^2}{(2\varepsilon_r + 3)(\varepsilon_r + 2)} \left(\frac{r_b}{2l_b} \right)^8. \quad (4.20)$$

In fact, the sum of four variants of eq. (4.20) should be substituted into eq. (4.19) in order to take into account all the image charges in the four cardinal directions. The correction is then applied to the perturbation measurements outside the cavity gap, and the corrected shunt impedance map is visualized in figs. 4.30 and 4.31 for the rectangular and elliptic cavity, respectively.

A visual comparison among figs. 4.28 to 4.31 immediately suggests that the image charge effect is just a minor cause for the anomaly. In fact, the latter is mainly due to the incapability of distinguishing the field orientation with the ceramic bead. The spherical symmetry of the bead results in its isotropic form factor, i.e. α_b is independent of the orientation of \mathbf{E} . Therefore, according to eq. (4.11), the detuning frequency is determined by the total electric field strength. However, only the z -component of the electric field is substituted into eq. (2.37) to compute the characteristic shunt impedance. If the electric field lies off the z direction, the shunt impedance is then overestimated by using eqs. (4.17) and (4.18).

This speculation is endorsed by the simulation. The simulated electric field orientation inside the beam pipe of the rectangular cavity is depicted in figs. 4.32 and 4.33 for the horizontal and vertical central plane, respectively. The plots for the elliptic cavity are very similar to these figures, and thus

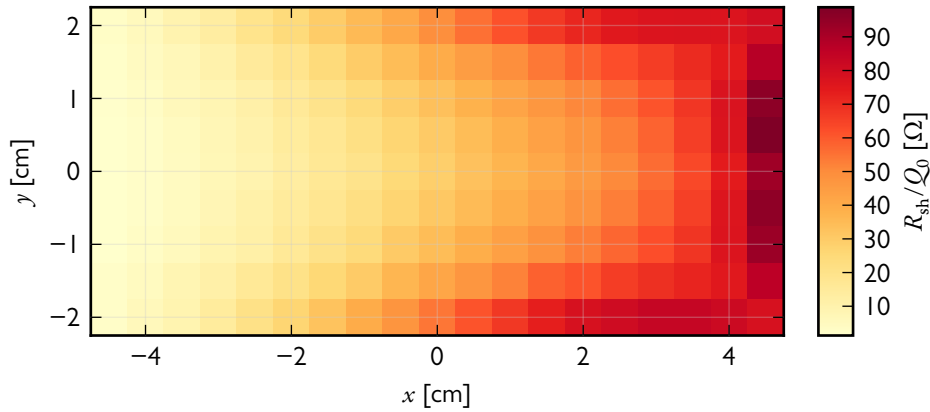


Figure 4.30 Shunt impedance map of the rectangular cavity in the aperture region, after the correction for the image charge effect is applied (cf. fig. 4.28). The coordinates are the same as those shown in fig. 4.18.

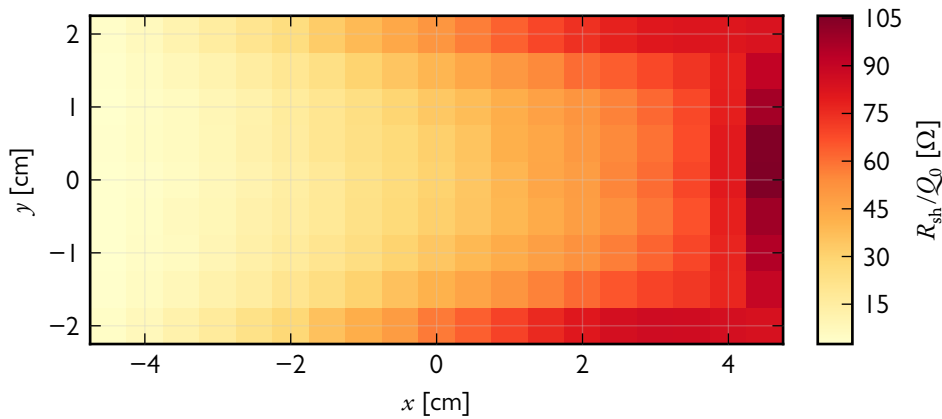


Figure 4.31 Similar to fig. 4.30, for the elliptic cavity (cf. fig. 4.29).

omitted for brevity. It is clear in figs. 4.32 and 4.33 that the electric field deviates from the z direction in the vicinity of apertures, which unravels the puzzle in figs. 4.28 and 4.29.

The blindness to the field orientation can be surpassed by breaking the spherical symmetry via adopting an asymmetric geometry and/or an anisotropic material. As a generalization of the sphere, the ellipsoid presents a triaxial form factor, which perturbs the electric field variously at different orientations [153]. Note that two shapes of practically available objects—needle and disk—can be reckoned special cases of the ellipsoid, i.e. the prolate and oblate spheroid [154]. The orientation of the electric field can also be distinguished by an anisotropic dielectric material, even if it is in the shape of a sphere. Furthermore, an ellipsoid with an anisotropic permittivity can, although less practical, be used to profile the electric field in both magnitude and orientation [155].

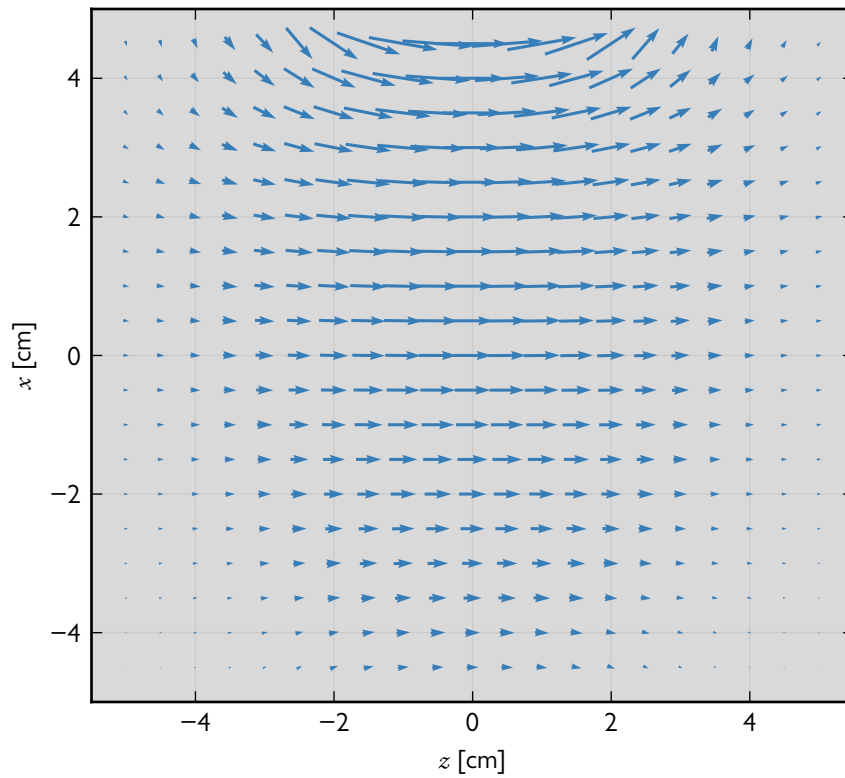


Figure 4.32 Simulated electric field orientation of the rectangular cavity in the beam pipe at $y = 0$. The coordinates are the same as those shown in fig. 4.18. The arrow length is proportional to the field strength, while the arrow head points to the field orientation. The cavity gap is between $z = \pm 2$ cm.

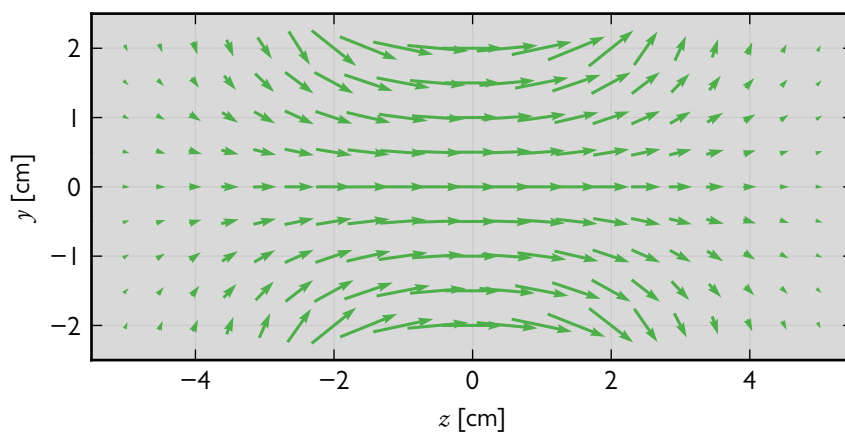


Figure 4.33 Similar to fig. 4.32, at $x = 0$.

5 CONCLUSION



Since the commissioning of the ESR in 1990, the research in nuclear physics has benefited from heavy-ion storage rings for the last few decades. Due to the ultra-high vacuum in the ring, a broad range of short-lived exotic nuclei close to the nucleon drip-lines in high atomic charge states could be stored for a sufficiently long time. Consequently, a set of sophisticated spectroscopic techniques could be applied to the stored ions for the systematic investigations on their fundamental properties, e.g. masses and lifetimes, in the ground and isomeric states. In particular, the Schottky spectroscopy in the isochronous mode—a study on the Schottky noise of the stored beam while the ion optics of the ring is set to isochronism—by means of an intensity-sensitive and time-resolving RF cavity enables the simultaneous measurements of masses and lifetimes of short-lived nuclei in the subsecond regime.

However, due to the large momentum acceptance of the ring, the isochronism condition cannot be fulfilled for every species of the stored ions. In order to correct for this anisochronism effect, it is proposed to additionally employ a position-resolving cavity adjacent to the existing one at the dispersive location to help distinguish the revolution orbit of each ion along with the measurement of its revolution frequency. Through the theoretical description on the detection principle of an RF cavity as well as the Schottky power spectral density of a coasting beam presented in chapter 2, it is concluded that the coupled signal strength of the beam is proportional to the characteristic shunt impedance of the cavity. The variance of the shunt impedance within the aperture region reflects the position-resolving ability of the cavity. By normalizing the signal strength from the position cavity with respect to that from the intensity cavity, the horizontal position of an ion can thus be inferred. The correction method for the anisochronism effect with the extra position information is then outlined in section 2.5. Briefly, a common reference orbit is appointed in the first place for all the ions of different species. After the relation between the revolution frequency and horizontal position is attained for each species, the representative frequencies can be deduced as if all the ions are on the reference orbit. Then, the evaluated nuclear masses based on the representative frequencies are intrinsically free of the anisochronism effect.

Unlike the conventional position cavity that employs the dipole mode to produce a horizontally variant shunt impedance distribution, an innovative design that exploits the monopole mode and offsets the cavity away from the central orbit is explored in chapter 3. This configuration can achieve a quite amount of shunt impedance in the aperture region, while the distribution still exhibits an inclined trend from one end to the other, which significantly improves the signal-to-noise ratio, and thus is especially advantageous for the exotic nuclei with low yields. The design specifications of the cavity are assessed according to the machine parameters of the CR in three isochronous modes, and in accordance with the technical requirements assigned by the ILIMA collaboration. In order to minimize the crosstalk between the two transverse directions, the height and width of the position cavity are intentionally deviated from each other, which has inspired two variants of the cavity, namely the rectangular and elliptic cavity. The optimization of the design is performed on both of them. First, the dimensions of the cavity are selected by virtue of the dependence graph in figs. 3.7 and 3.11 for the rectangular and elliptic cavity, respectively. Then, the computational approach takes over to account for the apertures

with beam pipes, the higher-order modes, and the detuning by plungers. Based on the simulation, it is important to round the edges of the apertures in order to attain a gradually ascending shunt impedance from left to right in the aperture region. The simulated shunt impedance maps for the rectangular and elliptic cavity are presented in figs. 3.17 and 3.18, respectively.

After the designs of the two cavities have been finalized, a scaled prototype is manufactured accordingly for each of them to justify the design concept. Moreover, a circular pillbox cavity is constructed to calibrate the relative permittivity of a ceramic bead, which is the key to the profiling of the electric field by perturbation. The details about the static and dynamic test on both prototype cavities as well as the calibration cavity is thoroughly documented in chapter 4. The static test bench (fig. 4.4) consists of a VNA for the measurements of S -parameters, a multimeter with a thermistor for the monitoring of the ambient temperature, and a PC running a dedicated Java application for the coordination of the whole test process. It is of practical importance to note that the measurement technique is so sensitive that the effect of the temperature drift actually needs to be corrected for. The detuning by the plungers and the damping of the higher-order modes by the probe couplers are also demonstrated in the test. In the dynamic test (fig. 4.18), in order to profile the electric fields inside the cavities, a motorized displacement unit with an associated motor controller is additionally incorporated into the setup. The ceramic bead is pierced by a cotton thread, and then attached to a pair of height gauges equipped with vernier scales, which also allow for fine adjustments in the vertical direction. The profiling region of the electric field is meshed into a grid. For each perturbation measurement at the grid node, a preceding reference measurement without perturbation is applied as well to minimize the thermal effect. The normalized electric field is then obtained from the detuning frequency, and the shunt impedance is approximated by a numerical integral of the electric field along the z -axis. The apparent shunt impedance excess near the beam pipe, after the deduction of the image charge effect, in the measurements (figs. 4.30 and 4.31) can be attributed to the artifact of the perturbation method with the ceramic bead that the orientation of the electric field is not detectable. Apart from that, the benchtop measurements are in good agreement with the computational simulations, which justifies the innovative design of a position-resolving cavity.

Since the two kinds of cavities are originally intended for being comparable, the mechanical parameters of both cavities are very alike, some of them are even identical. Nevertheless, several subtle differences do exist. The elliptic cavity is a little larger than the rectangular one, which causes a slightly lower resonant frequency. As a tradeoff, the rectangular cavity gains a bit more mass resolving power. The straighter shunt impedance contours in the rectangular cavity also lead to less crosstalk. On the other hand, the overall characteristic shunt impedance is a little higher for the elliptic cavity, which delivers slightly better intensity sensitivity. The wider spread of the first three resonances also results in less contamination in the monopole mode for the elliptic cavity. In all, both cavities are eligible for attending to the experimental duties.

The installing location for the position cavity in the CR should preferably coincide with the location of the largest momentum dispersion, which must be next to a dipole magnet in an arc section. The exact spot ought to be decided on by referring to the simulated results of the beam dynamics in the ring, and by considering the other elements nearby. The available space in the longitudinal direction should be enough to accommodate both the position and intensity cavity. In addition, it is suggested to install a pair of beam scrapers adjacent to the cavity doublet to allow for a direct calibration of the gauge function, i.e. $f_{\text{rev}} = \mathcal{G}(x)$, with a ray of ions, of which the horizontal position can precisely be controlled by the slit. This method is complementary to the benchtop measurement, but expected to deliver a more accurate result since the gauge function can directly be obtained. On the other hand, the benchtop measurement can be improved as well by adopting a dielectric needle or disk to measure the magnitude and orientation of the electric field inside a cavity.

So far, the design of the position cavity is CR-oriented, the methodology presented in this disser-

tation is, however, certainly universal, and can easily be adapted to other storage rings on demand, such as the ESR and CSRc. Furthermore, the cavity doublet and the correction method for the anisochronism effect may also find their applications in the isochronous mass measurements in a few new storage rings that will be operational in the near future. Specifically, these include the Rare-RI Ring (R3) at RIKEN [156], the Test Storage Ring (TSR) at CERN [157], and the Spectrometry Ring (SRing) at HIAF [158].

The R3 is a cyclotron-based storage ring dedicated to the precision mass measurements of the neutron rich nuclei, in particular along the pathway of the r-process, by means of the IMS. The isochronous ion-optical setting of the ring can be achieved by tuning the trim coils on the inner sides of the dipole magnets. The measurements on the exotic nuclei are on a single-ion basis, where the produced secondary nuclei are identified in-flight by means of their positions, timings, and energy losses, and gated by a fast kicker at the entrance of the ring such that only the nuclei of interest get stored. Within this experimental scheme, it is expected to attain a measurement precision of the order of 10^{-6} with a measurement time shorter than 1 ms. Therefore, the relative stability of the magnetic field and the relative uncertainty of the timing system must be controlled on the same level.

The TSR, on the other hand, aims at the low energy regime ($0.5\text{--}10\text{ MeV}\cdot\text{u}^{-1}$), and, after being shipped from MPIK to CERN, will be coupled to an Isotope Separation On-Line (ISOL) radioactive beam facility. With the high-quality secondary beams delivered from the post-accelerator, a number of exciting experimental programs, such as the lifetimes of ${}^7\text{Be}$ in different atomic charge states, in-flight β -decay of light exotic nuclei, and capture reactions for the astrophysical p-process, could for the first time be addressed. The TSR may also be employed for the removal of isobaric contaminants from the stored ion beams and for the systematic studies within the neutrino beam program.

Similar to the CR at FAIR, the SRing at HIAF also serves two purposes for the high-intensity and high-energy rare isotope beams: collecting and stochastic pre-cooling of the injected beam, and nuclear mass measurements by means of the IMS. When operated in the isochronous mode, the SRing is an achromatic magnetic spectrometer with a momentum acceptance of $\pm 0.45\%$ and a transverse acceptance of $30\text{ mm}\cdot\text{mrad}$ at the transition energy of 1.835. Heavy ions with a maximum magnetic rigidity of $20\text{ T}\cdot\text{m}$ can be stored in the ring. Due to its resemblance to the CR, the SRing will be the next favorable ring to test the detection scheme with a cavity doublet and the correction method for the anisochronism effect in the nuclear mass measurements.

A MAXWELL'S EQUATIONS



Maxwell's equations, together with the Lorentz force law, have laid the foundation for classical electrodynamics. The most widely adopted form of Maxwell's equations is a set of partial differential equations, which reads

$$\nabla \cdot \tilde{\mathbf{E}} = \frac{\rho_e}{\varepsilon}, \quad (\text{A.1})$$

$$\nabla \cdot \tilde{\mathbf{H}} = 0, \quad (\text{A.2})$$

$$\nabla \times \tilde{\mathbf{E}} = -\mu \frac{\partial \tilde{\mathbf{H}}}{\partial t}, \quad (\text{A.3})$$

$$\nabla \times \tilde{\mathbf{H}} = \mathbf{J}_e + \varepsilon \frac{\partial \tilde{\mathbf{E}}}{\partial t}, \quad (\text{A.4})$$

where $\tilde{\mathbf{E}}$ is electric field, $\tilde{\mathbf{H}}$ is magnetic field, ρ_e is electric charge density, \mathbf{J}_e is electric current density, ε is permittivity of medium, and μ is permeability of medium.

For the free space without sources, eqs. (A.1) to (A.4) reduce to a homogeneous form:

$$\nabla \cdot \tilde{\mathbf{E}} = 0, \quad (\text{A.5})$$

$$\nabla \cdot \tilde{\mathbf{H}} = 0, \quad (\text{A.6})$$

$$\nabla \times \tilde{\mathbf{E}} = -\mu_0 \frac{\partial \tilde{\mathbf{H}}}{\partial t}, \quad (\text{A.7})$$

$$\nabla \times \tilde{\mathbf{H}} = \varepsilon_0 \frac{\partial \tilde{\mathbf{E}}}{\partial t}, \quad (\text{A.8})$$

where ε_0 and μ_0 are the permittivity and permeability of free space, respectively. By virtue of the vector identity

$$\nabla \times (\nabla \times \mathbf{A}) \equiv \nabla(\nabla \cdot \mathbf{A}) - \nabla^2 \mathbf{A}, \quad (\text{A.9})$$

taking the curl of eq. (A.7) and plugging in eq. (A.5) lead to the wave equation of the electric field:

$$\nabla^2 \tilde{\mathbf{E}} - \frac{\partial^2 \tilde{\mathbf{E}}}{c^2 \partial t^2} = 0, \quad (\text{A.10})$$

where the speed of light in free space c is related to ε_0 and μ_0 via

$$c = \frac{1}{\sqrt{\varepsilon_0 \mu_0}}. \quad (\text{A.11})$$

By means of separation of variables: $\tilde{\mathbf{E}}(\mathbf{x}, t) = \mathbf{E}(\mathbf{x})T(t)$, where \mathbf{x} represents spatial coordinates and t is time, eq. (A.10) can be decoupled to a temporal part—a second-order ordinary differential

equation:

$$\frac{d^2 T}{dt^2} + c^2 k^2 T = 0, \quad (\text{A.12})$$

and a spatial part—the Helmholtz partial differential equation:

$$\nabla^2 \mathbf{E} + k^2 \mathbf{E} = 0, \quad (\text{A.13})$$

where the constant k is named wavenumber.

The solution to eq. (A.12) is a linear combination of sine and cosine functions. It can be generalized as $e^{-i\omega_0 t}$ with an angular frequency $\omega_0 = ck$. The solution to eq. (A.13) depends on boundary conditions. For instance, a perfectly conductive boundary leads to

$$\mathbf{n} \times \mathbf{E} = 0, \quad (\text{A.14})$$

$$\mathbf{n} \cdot \mathbf{H} = 0, \quad (\text{A.15})$$

where \mathbf{n} is the normal vector to the boundary. The geometry of the boundary decides the most appropriate coordinate system in which eq. (A.13) is to be solved.

Likewise, the wave equation and the Helmholtz equation of the magnetic field read

$$\nabla^2 \tilde{\mathbf{H}} - \frac{\partial^2 \tilde{\mathbf{H}}}{c^2 \partial t^2} = 0, \quad (\text{A.16})$$

$$\nabla^2 \mathbf{H} + k^2 \mathbf{H} = 0, \quad (\text{A.17})$$

with $\tilde{\mathbf{H}}(\mathbf{x}, t) = \mathbf{H}(\mathbf{x})e^{-i(\omega_0 t - \pi/2)}$.

A.1 Cartesian Coordinate System

For a rectangular cavity, it is convenient to solve eq. (A.13) in a Cartesian coordinate system. Let a , b , and d be the height, width, and depth of the cavity, respectively. Without loss of generality, assume the relation $a > b > d$ holds. The origin of the coordinate system is located at a vertex of the cavity. Three mutually orthogonal axes x , y , and z align with b (horizontal), a (vertical), and d (longitudinal), respectively.

The explicit form of the Laplace operator ∇^2 in the Cartesian coordinates reads

$$\nabla^2 = \frac{\partial^2}{\partial x^2} + \frac{\partial^2}{\partial y^2} + \frac{\partial^2}{\partial z^2}. \quad (\text{A.18})$$

The electric field \mathbf{E} can be expanded as

$$\mathbf{E}(\mathbf{x}) = E_x(x, y, z)\hat{\mathbf{x}} + E_y(x, y, z)\hat{\mathbf{y}} + E_z(x, y, z)\hat{\mathbf{z}}. \quad (\text{A.19})$$

The hatted letters $\hat{\mathbf{x}}$, $\hat{\mathbf{y}}$, and $\hat{\mathbf{z}}$ denote normalized basis vectors in the horizontal, vertical, and longitudinal directions, respectively. As a result, eq. (A.13) in fact consists of three scalar equations:

$$\left(\frac{\partial^2}{\partial x^2} + \frac{\partial^2}{\partial y^2} + \frac{\partial^2}{\partial z^2} + k^2 \right) E_x(x, y, z) = 0, \quad (\text{A.20})$$

$$\left(\frac{\partial^2}{\partial x^2} + \frac{\partial^2}{\partial y^2} + \frac{\partial^2}{\partial z^2} + k^2 \right) E_y(x, y, z) = 0, \quad (\text{A.21})$$

$$\left(\frac{\partial^2}{\partial x^2} + \frac{\partial^2}{\partial y^2} + \frac{\partial^2}{\partial z^2} + k^2 \right) E_z(x, y, z) = 0. \quad (\text{A.22})$$

Again, eqs. (A.20) to (A.22) can be solved via separation of variables. The general solution is complicated though, a particular solution that fulfills eq. (A.14) neatly reads [97]

$$E_x(x, y, z) = E_{x0} \cos(k_x x) \sin(k_y y) \sin(k_z z), \quad (\text{A.23})$$

$$E_y(x, y, z) = E_{y0} \sin(k_x x) \cos(k_y y) \sin(k_z z), \quad (\text{A.24})$$

$$E_z(x, y, z) = E_{z0} \sin(k_x x) \sin(k_y y) \cos(k_z z), \quad (\text{A.25})$$

$$\text{with } k_x = \frac{n\pi}{b}, \quad k_y = \frac{m\pi}{a}, \quad k_z = \frac{l\pi}{d}. \quad (\text{A.26})$$

Here, the nonnegative integers n , m , and l are mode numbers which define EM field patterns; E_{x0} , E_{y0} , and E_{z0} are scaling factors, and, according to eq. (A.5), are constrained via

$$k_x E_{x0} + k_y E_{y0} + k_z E_{z0} = 0. \quad (\text{A.27})$$

Besides, k_x , k_y , and k_z alone must fulfill the relation

$$k_x^2 + k_y^2 + k_z^2 = k^2 = \frac{\omega_0^2}{c^2}. \quad (\text{A.28})$$

Based on eq. (A.7), after taking into account the phase difference, the magnetic field \mathbf{H} can be obtained via

$$\mathbf{H} = -\frac{1}{\omega_0 \mu_0} \nabla \times \mathbf{E}, \quad (\text{A.29})$$

which delivers

$$H_x(x, y, z) = \frac{k_z E_{y0} - k_y E_{z0}}{\omega_0 \mu_0} \sin(k_x x) \cos(k_y y) \cos(k_z z), \quad (\text{A.30})$$

$$H_y(x, y, z) = \frac{k_x E_{z0} - k_z E_{x0}}{\omega_0 \mu_0} \cos(k_x x) \sin(k_y y) \cos(k_z z), \quad (\text{A.31})$$

$$H_z(x, y, z) = \frac{k_y E_{x0} - k_x E_{y0}}{\omega_0 \mu_0} \cos(k_x x) \cos(k_y y) \sin(k_z z). \quad (\text{A.32})$$

In particular, the fundamental mode with the lowest frequency, which is also the monopole mode, is given by the mode numbers $(n, m, l) = (1, 1, 0)$. Note that $(1, 0, 0)$ does not exist, according to eq. (A.27). The EM fields in such a mode are given as

$$E_x = 0, \quad (\text{A.33})$$

$$E_y = 0, \quad (\text{A.34})$$

$$E_z = E_0 \sin\left(\frac{\pi x}{b}\right) \sin\left(\frac{\pi y}{a}\right), \quad (\text{A.35})$$

$$H_x = -\frac{\pi E_0}{\omega_0 \mu_0 a} \sin\left(\frac{\pi x}{b}\right) \cos\left(\frac{\pi y}{a}\right), \quad (\text{A.36})$$

$$H_y = \frac{\pi E_0}{\omega_0 \mu_0 b} \cos\left(\frac{\pi x}{b}\right) \sin\left(\frac{\pi y}{a}\right), \quad (\text{A.37})$$

$$H_z = 0, \quad (\text{A.38})$$

with a resonant frequency

$$f_0 = \frac{c}{2} \sqrt{\frac{1}{a^2} + \frac{1}{b^2}}. \quad (\text{A.39})$$

A.2 Cylindrical Coordinate System

A cylindrical coordinate system is suitable for solving eq. (A.13) in a circular cylindrical cavity. Let a and d be the radius and height of the cavity, respectively. The origin of the coordinate system is located in the center of one circular face. Three coordinates r , ϑ , and z denote the radial, azimuthal, and axial direction, respectively.

In such a coordinate system, the electric field is expressed as

$$\mathbf{E}(\mathbf{x}) = E_r(r, \vartheta, z)\hat{\mathbf{r}} + E_\vartheta(r, \vartheta, z)\hat{\boldsymbol{\vartheta}} + E_z(r, \vartheta, z)\hat{\mathbf{z}}, \quad (\text{A.40})$$

where hatted symbols are normalized basis vectors in the corresponding directions. The Laplace operator now becomes

$$\nabla^2 = \frac{\partial}{r\partial r} \left(r \frac{\partial}{\partial r} \right) + \frac{\partial^2}{r^2\partial\vartheta^2} + \frac{\partial^2}{\partial z^2}. \quad (\text{A.41})$$

Likewise, eq. (A.13) can be expanded to a set of scalar equations:

$$\left[\frac{\partial}{r\partial r} \left(r \frac{\partial}{\partial r} \right) + \frac{\partial^2}{r^2\partial\vartheta^2} + \frac{\partial^2}{\partial z^2} + k^2 \right] E_r(r, \vartheta, z) = 0, \quad (\text{A.42})$$

$$\left[\frac{\partial}{r\partial r} \left(r \frac{\partial}{\partial r} \right) + \frac{\partial^2}{r^2\partial\vartheta^2} + \frac{\partial^2}{\partial z^2} + k^2 \right] E_\vartheta(r, \vartheta, z) = 0, \quad (\text{A.43})$$

$$\left[\frac{\partial}{r\partial r} \left(r \frac{\partial}{\partial r} \right) + \frac{\partial^2}{r^2\partial\vartheta^2} + \frac{\partial^2}{\partial z^2} + k^2 \right] E_z(r, \vartheta, z) = 0. \quad (\text{A.44})$$

While the general solution to eqs. (A.42) to (A.44) can be calculated by separation of variables, the main interest will be focused on a particular subset where the magnetic field does not have an axial component. This narrows the scope down to the TM modes. The exact formulae are given as [97]

$$E_r = -\frac{E_0 k_z}{k_r} J'_n(k_r r) \cos(n\vartheta) \sin(k_z z), \quad (\text{A.45})$$

$$E_\vartheta = \frac{nE_0 k_z}{k_r^2 r} J_n(k_r r) \sin(n\vartheta) \sin(k_z z), \quad (\text{A.46})$$

$$E_z = E_0 J_n(k_r r) \cos(n\vartheta) \cos(k_z z), \quad (\text{A.47})$$

$$H_r = \frac{nE_0 \omega_0 \varepsilon_0}{k_r^2 r} J_n(k_r r) \sin(n\vartheta) \cos(k_z z), \quad (\text{A.48})$$

$$H_\vartheta = \frac{E_0 \omega_0 \varepsilon_0}{k_r} J'_n(k_r r) \cos(n\vartheta) \cos(k_z z), \quad (\text{A.49})$$

$$H_z = 0, \quad (\text{A.50})$$

where E_0 is a scaling factor, J_n is the Bessel function of order n , and J'_n is its corresponding derivative. Moreover, n , k_r , and k_z are separation constants, among which n is a nonnegative integer and the other two fulfill the relation

$$k_r^2 + k_z^2 = k^2 = \frac{\omega_0^2}{c^2}. \quad (\text{A.51})$$

It can also be verified that \mathbf{E} and \mathbf{H} fulfill eq. (A.29) by virtue of eqs. (A.11) and (A.51).

According to eq. (A.15), H_r must vanish when $r = a$, which essentially requires that

$$J_n(k_r a) = 0, \quad \Rightarrow \quad k_r = \frac{j_{nm}}{a}, \quad (\text{A.52})$$

where j_{nm} is the m th root of J_n . From eq. (A.14), it is required that E_r and E_ϑ must vanish when $z = d$. Therefore, the following equation must hold:

$$\sin(k_z d) = 0, \quad \Rightarrow \quad k_z = \frac{l\pi}{d}, \quad (\text{A.53})$$

where l is a nonnegative integer.

In particular, the EM fields in the monopole mode, by letting $(n, m, l) = (0, 1, 0)$, read

$$E_r = 0, \quad (\text{A.54})$$

$$E_\vartheta = 0, \quad (\text{A.55})$$

$$E_z = E_0 J_0 \left(\frac{j_{01} r}{a} \right), \quad (\text{A.56})$$

$$H_r = 0, \quad (\text{A.57})$$

$$H_\vartheta = \frac{E_0 \omega_0 \varepsilon_0 a}{j_{01}} J_0' \left(\frac{j_{01} r}{a} \right), \quad (\text{A.58})$$

$$H_z = 0, \quad (\text{A.59})$$

with the lowest resonant frequency

$$f_0 = \frac{j_{01} c}{2\pi a}. \quad (\text{A.60})$$

A.3 Elliptic Cylindrical Coordinate System

An elliptic cylindrical coordinate system is a generalization of a cylindrical coordinate system, which is useful for solving the Helmholtz equation in a cylindrical cavity with an elliptic cross section. By virtue of a Cartesian coordinate system, the widely adopted definition of the elliptic cylindrical coordinates (ν, ϑ, z) reads

$$x = r \cosh \nu \cos \vartheta, \quad (\text{A.61})$$

$$y = r \sinh \nu \sin \vartheta, \quad (\text{A.62})$$

$$z = z, \quad (\text{A.63})$$

where $\nu \in [0, +\infty)$ and $\vartheta \in [0, 2\pi)$. Occasionally, it is convenient to organize eqs. (A.61) and (A.62) into a compact form:

$$x + iy = r \cosh(\nu + i\vartheta). \quad (\text{A.64})$$

A.3.1 Elliptic Coordinate System

The first two coordinates (ν, ϑ) in eqs. (A.61) and (A.62) span a two-dimensional elliptic coordinate subsystem, where the coordinate curves are confocal ellipses and hyperbolae with a focal length of r . In addition, all the ellipses and hyperbolae intersect at right angles, because (ν, ϑ) is an orthogonal coordinate system.

A special elliptic coordinate system with $r = 1$ is illustrated in fig. A.1. It is then clear that an ellipse can be formed by fixing ν and only varying ϑ . The size of the ellipse is defined by r , whereas the eccentricity is determined by ν . The major axis a and the minor axis b of the ellipse can be transformed from r and ν via

$$a = 2r \cosh \nu, \quad (\text{A.65})$$

$$b = 2r \sinh \nu, \quad (\text{A.66})$$

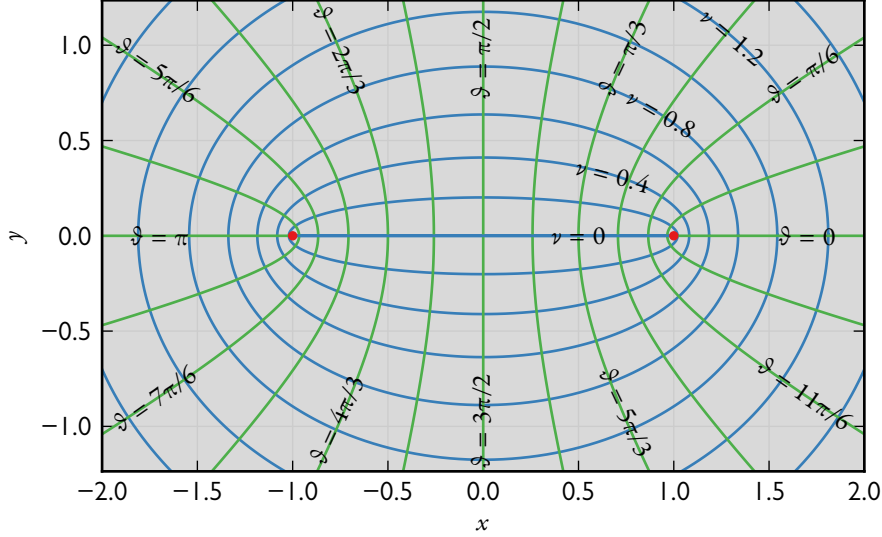


Figure A.1 Elliptic coordinate system with a unitary focal length. The blue ellipses are coordinate curves of ν , while the green hyperbolae are coordinate curves of ϑ . The red dots represent their common foci.

or vice versa:

$$r = \frac{\sqrt{a^2 - b^2}}{2}, \quad (\text{A.67})$$

$$\nu = \operatorname{artanh}\left(\frac{b}{a}\right). \quad (\text{A.68})$$

Note that a polar coordinate system can be reckoned a special case of the elliptic coordinate system in the limit of $r \rightarrow 0$ as the foci collapse to one point at the origin. Therefore, the coordinate ϑ analogously indicates the azimuthal direction in the elliptic coordinates.

Suppose that the origin of the elliptic cylindrical coordinate system is located in the center of one base of the cavity, while the z -axis lies in the axial direction. The electric field \mathbf{E} is then expanded as

$$\mathbf{E}(\mathbf{x}) = E_\nu(\nu, \vartheta, z)\hat{\boldsymbol{\nu}} + E_\vartheta(\nu, \vartheta, z)\hat{\boldsymbol{\vartheta}} + E_z(\nu, \vartheta, z)\hat{\mathbf{z}}, \quad (\text{A.69})$$

where hatted symbols are normalized basis vectors for the corresponding coordinates. The Laplace operator in the elliptic cylindrical coordinate system reads

$$\nabla^2 = \frac{1}{r^2(\sinh^2 \nu + \sin^2 \vartheta)} \left(\frac{\partial^2}{\partial \nu^2} + \frac{\partial^2}{\partial \vartheta^2} \right) + \frac{\partial^2}{\partial z^2}. \quad (\text{A.70})$$

Now eq. (A.13) can explicitly be expressed as

$$\left[\frac{1}{r^2(\sinh^2 \nu + \sin^2 \vartheta)} \left(\frac{\partial^2}{\partial \nu^2} + \frac{\partial^2}{\partial \vartheta^2} \right) + \frac{\partial^2}{\partial z^2} + k^2 \right] E_\nu(\nu, \vartheta, z) = 0, \quad (\text{A.71})$$

$$\left[\frac{1}{r^2(\sinh^2 \nu + \sin^2 \vartheta)} \left(\frac{\partial^2}{\partial \nu^2} + \frac{\partial^2}{\partial \vartheta^2} \right) + \frac{\partial^2}{\partial z^2} + k^2 \right] E_\vartheta(\nu, \vartheta, z) = 0, \quad (\text{A.72})$$

$$\left[\frac{1}{r^2(\sinh^2 \nu + \sin^2 \vartheta)} \left(\frac{\partial^2}{\partial \nu^2} + \frac{\partial^2}{\partial \vartheta^2} \right) + \frac{\partial^2}{\partial z^2} + k^2 \right] E_z(\nu, \vartheta, z) = 0. \quad (\text{A.73})$$

Analytically solving the general solution to eqs. (A.71) to (A.73) is much more challenging than doing so in a cylindrical coordinate system. Even for the particular solution in the TM modes, it presents great difficulties. Here, the attention is only paid to the monopole mode. In analogy with eqs. (A.54) to (A.59), it is reasonable to stipulate that $E_\nu = E_\vartheta = H_z = 0$, while E_z , H_ν , and H_ϑ are independent of z . The effort is then focused on solving a two-dimensional Helmholtz equation in an elliptic coordinate system.

Substituting $E_z(\nu, \vartheta) = N(\nu)\Theta(\vartheta)$ into eq. (A.73) leads to

$$\frac{d^2\Theta}{d\vartheta^2} + (k^2 r^2 \sin^2 \vartheta + k_s) \Theta = 0, \quad (\text{A.74})$$

$$\frac{d^2 N}{d\nu^2} + (k^2 r^2 \sinh^2 \nu - k_s) N = 0, \quad (\text{A.75})$$

where k_s is a separation constant. By virtue of the relations:

$$\sin^2 \vartheta = \frac{1 - \cos(2\vartheta)}{2}, \quad (\text{A.76})$$

$$\sinh^2 \nu = \frac{\cosh(2\nu) - 1}{2}, \quad (\text{A.77})$$

eqs. (A.74) and (A.75) can be reformulated to

$$\frac{d^2\Theta}{d\vartheta^2} + [w - 2u \cos(2\vartheta)] \Theta = 0, \quad (\text{A.78})$$

$$\frac{d^2 N}{d\nu^2} - [w - 2u \cosh(2\nu)] N = 0, \quad (\text{A.79})$$

where the substitutions

$$u = \frac{k^2 r^2}{4}, \quad (\text{A.80})$$

$$w = \frac{k^2 r^2}{2} + k_s, \quad (\text{A.81})$$

have been applied.

A.3.2 Mathieu Functions

Equations (A.78) and (A.79) are known as the ordinary and modified Mathieu equation, respectively. Their corresponding solutions are the Mathieu functions and the modified Mathieu functions. From the similarity between elliptic and polar coordinates, it can be shown that in the limit of $r \rightarrow 0$ the Mathieu functions degenerate to the sinusoidal functions, while the modified Mathieu functions degenerate to the Bessel functions [159].

The Mathieu functions have two independent families, namely $ce_m(\vartheta; u)$ and $se_m(\vartheta; u)$, with even and odd polarity, respectively. The nonnegative integer m runs from zero for ce_m , but only from one for se_m . The Mathieu functions depend not only on the variable ϑ , but also on the parameter u . The rotational symmetry of the boundary requires that ce_m and se_m are periodic with a period of π (m is even) or 2π (m is odd), which assigns a discrete set of values, i.e. eigenvalues, to w in eq. (A.78). When sorted in an ascending order, the ordinal rank of w is indexed by m . Given a particular combination of (u, m) , w is accordingly fixed.

Recalling the electric field pattern in the monopole mode in a circular cavity, it is natural to imagine that E_z does not change its sign in the whole cross section and concentrates in the central region as

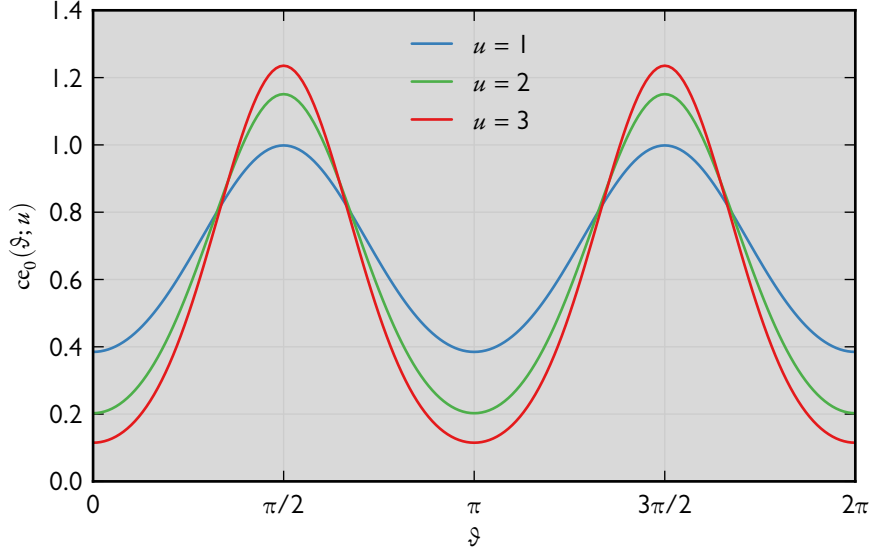


Figure A.2 Even Mathieu function of order zero with various parameters.

well for an elliptic cavity. Therefore, ce_0 is the only solution that can correctly describe the azimuthal behavior of E_z [159]. The visualization of $ce_0(\vartheta; u)$ with different parameters is plotted in fig. A.2.

Likewise, the modified Mathieu functions also have two independent families, namely $Ce_m(\nu; u)$ and $Se_m(\nu; u)$, with even and odd polarity, respectively. The mode number m is the same as the one in ce_m and se_m because of the joint constants u and w in eqs. (A.78) and (A.79). Having selected ce_0 as the azimuthal part of E_z , only Ce_0 and Se_0 are eligible for the radial part. However, due to the odd polarity, Se_0 vanishes when $\nu = 0$, which should obviously be discarded. The visualization of $Ce_0(\nu; u)$ with different parameters is plotted in fig. A.3.

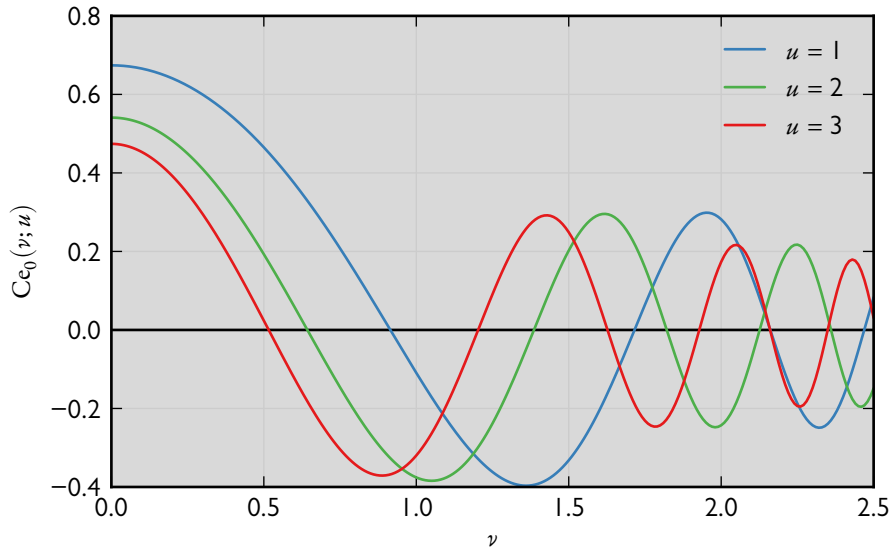


Figure A.3 Even modified Mathieu function of order zero with various parameters.

The complete expression of E_z hence reads

$$E_z = E_0 Ce_0(\nu; u) ce_0(\vartheta; u), \quad (\text{A.82})$$

where E_0 is a scaling factor. The free parameter u can be determined by applying the boundary condition, which requires that E_z vanishes at the elliptic boundary according to eq. (A.14). Let c_{01} be the first root of $Ce_0(\nu; u)$. It must comply with the boundary shape. That is to say, c_{01} can be determined from the major and minor axis of the ellipse by substituting for ν in eq. (A.68). With c_{01} known, the parameter \tilde{u} in this case can be obtained accordingly by solving $Ce_0(c_{01}; u) = 0$. Combining eqs. (A.67) and (A.80) leads to a resonant frequency

$$f_0 = \frac{2c}{\pi} \sqrt{\frac{\tilde{u}}{a^2 - b^2}}. \quad (\text{A.83})$$

The magnetic field components H_ν and H_ϑ can be obtained by virtue of eq. (A.29). The full expressions of EM fields in the monopole mode are given as

$$E_\nu = 0, \quad (\text{A.84})$$

$$E_\vartheta = 0, \quad (\text{A.85})$$

$$E_z = E_0 Ce_0(\nu; \tilde{u}) ce_0(\vartheta; \tilde{u}), \quad (\text{A.86})$$

$$H_\nu = -\frac{E_0 Ce_0(\nu; \tilde{u}) ce'_0(\vartheta; \tilde{u})}{2\mu_0 c \sqrt{\tilde{u}(\sinh^2 \nu + \sin^2 \vartheta)}}, \quad (\text{A.87})$$

$$H_\vartheta = \frac{E_0 Ce'_0(\nu; \tilde{u}) ce_0(\vartheta; \tilde{u})}{2\mu_0 c \sqrt{\tilde{u}(\sinh^2 \nu + \sin^2 \vartheta)}}, \quad (\text{A.88})$$

$$H_z = 0, \quad (\text{A.89})$$

where ce'_0 is the derivative of ce_0 with respect to ϑ , and Ce'_0 is the derivative of Ce_0 with respect to ν .

B ENGINEERING DRAWINGS



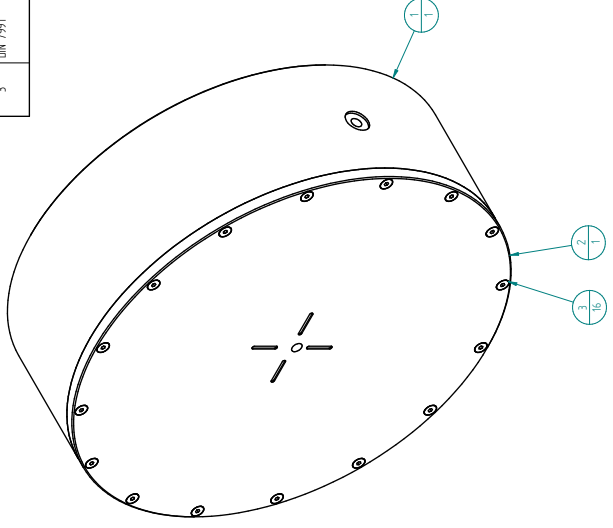
The engineering drawings for the manufacture of prototype cavities are reprinted with permission from Kreß GmbH. Each drawing is scaled down by a factor of eight. The reader is advised to refer to the electronic version of this dissertation for a better readability. As an index, table B.1 summarizes all the parts of the cavities.

Table B.1 Lookup table containing sheet numbers of drawings and the corresponding cavity parts.

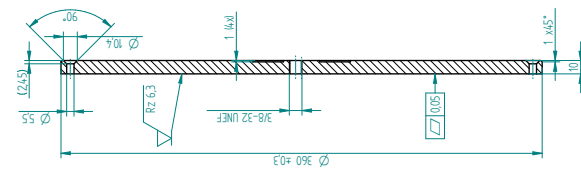
Sheet number	Description
15.024.01.00	circular cavity
15.024.01.01	cavity body
15.024.01.02	cavity lid
15.024.02.00	rectangular cavity
15.024.02.01	cavity body
15.024.02.02	cavity lid
15.024.03.00	elliptic cavity
15.024.03.01	cavity lid
15.024.03.02	cavity body
15.024.02.03	beam pipe
15.024.02.04	plunger
15.024.02.05	holder
15.024.02.06	stud
15.024.03.03	blocking screw

Pos.Nr.	Dokumentnummer	Index	Titel	Material	Menge
1	15.024.0101	A	Resonator zylindrisch	Al MgSi1	1
2	15.024.0102	A	Resonatordeckel	Alpalm	1
3	DIN 7991		N_Senkschraube DIN 7991 - M5x16 - A2-70	A2-70	16

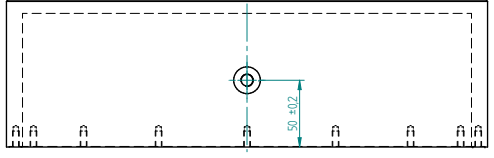
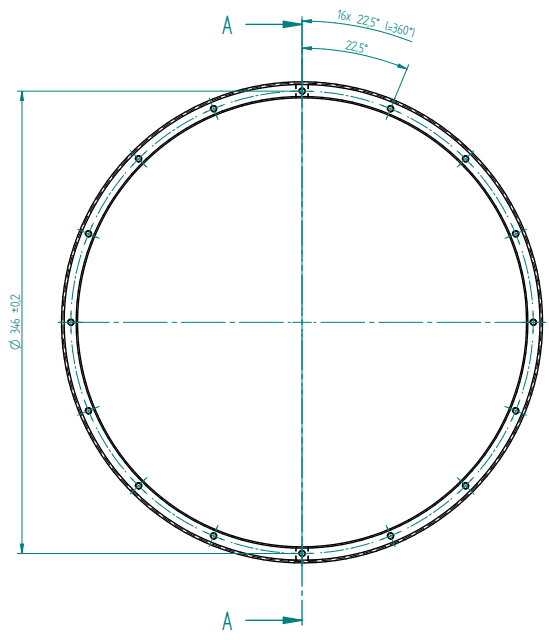
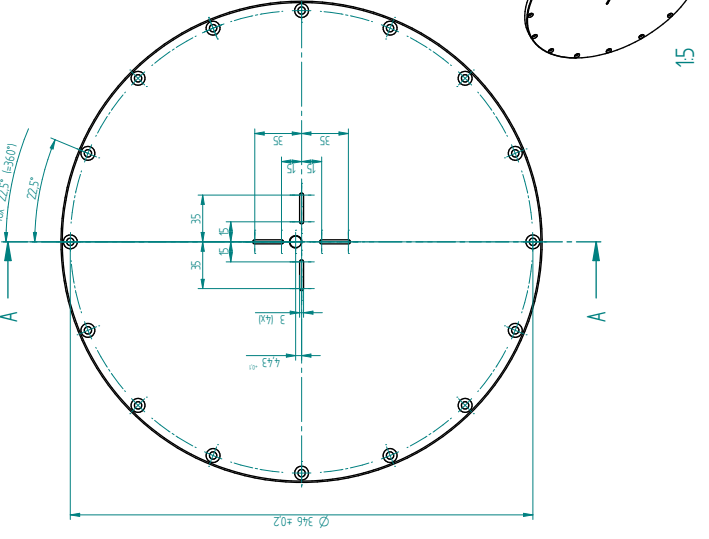
Diese Zeichnung ist urheberrechtlich geschützt. Sie darf ohne unsere schriftliche Zustimmung weder ververvielfältigt noch in irgendeiner Weise an Dritte weitergegeben werden.
 Krefl GmbH
 Resonator zylindrisch ver.
 Blatt: 15.024.0101



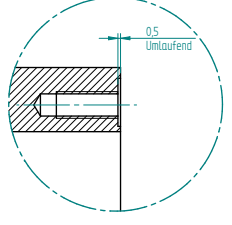
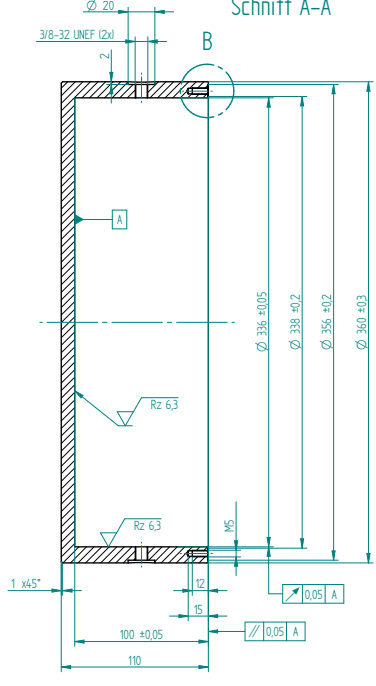
Schnitt A-A



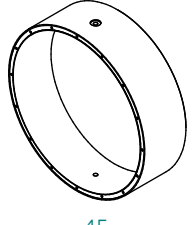
Diese Zeichnung ist urheberrechtlich geschützt. Sie darf ohne unsere schriftliche Zustimmung weder ververvielfältigt noch in irgendeiner Weise an Dritte weitergegeben werden.
 Krefl GmbH
 Resonatordeckel
 Blatt: 15.024.0102



Schnitt A-A

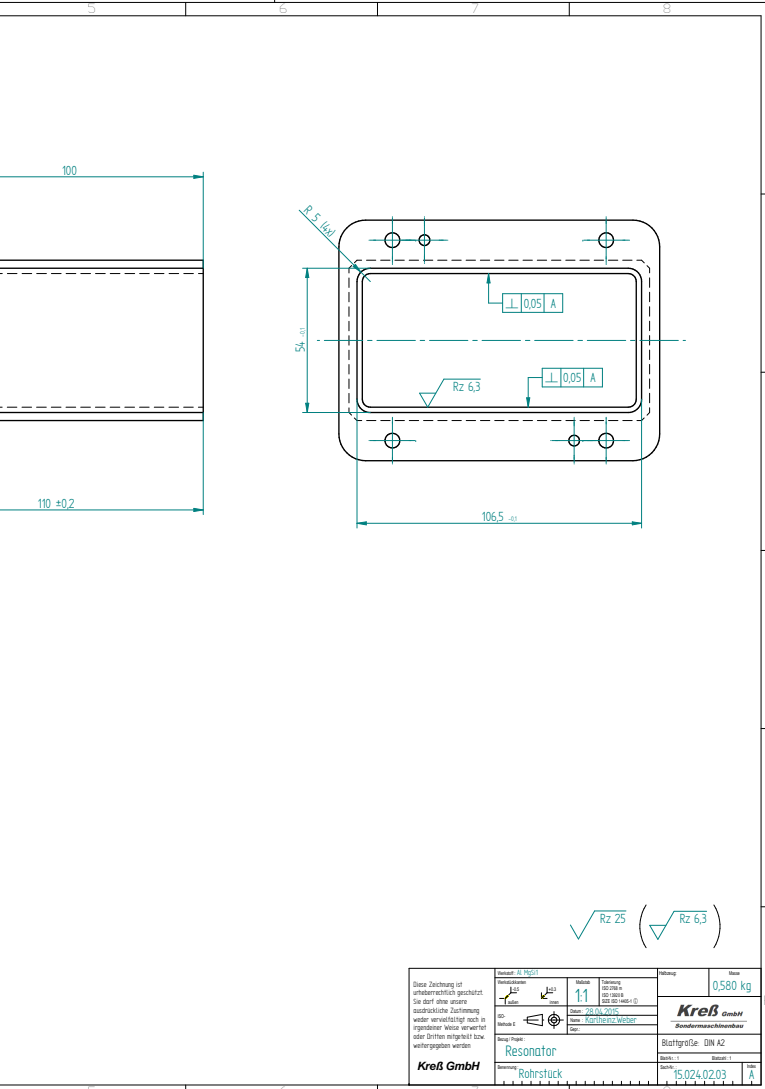
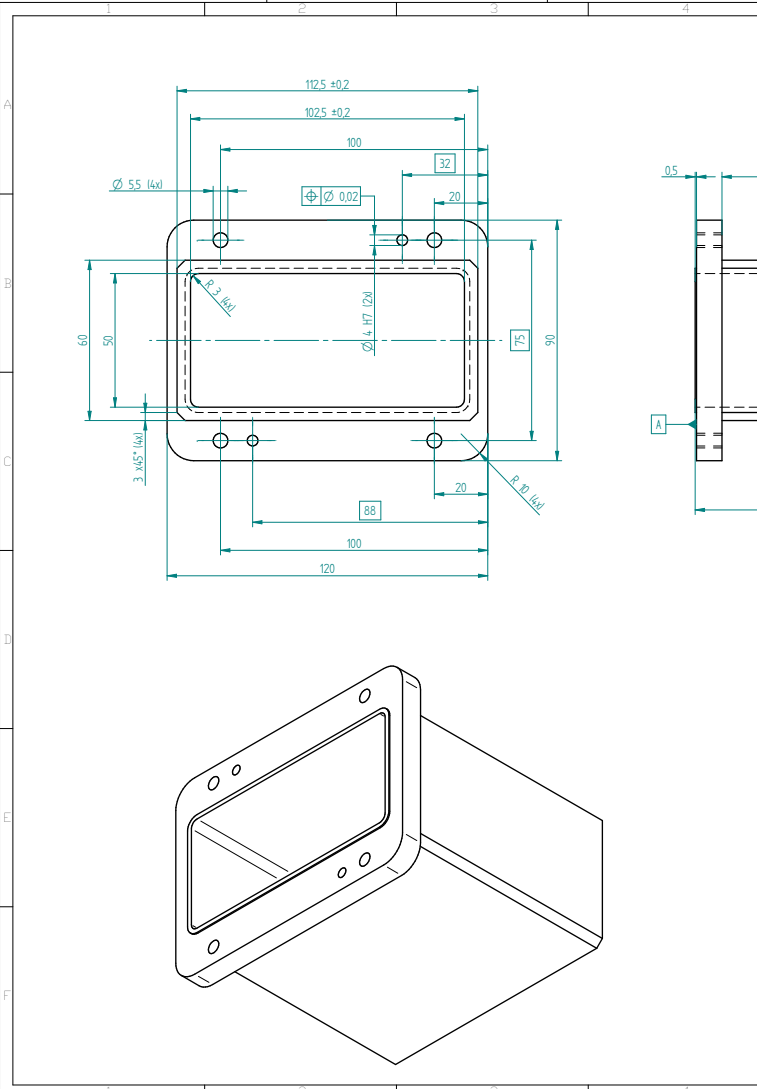
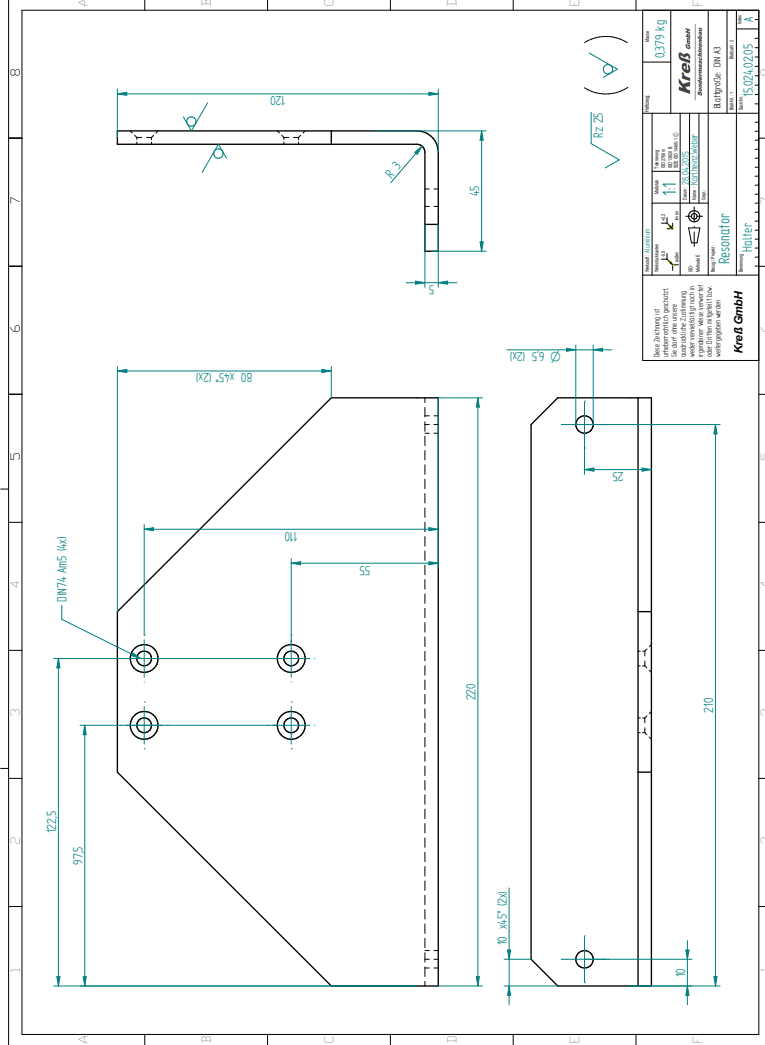
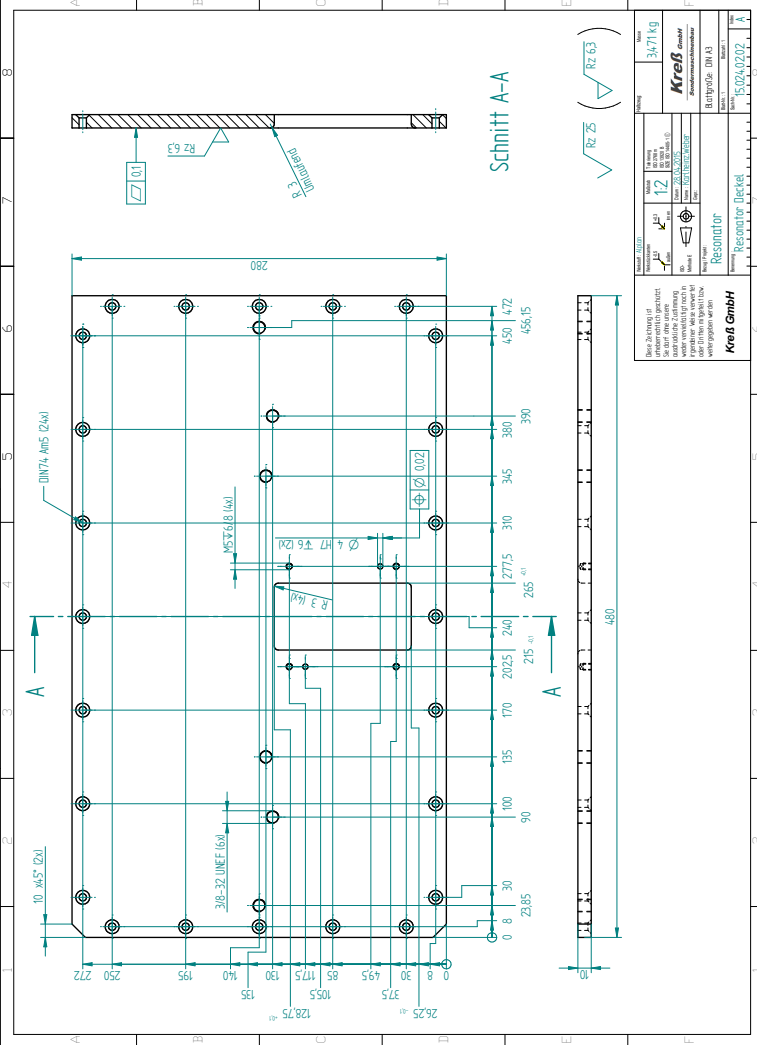


Einzelheit B 21

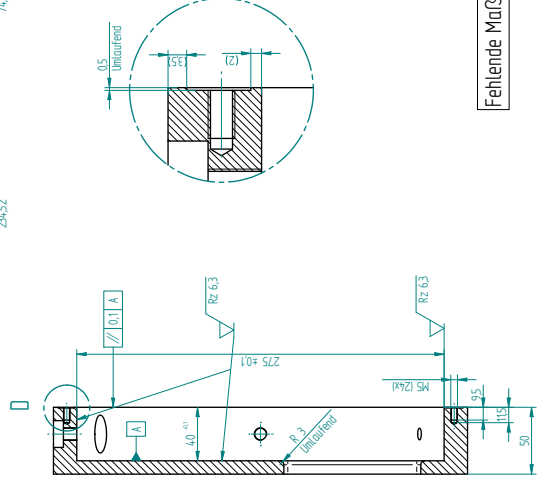
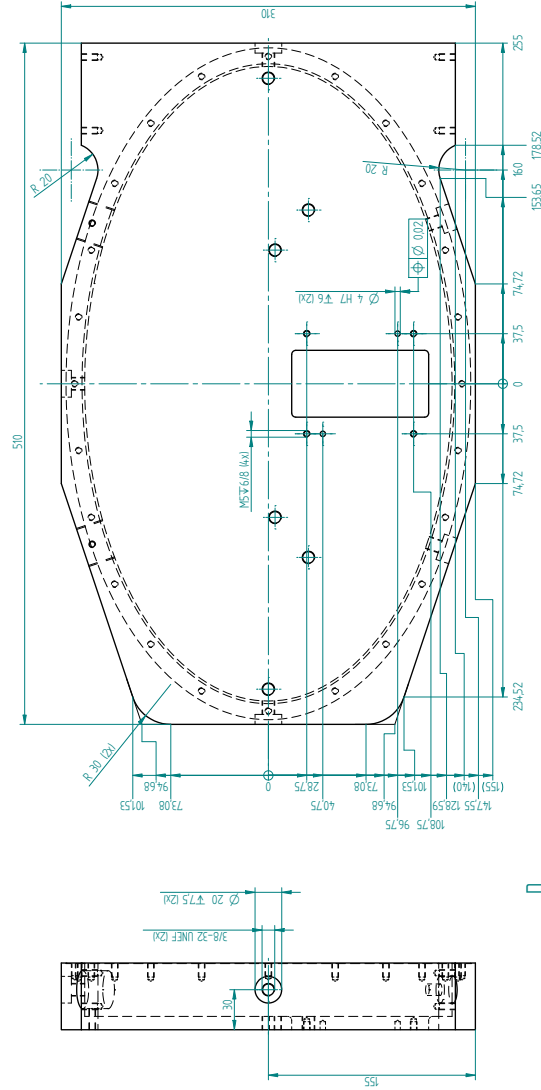
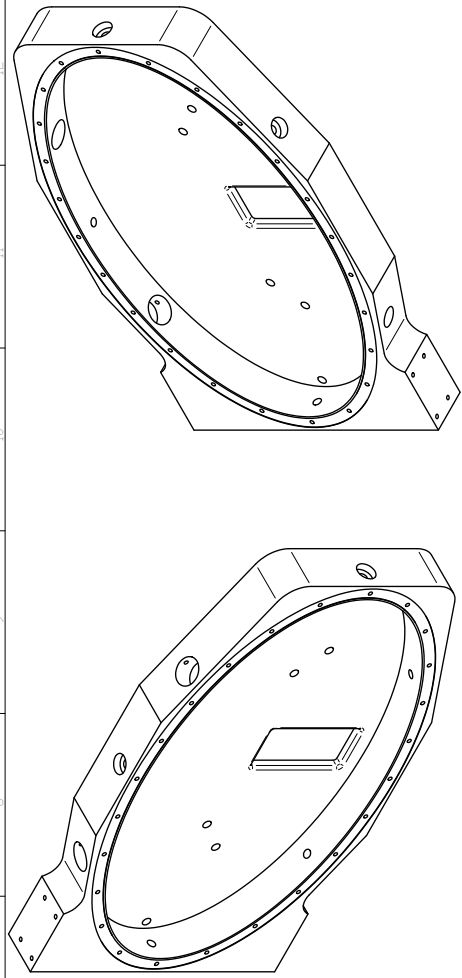


√ Rz 2.5 (√ Rz 6.3)

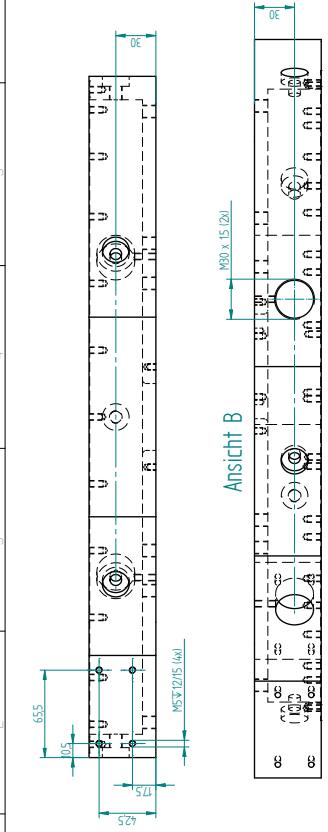
Diese Zeichnung ist urheberrechtlich geschützt. Sie darf ohne unsere schriftliche Zustimmung weder ververvielfältigt noch in irgendeiner Weise an Dritte weitergegeben werden.
 Krefl GmbH
 Resonator zylindrisch
 Blatt: 15.024.0101



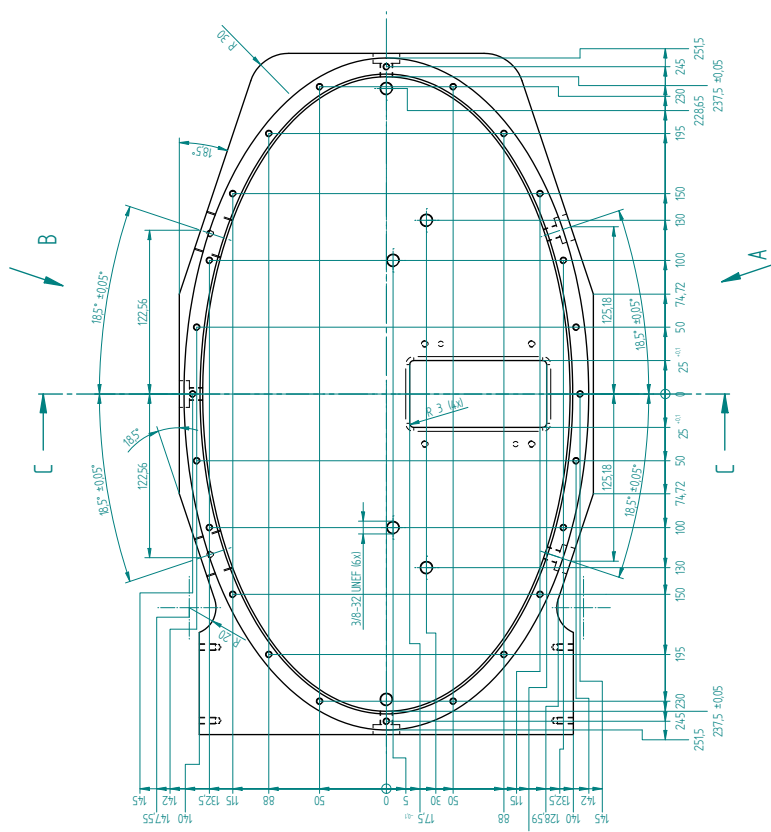
Dieser Zeichnung ist urheberrechtlich geschützt. Sie darf ohne unsere schriftliche Zustimmung weder ververvielfältigt noch in irgendeiner Weise erneut oder Dritten eingeleitet bzw. weitergegeben werden.		Blattgröße: DIN A2 Blatt: 1 Datum: 15.024.0203	Menge: 0580 kg Kreß GmbH Sondermaschinenbau
Blatt: 1 Datum: 15.024.0203	Blattgröße: DIN A2 Blatt: 1 Datum: 15.024.0203	Blattgröße: DIN A2 Blatt: 1 Datum: 15.024.0203	Menge: 0580 kg Kreß GmbH Sondermaschinenbau



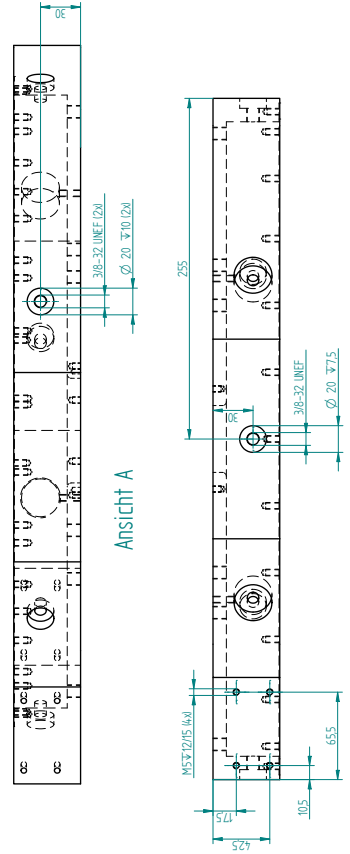
Schnitt C-C



Ansicht B



Ansicht A



Einzelheit D
2:1

Fehlende Maße siehe 30 Daten



Diese Zeichnung ist unvollständig, wenn nicht alle Angaben in der Tabelle erfüllt sind.		Blatt 1 von 1	7748 kg
Maßstab 1:1	Blatt 12	Blatt 1	Kref GmbH Resonator Ellipse
Material 1.4571	Zeichnung 15.02.03.02	Blatt 1	Blatt 1
Zeichnung 15.02.03.02	Blatt 1	Blatt 1	Blatt 1

BIBLIOGRAPHY



- [1] F. Bosch, Yu. A. Litvinov *et al.*, “Nuclear physics with unstable ions at storage rings”. *Prog. Part. Nucl. Phys.*, **73** (2013) 84.
- [2] Yu. A. Litvinov and F. Bosch, “Beta decay of highly charged ions”. *Rep. Prog. Phys.*, **74** (2011) 016301.
- [3] P. H. Mokler and Th. Stöhlker, “The physics of highly charged heavy ions revealed by storage/cooler rings”. *Adv. At. Mol. Opt. Phys.*, **37** (1996) 297.
- [4] M. Larsson, “Atomic and molecular physics with ion storage rings”. *Rep. Prog. Phys.*, **58** (1995) 1267.
- [5] B. Franzke, “The heavy ion storage and cooler ring project ESR at GSI”. *Nucl. Instrum. Meth. B*, **24–25, Part 1** (1987) 18.
- [6] J. W. Xia, W. L. Zhan *et al.*, “The heavy ion cooler-storage-ring project (HIRFL-CSR) at Lanzhou”. *Nucl. Instrum. Meth. A*, **488** (2002) 11.
- [7] B. Franzke, H. Geissel *et al.*, “Mass and lifetime measurements of exotic nuclei in storage rings”. *Mass Spectrom. Rev.*, **27** (2008) 428.
- [8] Yu. A. Litvinov, S. Bishop *et al.*, “Nuclear physics experiments with ion storage rings”. *Nucl. Instrum. Meth. B*, **317, Part B** (2013) 603.
- [9] H. S. Xu, Y. H. Zhang *et al.*, “Accurate mass measurements of exotic nuclei with the CSRe in Lanzhou”. *Int. J. Mass Spectrom.*, **349–350** (2013) 162.
- [10] F. Bosch and Yu. A. Litvinov, “Mass and lifetime measurements at the experimental storage ring of GSI”. *Int. J. Mass Spectrom.*, **349–350** (2013) 151.
- [11] F. Nolden, P. Hülsmann *et al.*, “A fast and sensitive resonant Schottky pick-up for heavy ion storage rings”. *Nucl. Instrum. Meth. A*, **659** (2011) 69.
- [12] J. Trötscher, K. Balog *et al.*, “Mass measurements of exotic nuclei at the ESR”. *Nucl. Instrum. Meth. B*, **70** (1992) 455.
- [13] B. Mei, X. Tu *et al.*, “A high performance time-of-flight detector applied to isochronous mass measurement at CSRe”. *Nucl. Instrum. Meth. A*, **624** (2010) 109.
- [14] O. Klepper, “Bound-state beta decay and nuclear lifetime measurements at the storage-cooler ring ESR”. *Nucl. Phys. A*, **626** (1997) 199.

- [15] B. Sun, R. Knöbel *et al.*, “Direct measurement of the 4.6 MeV isomer in stored bare ^{133}Sb ions”. *Phys. Lett. B*, **688** (2010) 294.
- [16] F. Bosch, T. Faestermann *et al.*, “Observation of bound-state β^- decay of fully ionized ^{187}Re : ^{187}Re - ^{187}Os cosmochronometry”. *Phys. Rev. Lett.*, **77** (1996) 5190.
- [17] I. Dillmann and Yu. A. Litvinov, “R-process nucleosynthesis: Present status and future experiments at the FRS and ESR”. *Prog. Part. Nucl. Phys.*, **66** (2011) 358.
- [18] D. Lunney, J. M. Pearson *et al.*, “Recent trends in the determination of nuclear masses”. *Rev. Mod. Phys.*, **75** (2003) 1021.
- [19] M. Goepfert-Mayer, “On closed shells in nuclei”. *Phys. Rev.*, **74** (1948) 235.
- [20] C. F. von Weizsäcker, “Zur Theorie der Kernmassen”. *Z. Phys.*, **96** (1935) 431.
- [21] E. M. Burbidge, G. R. Burbidge *et al.*, “Synthesis of the elements in stars”. *Rev. Mod. Phys.*, **29** (1957) 547.
- [22] F. W. Aston, “LIX. The mass-spectra of chemical elements”. *Phil. Mag.*, **39** (1920) 611.
- [23] A. S. Eddington, “The internal constitution of the stars”. *Nature*, **106** (1920) 14.
- [24] Yu. A. Litvinov, T. J. Bürvenich *et al.*, “Isospin dependence in the odd-even staggering of nuclear binding energies”. *Phys. Rev. Lett.*, **95** (2005) 042501.
- [25] L. Chen, Yu. A. Litvinov *et al.*, “Schottky mass measurement of the ^{208}Hg isotope: Implication for the proton-neutron interaction strength around doubly magic ^{208}Pb ”. *Phys. Rev. Lett.*, **102** (2009) 122503.
- [26] Y. H. Zhang, H. S. Xu *et al.*, “Mass measurements of the neutron-deficient ^{41}Ti , ^{45}Cr , ^{49}Fe , and ^{53}Ni nuclides: First test of the isobaric multiplet mass equation in *fp*-shell nuclei”. *Phys. Rev. Lett.*, **109** (2012) 102501.
- [27] D. Shubina, R. B. Cakirli *et al.*, “Schottky mass measurements of heavy neutron-rich nuclides in the element range $70 \leq Z \leq 79$ at the GSI experimental storage ring”. *Phys. Rev. C*, **88** (2013) 024310.
- [28] P. Shuai, H. S. Xu *et al.*, “Charge and frequency resolved isochronous mass spectrometry and the mass of ^{51}Co ”. *Phys. Lett. B*, **735** (2014) 327.
- [29] K. Blaum, “High-accuracy mass spectrometry with stored ions”. *Phys. Rep.*, **425** (2006) 1.
- [30] K. Blaum, J. Dilling *et al.*, “Precision atomic physics techniques for nuclear physics with radioactive beams”. *Phys. Scr.*, **2013** (2013) 014017.
- [31] J. Clark and G. Savard, “Precision masses for studies of the astrophysical r-process”. *Int. J. Mass Spectrom.*, **349–350** (2013) 81.
- [32] H. Schatz, “Nuclear masses in astrophysics”. *Int. J. Mass Spectrom.*, **349–350** (2013) 181.
- [33] X. L. Tu, H. S. Xu *et al.*, “Direct mass measurements of short-lived $A = 2Z - 1$ nuclides ^{63}Ge , ^{65}As , ^{67}Se , and ^{71}Kr and their impact on nucleosynthesis in the rp-process”. *Phys. Rev. Lett.*, **106** (2011) 112501.

- [34] X. L. Yan, H. S. Xu *et al.*, “Mass measurement of ^{45}Cr and its impact on the Ca-Sc cycle in X-ray bursts”. *Astrophys. J. Lett.*, **766** (2013) L8.
- [35] P. Walker and G. Dracoulis, “Energy traps in atomic nuclei”. *Nature*, **399** (1999) 35.
- [36] P. M. Walker and G. D. Dracoulis, “Exotic isomers in deformed atomic nuclei”. *Hyperfine Interact.*, **135** (2001) 83.
- [37] P. M. Walker and J. J. Carroll, “Ups and downs of nuclear isomers”. *Phys. Today*, **58** (2005) 39.
- [38] Yu. A. Litvinov, F. Attallah *et al.*, “Schottky mass measurements of cooled exotic nuclei”. *Hyperfine Interact.*, **132** (2001) 281.
- [39] Yu. A. Litvinov, H. Geissel *et al.*, “Precision experiments with time-resolved Schottky mass spectrometry”. *Nucl. Phys. A*, **734** (2004) 473.
- [40] Z. Liu, Yu. A. Litvinov *et al.*, “Exploring long-lived K -isomers via Schottky-mass-spectrometry at the ESR”. *Int. J. Mod. Phys. E*, **15** (2006) 1645.
- [41] B. Sun, Yu. A. Litvinov *et al.*, “Discovery of a new long-lived isomeric state in ^{125}Ce ”. *Eur. Phys. J. A*, **31** (2007) 393.
- [42] M. W. Reed, I. J. Cullen *et al.*, “Discovery of highly excited long-lived isomers in neutron-rich hafnium and tantalum isotopes through direct mass measurements”. *Phys. Rev. Lett.*, **105** (2010) 172501.
- [43] M. W. Reed, P. M. Walker *et al.*, “Long-lived isomers in neutron-rich $Z = 72-76$ nuclides”. *Phys. Rev. C*, **86** (2012) 054321.
- [44] L. Chen, P. M. Walker *et al.*, “Direct observation of long-lived isomers in ^{212}Bi ”. *Phys. Rev. Lett.*, **110** (2013) 122502.
- [45] F. Bosch, “The planned heavy-ion storage-cooler ring at GSI: A powerful tool for new experiments in atomic physics”. *Nucl. Instrum. Meth. B*, **23** (1987) 190.
- [46] F. Bosch, “Schottky mass- and lifetime-spectrometry of unstable, stored ions”. *J. Phys. B*, **36** (2003) 585.
- [47] F. Bosch, “Beta decay of highly charged ions”. *Hyperfine Interact.*, **173** (2007) 1.
- [48] M. Jung, F. Bosch *et al.*, “First observation of bound-state β^- decay”. *Phys. Rev. Lett.*, **69** (1992) 2164.
- [49] F. Bosch, “Manipulation of nuclear lifetimes in storage rings”. *Phys. Scr.*, **1995** (1995) 221.
- [50] F. Bosch, “Measurement of mass and beta-lifetime of stored exotic nuclei”. *Lect. Notes Phys.*, **651** (2004) 137.
- [51] H. Irnich, H. Geissel *et al.*, “Half-life measurements of bare, mass-resolved isomers in a storage-cooler ring”. *Phys. Rev. Lett.*, **75** (1995) 4182.
- [52] Yu. A. Litvinov, F. Attallah *et al.*, “Observation of a dramatic hindrance of the nuclear decay of isomeric states for fully ionized atoms”. *Phys. Lett. B*, **573** (2003) 80.

- [53] T. Ohtsubo, F. Bosch *et al.*, “Simultaneous measurement of β^- decay to bound and continuum electron states”. *Phys. Rev. Lett.*, **95** (2005) 052501.
- [54] Yu. A. Litvinov, F. Bosch *et al.*, “Measurement of the β^+ and orbital electron-capture decay rates in fully ionized, hydrogenlike, and heliumlike ^{140}Pr ions”. *Phys. Rev. Lett.*, **99** (2007) 262501.
- [55] N. Winckler, H. Geissel *et al.*, “Orbital electron capture decay of hydrogen- and helium-like ^{142}Pm ions”. *Phys. Lett. B*, **679** (2009) 36.
- [56] D. R. Aranasov, N. Winckler *et al.*, “Half-life measurements of stored fully ionized and hydrogen-like ^{122}I ions”. *Eur. Phys. J. A*, **48** (2012) 1.
- [57] Yu. A. Litvinov, F. Bosch *et al.*, “Observation of non-exponential orbital electron capture decays of hydrogen-like ^{140}Pr and ^{142}Pm ions”. *Phys. Lett. B*, **664** (2008) 162.
- [58] F. Bosch and Yu. A. Litvinov, “Observation of non-exponential orbital electron-capture decay of stored hydrogen-like ions”. *Prog. Part. Nucl. Phys.*, **64** (2010) 435.
- [59] P. Kienle, F. Bosch *et al.*, “High-resolution measurement of the time-modulated orbital electron capture and of the β^+ decay of hydrogen-like $^{142}\text{Pm}^{60+}$ ions”. *Phys. Lett. B*, **726** (2013) 638.
- [60] Z. Patyk, H. Geissel *et al.*, “ α -decay half-lives for neutral atoms and bare nuclei”. *Phys. Rev. C*, **78** (2008) 054317.
- [61] A. Musumarra, F. Farinon *et al.*, “Electron screening effects on α -decay”. *AIP Conf. Proc.*, **1165** (2009) 415.
- [62] C. Nociforo, F. Farinon *et al.*, “Measurements of α -decay half-lives at GSI”. *Phys. Scr.*, **2012** (2012) 014028.
- [63] M. Arnould, S. Goriely *et al.*, “The r-process of stellar nucleosynthesis: Astrophysics and nuclear physics achievements and mysteries”. *Phys. Rep.*, **450** (2007) 97.
- [64] K. Langanke and M. Wiescher, “Nuclear reactions and stellar processes”. *Rep. Prog. Phys.*, **64** (2001) 1657.
- [65] T. Kodama and K. Takahashi, “On the delayed neutrons at the final stage of the r-process”. *Phys. Lett. B*, **43** (1973) 167.
- [66] S. Das, “The importance of delayed neutrons in nuclear research—A review”. *Prog. Nucl. Energy*, **28** (1994) 209.
- [67] A. Evdokimov, I. Dillmann *et al.*, “An alternative approach to measure beta-delayed neutron emission”. *Proc. Nuclei in the Cosmos XII*, Cairns, Australia (2012) 115.
- [68] O. Klepper and C. Kozhuharov, “Particle detectors for beam diagnosis and for experiments with stable and radioactive ions in the storage-cooler ring ESR”. *Nucl. Instrum. Meth. B*, **204** (2003) 553.
- [69] T. W. Hänsch and A. L. Schawlow, “Cooling of gases by laser radiation”. *Opt. Commun.*, **13** (1975) 68.
- [70] S. van der Meer, “Stochastic damping of betatron oscillations in the ISR”. *CERN-ISR-PO-72-31*, CERN, Geneva, Switzerland (1972).

- [71] G. I. Budker, “An effective method of damping particle oscillations in proton and antiproton storage rings”. *At. Energy*, **22** (1967) 438.
- [72] H. Wollnik, “Laterally and longitudinally dispersive recoil mass separators”. *Nucl. Instrum. Meth. B*, **26** (1987) 267.
- [73] M. Wang, G. Audi *et al.*, “The AME2012 atomic mass evaluation (II)”. *Chin. Phys. C*, **36** (2012) 1603.
- [74] W. Schottky, “Über spontane Stromschwankungen in verschiedenen Elektrizitätsleitern”. *Ann. Phys. (Berlin)*, **362** (1918) 541.
- [75] J. Borer, P. Bramham *et al.*, “Non-destructive diagnostics of coasting beams with Schottky noise”. *Proc. HEACC '74*, Stanford, California, USA (1974) 53056.
- [76] S. van der Meer, “Diagnostics with schottky noise”. *Lect. Notes Phys.*, **343** (1989) 423.
- [77] B. Franzke, K. Beckert *et al.*, “Schottky mass spectrometry at the experimental storage ring ESR”. *Phys. Scr.*, **T59** (1995) 176.
- [78] F. Nolden, “Beams at storage rings—from proton to uranium”. *Int. J. Mod. Phys. E*, **18** (2009) 474.
- [79] W. D. Phillips, “Laser cooling and trapping of neutral atoms”. *Rev. Mod. Phys.*, **70** (1998) 721.
- [80] H. Poth, “Electron cooling: Theory, experiment, application”. *Phys. Rep.*, **196** (1990) 135.
- [81] D. Möhl, G. Petrucci *et al.*, “Physics and technique of stochastic cooling”. *Phys. Rep.*, **58** (1980) 73.
- [82] F. Nolden, K. Beckert *et al.*, “Experience and prospects of stochastic cooling of radioactive beams at GSI”. *Nucl. Instrum. Meth. A*, **532** (2004) 329.
- [83] M. Steck, K. Beckert *et al.*, “Anomalous temperature reduction of electron-cooled heavy ion beams in the storage ring ESR”. *Phys. Rev. Lett.*, **77** (1996) 3803.
- [84] M. Hausmann, F. Attallah *et al.*, “First isochronous mass spectrometry at the experimental storage ring ESR”. *Nucl. Instrum. Meth. A*, **446** (2000) 569.
- [85] H. Geissel, “Precision experiments with relativistic exotic nuclei at GSI”. *Prog. Part. Nucl. Phys.*, **42** (1999) 3.
- [86] X. L. Tu, M. Wang *et al.*, “Precision isochronous mass measurements at the storage ring CSRe in Lanzhou”. *Nucl. Instrum. Meth. A*, **654** (2011) 213.
- [87] A. Dolinskii, S. Litvinov *et al.*, “Study of the mass resolving power in the CR storage ring operated as a TOF spectrometer”. *Nucl. Instrum. Meth. A*, **574** (2007) 207.
- [88] H. Geissel, R. Knöbel *et al.*, “A new experimental approach for isochronous mass measurements of short-lived exotic nuclei with the FRS-ESR facility”. *Hyperfine Interact.*, **173** (2006) 49.
- [89] A. Dolinskii, H. Geissel *et al.*, “The CR storage ring in an isochronous mode operation with nonlinear optics characteristics”. *Nucl. Instrum. Meth. B*, **266** (2008) 4579.

- [90] S. Litvinov, D. Toprek *et al.*, “Isochronicity correction in the CR storage ring”. *Nucl. Instrum. Meth. A*, **724** (2013) 20.
- [91] X. Gao, Y.-J. Yuan *et al.*, “Isochronicity corrections for isochronous mass measurements at the HIRFL-CSR_e”. *Nucl. Instrum. Meth. A*, **763** (2014) 53.
- [92] H. Geissel and Yu. A. Litvinov, “Precision experiments with relativistic exotic nuclei at GSI”. *J. Phys. G*, **31** (2005) S1779.
- [93] B. Sun, R. Knöbel *et al.*, “A new resonator Schottky pick-up for short-lived nuclear investigations”. *PHN-NUSTAR-FRS-21*, GSI, Darmstadt (2011).
- [94] W. Zhang, X. L. Tu *et al.*, “A timing detector with pulsed high-voltage power supply for mass measurements at CSR_e”. *Nucl. Instrum. Meth. A*, **755** (2014) 38.
- [95] G. Dôme, “Basic RF theory, waveguides and cavities”. *Proc. CAS ’91: RF Engineering for Particle Accelerators*, Oxford, UK (1991) 1.
- [96] F. Gerigk, “Cavity types”. *Proc. CAS ’10: RF for Accelerators*, Ebeltoft, Denmark (2010) 277.
- [97] A. Wolski, “Theory of electromagnetic fields”. *Proc. CAS ’10: RF for Accelerators*, Ebeltoft, Denmark (2010) 15.
- [98] R. Lorenz, “Cavity beam position monitors”. *Proc. BIW ’98*, Stanford, California, USA (1998) 53.
- [99] J. Müller, “Untersuchung über elektromagnetische Hohlräume”. *Hochfrequenztech. Electroakus.*, **54** (1939) 157.
- [100] J. C. Slater, “Microwave electronics”. *Rev. Mod. Phys.*, **18** (1946) 441.
- [101] R. Waldron, “Perturbation theory of resonant cavities”. *Proc. IEE*, **107** (1960) 272.
- [102] R. Carter, “Accuracy of microwave cavity perturbation measurements”. *IEEE Trans. Microw. Theory Techn.*, **49** (2001) 918.
- [103] E. G. Spencer and R. C. LeCraw, “Wall effects on microwave measurements of ferrite spheres”. *J. Appl. Phys.*, **26** (1955) 250.
- [104] D. Boussard, “Schottky noise and beam transfer function diagnostics”. *Proc. CAS ’85*, Oxford, UK (1985) 416.
- [105] H. Klein, “Basic concepts I”. *Proc. CAS ’91: RF Engineering for Particle Accelerators*, Oxford, UK (1991) 97.
- [106] M. Chodorow, E. L. Ginzton *et al.*, “Stanford high-energy linear electron accelerator (Mark III)”. *Rev. Sci. Instrum.*, **26** (1955) 134.
- [107] E. Jensen, “Cavity basics”. *Proc. CAS ’10: RF for Accelerators*, Ebeltoft, Denmark (2010) 259.
- [108] D. Alesini, “Power coupling”. *Proc. CAS ’10: RF for Accelerators*, Ebeltoft, Denmark (2010) 125.
- [109] W. Schnell, “Common-mode rejection in resonant microwave position monitors for linear colliders”. *CLIC-Note-70*, CERN, Geneva (1988).

- [110] D. A. Goldberg and G. R. Lambertson, “Dynamic devices: A primer on pickups and kickers”. *AIP Conf. Proc.*, **249** (1992) 537.
- [111] S. Chattopadhyay, “Some fundamental aspects of fluctuations and coherence in charged-particle beams in storage rings”. *AIP Conf. Proc.*, **127** (1985) 467.
- [112] F. Nolden, “Instrumentation and diagnostics using Schottky signals”. *Proc. DIPAC '01*, Grenoble, France (2001) 6.
- [113] X. Chen, M. S. Sanjari *et al.*, “Accuracy improvement in the isochronous mass measurement using a cavity doublet”. *Hyperfine Interact.*, (in press), preview available at doi:10.1007/s10751-015-1183-3.
- [114] G. Audi, W. G. Davies *et al.*, “A method of determining the relative importance of particular data on selected parameters in the least-squares analysis of experimental data”. *Nucl. Instrum. Meth. A*, **249** (1986) 443.
- [115] Yu. A. Litvinov, H. Geissel *et al.*, “Mass measurement of cooled neutron-deficient bismuth projectile fragments with time-resolved Schottky mass spectrometry at the FRS-ESR facility”. *Nucl. Phys. A*, **756** (2005) 3.
- [116] R. Bergere, A. Veyssiere *et al.*, “Linac beam position monitor”. *Rev. Sci. Instrum.*, **33** (1962) 1441.
- [117] P. Brunet, J. Dobson *et al.*, “Microwave beam position monitors”. *TN-64-45*, SLAC, Stanford (1964).
- [118] E. V. Farinholt, Z. D. Farkas *et al.*, “Microwave beam position monitors at SLAC”. *IEEE Trans. Nucl. Sci.*, **14** (1967) 1127.
- [119] D. A. Goldberg, W. Barry *et al.*, “A high-frequency Schottky detector for use in the Tevatron”. *Proc. PAC '87*, Washington, DC, USA (1987) 547.
- [120] Y. Inoue, H. Hayano *et al.*, “Development of a high-resolution cavity-beam position monitor”. *Phys. Rev. ST Accel. Beams*, **11** (2008) 062801.
- [121] J. Su, Y. Du *et al.*, “Design and cold test of a rectangular cavity beam position monitor”. *Chin. Phys. C*, **37** (2013) 017002.
- [122] J. McKeown, “Beam position monitor using a single cavity”. *IEEE Trans. Nucl. Sci.*, **26** (1979) 3423.
- [123] R. Lill, G. Waldschmidt *et al.*, “Linac coherent light source undulator RF BPM system”. *Proc. FEL '06*, Berlin, Germany (2006) 706.
- [124] H. Maesaka, H. Ego *et al.*, “Sub-micron resolution RF cavity beam position monitor system at the SACLA XFEL facility”. *Nucl. Instrum. Meth. A*, **696** (2012) 66.
- [125] M. Dal Forno, P. Craievich *et al.*, “A novel electromagnetic design and a new manufacturing process for the cavity BPM (Beam Position Monitor)”. *Nucl. Instrum. Meth. A*, **662** (2012) 1.
- [126] S. Walston, S. Boogert *et al.*, “Performance of a high resolution cavity beam position monitor system”. *Nucl. Instrum. Meth. A*, **578** (2007) 1.

- [127] M. Slater, C. Adolphsen *et al.*, “Cavity BPM system tests for the ILC energy spectrometer”. *Nucl. Instrum. Meth. A*, **592** (2008) 201.
- [128] S. Shin and M. Wendt, “Design studies for a high resolution cold cavity beam position monitor”. *IEEE Trans. Nucl. Sci.*, **57** (2010) 2159.
- [129] Y. I. Kim, R. Ainsworth *et al.*, “Cavity beam position monitor system for the Accelerator Test Facility 2”. *Phys. Rev. ST Accel. Beams*, **15** (2012) 042801.
- [130] R. Ursic, R. Flood *et al.*, “1 nA beam position monitoring system”. *Proc. PAC '97*, Vancouver, Canada (1997) 2131.
- [131] T. R. Pusch, F. Frommberger *et al.*, “Measuring the intensity and position of a pA electron beam with resonant cavities”. *Phys. Rev. ST Accel. Beams*, **15** (2012) 112801.
- [132] M. Hansli, R. Jakoby *et al.*, “Current status of the Schottky cavity sensor for the CR at FAIR”. *Proc. IBIC '13*, Oxford, UK (2013) 907.
- [133] T. Shintake, “The choke mode cavity”. *KEK-Preprint-92-51*, KEK, Tsukuba (1992).
- [134] O. Altenmueller and P. Brunet, “Some RF characteristics of the beam phase reference cavity”. *TN-64-51*, SLAC, Stanford (1964).
- [135] R. Bossart, “High precision beam position monitor using a re-entrant coaxial cavity”. *Proc. LINAC '94*, Tsukuba, Japan (1994) 851.
- [136] C. Magne, M. Juillard *et al.*, “High resolution BPM for future colliders”. *Proc. LINAC '98*, Chicago, Illinois, USA (1998) 323.
- [137] C. Simon, M. Luong *et al.*, “Performance of a reentrant cavity beam position monitor”. *Phys. Rev. ST Accel. Beams*, **11** (2008) 082802.
- [138] M. S. Sanjari, X. Chen *et al.*, “Conceptual design of elliptical cavities for intensity and position sensitive beam measurements in storage rings”. *Phys. Scr.*, (in press), preview available at arXiv:1506.00440v2.
- [139] P. M. Walker, Yu. A. Litvinov *et al.*, “The ILIMA project at FAIR”. *Int. J. Mass Spectrom.*, **349–350** (2013) 247.
- [140] S. Litvinov, C. Dimopoulou *et al.*, “Status of the storage ring design at FAIR”. *Proc. STORI '11*, Frascati, Italy (2011) 26.
- [141] ILIMA Collaboration, “Technical proposal for the ILIMA project”. *TP-ILIMA*, GSI, Darmstadt (2005).
- [142] H. Nyquist, “Certain topics in telegraph transmission theory”. *Trans. Am. Inst. Elec. Eng.*, **47** (1928) 617.
- [143] C. Shannon, “Communication in the presence of noise”. *Proc. IRE*, **37** (1949) 10.
- [144] T. Schilcher, “RF applications in digital signal processing”. *Proc. CAS '07: Digital Signal Processing*, Sigtuna, Sweden (2007) 249.
- [145] J. B. Johnson, “Thermal agitation of electricity in conductors”. *Phys. Rev.*, **32** (1928) 97.

- [146] H. Nyquist, "Thermal agitation of electric charge in conductors". *Phys. Rev.*, **32** (1928) 110.
- [147] F. Caspers, "RF engineering basic concepts: S -parameters". *Proc. CAS '10: RF for Accelerators*, Ebeltoft, Denmark (2010) 67.
- [148] K. Kurokawa, "Power waves and the scattering matrix". *IEEE Trans. Microw. Theory Techn.*, **13** (1965) 194.
- [149] F. Caspers, "RF engineering basic concepts: The Smith chart". *Proc. CAS '10: RF for Accelerators*, Ebeltoft, Denmark (2010) 95.
- [150] P. H. Smith, "An improved transmission line calculator". *Electronics*, **17** (1944) 130.
- [151] D. Kajfez, "Linear fractional curve fitting for measurement of high Q factors". *IEEE Trans. Microw. Theory Techn.*, **42** (1994) 1149.
- [152] J. Gao, "Effects of the cavity walls on perturbation measurements". *IEEE Trans. Instrum. Meas.*, **40** (1991) 618.
- [153] R. Sillars, "The properties of a dielectric containing semiconducting particles of various shapes". *J. Inst. Elect. Eng.*, **80** (1937) 378.
- [154] A. Sihvola, "Dielectric polarization and particle shape effects". *J. Nanomater.*, **2007** (2007) 45090.
- [155] L. A. Apresyan and D. V. Vlasov, "On depolarization factors of anisotropic ellipsoids in an anisotropic medium". *Tech. Phys.*, **59** (2014) 1760.
- [156] M. Wakasugi, "The rare RI ring facility at the RIKEN RI beam factory". *J. Phys. Soc. Conf. Proc.*, **6** (2015) 010020.
- [157] M. Grieser, Yu. A. Litvinov *et al.*, "Storage ring at HIE-ISOLDE". *Eur. Phys. J. Spec. Top.*, **207** (2012) 1.
- [158] X. Gao, J.-C. Yang *et al.*, "SHER-HIAF ring lattice design". *Chin. Phys. C*, **38** (2014) 047002.
- [159] J. C. Gutiérrez-Vega, R. M. Rodríguez-Dagnino *et al.*, "Mathieu functions, a visual approach". *Am. J. Phys.*, **71** (2003) 233.

ACKNOWLEDGMENTS



This dissertation would never have been finished without the support in various aspects from numerous people, to whom I express my earnest gratitude. Furthermore, I feel especially appreciative to every person in my life who has shaped me into who I am today.

In particular, I would like to thank my supervisor, Yuri Litvinov, for his care, guidance, and personality that have profoundly influenced me since my first day at GSI. I am also most indebted to my professor, Klaus Blaum, for his critical role in my doctoral study at university; to Adriana Pálffy, for her agreement on refereeing this dissertation at the last minute without notice; and to Peter Fischer, for his time and service on my thesis committee.

Additionally, I am grateful to my advisor, Shahab Sanjari, for his enthusiasm, knowledge, and encouragement throughout my doctoral training; to Jeremi Piotrowski, for his help with setting up the lab and as a companion there; to Markus Steck, for his discipline and insightful criticism on this dissertation; to Pierre-Michel Hillenbrand, for translating the abstract of this dissertation into German; to Christian Trageser, for creating the productive atmosphere in the office during my thesis writing; and to Oleksandr Kovalenko, for demonstrating the administrative procedures required by the graduate school.

Moreover, I am thankful to Fritz Bosch, Peter Hülsmann, Sergey Litvinov, Fritz Nolden, Xiaolin Tu, Nicolas Winckler, and Xinliang Yan at GSI; to Hushan Xu, Yuhu Zhang, Xiaohong Zhou, Yippan Guo, Mingzhi Li, Minle Liang, Jing Si, Xiaohua Yuan, and Wei Zhang at IMP; and to Tomohiro Uesaka, Taka Yamaguchi, Zhuang Ge, Sarah Naimi, and Fumi Suzaki at RIKEN.

This thesis work has received funding from the European Union within the Marie Curie Innovative Training Network—the oPAC project. I would like to pass my heartfelt thanks to the project management team—Carsten Welsch, Rita Galan, Blaise Guenard, Ricardo Torres, Glenda Wall, and Helen Williams—for their thoughtful organization of every training event; and to all the oPAC fellows for the fabulous memories we have shared over the past three years.

Finally, I would like to dedicate this dissertation to my parents, whom I cannot thank enough.